Overview article

Fracture and fatigue in additively manufactured metals

Thorsten Hermann Becker[a], Punit Kumar[b], Upadrasta Ramamurty[b,c,*]

[a] *Department of Mechanical and Mechatronic Engineering, Stellenbosch University, Stellenbosch, South Africa*
[b] *School of Mechanical and Aerospace Engineering, Nanyang Technological University, Singapore*
[c] *Institute of Materials Research and Engineering, Agency for Science, Technology and Research (A∗STAR), 138634 Singapore*

ARTICLE INFO

ABSTRACT

Additive manufacturing (AM) of metallic components offers many advantages over conventional manufacturing methods, most notably design freedom at little material waste. Consequently, there is significant current interest in the manufacturing aspects of a wide variety of structural alloys. Concomitantly, establishing the processing – microstructure – mechanical performance relations, in conjunction with the attributes such as flaws, residual stresses, and mesostructures inherent to the AM processes, is critical for the widespread adoption of structural metallic components made using AM. Keeping this in view, a comprehensive review of the current understanding of the structure-property correlations in AM alloys is provided here. Unique aspects of the microstructures of the AM alloys, process-related attributes, and their effect on the tensile, fracture, fatigue crack growth, and unnotched fatigue properties are highlighted, with emphasis on the interplay between the microstructures and process attributes in determining the structural integrity of AM alloys in terms of properties such as near-threshold fatigue crack growth rate, fracture toughness, and fatigue strength. These aspects are contrasted with respective structure-property correlations in wrought or cast alloys. Strategies employed for improving the damage tolerance of the alloys through either improvisation of the processing conditions during AM or via post-processing treatments such as annealing, hot-isostatic pressing, and shot peening, are summarized. The existing gaps in understanding fatigue and fracture in AM alloys, which are critical for widespread deployment and reliable design of engineering components, are identified; such gaps are expected to provide future avenues for research in this area.

1. Introduction

Conventional manufacturing of metallic parts, in addition to being a key technology enabler, is an integral part of the modern industrial economy. Typically, manufacturing consists of casting, followed by thermo-mechanical processing for 'shaping' using forging, rolling, or extrusion (or some other method), and final 'finishing' via welding, machining, surface modifications, amongst others. As these processes have been fine-tuned and perfected over several centuries, a detailed understanding of the relationship between the alloy's composition, processing history, microstructural evolution, and mechanical performance has been developed and put into industrial practice. Given that a structural part must often satisfy several property metrics simultaneously, such knowledge is particularly critical as minute variations in either the composition or processing routes (or both) can alter the property combinations in myriad ways that are not necessarily correlated in a simple manner.

Additive manufacturing (AM)—versus 'subtractive manufacturing' typically employed in conventional manufacturing—has the potential to usurp the aforementioned fine-tuned manufacturing equilibrium. This is because of the number of advantages it offers: (i) near-net shaped part fabrication using only one fabrication step, (ii) design flexibility that allows access to design space that could otherwise not be utilised, (iii) near-zero material wastage, resulting in high 'fly-to-buy' ratios, (iv) rapid prototyping and testing of parts, which markedly reduces the 'concept-to-deployment' cycle times for new designs, (v) flexibility in terms of manufacturing different types of components using different alloys, (vi) on-demand manufacturing resulting in low inventory costs and minimal supply chain disruptions, and (vii) ability to produce parts with compositional gradients or contain multiple alloys within them. Hence, considerable excitement about AM exists worldwide, with substantial investments already made (or being made) for research and capacity building. The importance of AM for Industry 4.0 due to its digital nature is also an underlying reason.

Terminology/Symbols

AM	Additive Manufacturing
LB-PBF	Laser based powder bed fusion processes
EB-PBF	Electron beam-based powder bed fusion processes
HAADF	High-angle annular dark-field imaging
X, Y and Z	The coordinate system for the AM system as defined in ISO / ASTM52921
LOF	Lack-of-fusion flaw
AB	As built
AN	Annealing treatment
DA	Duplex annealing treatment
BA	Beta annealing treatment
HSTA	homogenisation and solutionising treatment
ST	Solution treated
MP	machined, or machined and polished
VP	vibratory polished
EP	electro polished
AP	abrasive blast polishing
YS	Yield strength
UTS	Ultimate tensile strength
EF	Elongation at failure
G	Temperature gradient
A	Austinite
M	Martensite
PBG	prior-β grain
R_a	surface roughness average
R	load ratio
m	crack growth rate exponent
ΔK	cyclic stress intensity factor
ΔK_{th}	threshold cyclic stress intensity factor
K_{Ic}	mode I plane strain fracture toughness
BJP	Binder Jet Printing
LB-DED	Laser based direct energy deposition
STEM	Scanning transmission electron microscopy
X-Y	Crack opening in X, crack direction in Y (or vice versa).
X-Z	Crack opening in X or Y, crack direction in Z
Z-X	Crack opening in Z, crack direction in X or Y
AR	Aspect ratio
STA	Solutionising and ageing treatment
AG	Age hardening treatment
SR	Stress-relieving treatment
HIP	Hot Isostatic Pressing treatment
FC	Furnace cooling
AC	Air cooling
WQ	Water quenching
SB	sand blasting
SP	shot peened
LSP	laser shock peened
CP	cavitation peening
FCG	Fatigue crack growth
HCF	High cycle fatigue strength
H	Solidification rate
α	alpha phase
α'	martensitic phase
β	beta phase
γ, γ' and γ''	gamma phases
δ	delta phase

σ	omega phase
Y	geometry factor
ψ	sphericity
a_i initial flaw size σ_a	cyclic stress amplitude
d	flaw diameter
h	hatch spacing
t	layer thickness

Amongst different classes of materials that are being explored, AM of metals and alloys is technologically the most challenging as producing parts in a highly reproducible manner is not as simple as it *prima facie* appears to be. This is exacerbated by the fact that additional process-related attributes such as porosity, residual stresses, mesostructures that arise due to line-by-line, layer-by-layer build strategies, and variations in the microstructures from location to location of the built part add considerable complexity to the establishment of the processing-structure-property relations. Consequently, ensuring structural integrity and reliability of parts produced for quality assessment and certification purposes is still a major challenge that is holding the widespread adaptation of AM back. The key to addressing this challenge would be detailed structure-property correlations that also take process attributes into account. While the manufacturing aspects and the microstructure – tensile property connections are extensively investigated and reported, fatigue and fracture aspects, which ultimately dictate the structural integrity of engineering parts, are not extensively investigated, especially from the 'microstructural' perspective.

Fatigue driven fracture is the most prominent cause of structural failure in load-bearing components. The microstructural origins for the initiation, propagation and fast fracture mechanisms that drive fatigue failure in conventionally manufactured metals alloys are well understood. However, the understanding of how the unique microstructures in AM alloys, such as fine metastable phases, mesostructures, and porosity - all of which directly result from the unique processing attributes, affect the fatigue and fracture is not firmly established yet. This is not only critical for reliability assessments of AM components, but will also aid in identifying the processing steps that must be modified to produce components with adequate or superior structural integrity. AM is associated with a vast amount of process parameters, allows for intricate design features that result in highly unusual loading configurations, and allows for customisable part production; this makes linking material, process and structure especially difficult. Keeping this in view, we provide a comprehensive review of the fatigue and fracture aspects of AM alloys here. Moreover, since the microstructures and tensile properties form an essential part of the discussion, those aspects are also summarised.

Given the exponential increase in research on AM alloys, it is not surprising that several reviews on the AM of metals are already available. For example, Gu et al. [1], Sames et al. [2], Herzog et al. [3], and DebRoy et al. [4] provide a comprehensive overview of the physical processes, the metallurgy and its influence on properties. The focus of many such reviews has been on many applications of different metals and the AM process itself; for example, Mostafaei et al. [5] reviewed the binder jetting process. Reviews that focus on specific metals include; titanium alloys by Dutta et al. [6], Agius et al. [7], Romero et al. [8], Liu et al. [9]; aluminium alloys by Aboulkhair et al. [10]; stainless steels by Fayazfar et al. [11] and Bajaj et al. [12]; and Nickel-based superalloys by Babu et al. [13] and Jinoop et al. [14]. This has resulted in a flurry of publications that focus on the fatigue and fracture of AM metals. While Lewandowski and Seifi [15] provided a review that was exclusively focused on mechanical properties, substantial

progress is made over the last five years. In a review by Sanaei et al. [16], the effect of process-related attributes on high cycle fatigue behaviour was highlighted. While the articles by Shamsaei et al. [17,18] and Fotovvati et al. [19] review the fatigue properties of AM metals, the emphasis is not on the interrelationship between the microstructures - the process related attributes - properties, which the present overview seeks to place emphasise on.

This review is organized in the following manner. A brief overview of widely used AM techniques and alloys, emphasising relevant process attributes and commonly reported AM alloys, is provided in next section (Section 2). The theme of commonly reported AM alloys carries throughout the review, starting with a discussion on the microstructural features (Section 3) and process-related attributes (Section 4). Following this, a review of quasi-static properties, namely tensile (Section 5) and Fracture Toughness (Section 6) properties, is presented. Section 7 focuses on the fatigue crack growth behaviour, while Section 8 focuses on un-notched fatigue. The review concludes by presenting closing remarks in Section 9.

2. Widely used AM techniques and alloys

2.1. Methods

The ISO/ASTM 52900 standard currently classifies AM processes into the following seven categories [20]: Binder Jetting (or binder jet printing, BJP), Directed Energy Deposition (DED), Material Extrusion, Material Jetting, Powder Bed Fusion (PBF), Sheet Lamination, and Vat Photopolymerization. These are further grouped based on the energy source used (laser or electron beam and arc), the feedstock state (powder, wire or sheet), and the method of material feed (blown or fed powder or powder bed) [20]. Based on the volume and quality of literature available on fatigue and fracture AM alloys and microstructure-property correlations in them, this overview's focus is limited to the three powder-based technologies, BJP, PBF and DED. While PBF and DED processes (with the heat source being either a laser or an electron beam) are considered as direct fabrication routes, BJP is regarded as an indirect one [2]. Parts produced using the direct methods are generally considered superior in terms of consistency and dimensional accuracy, and hence are more prevalent in terms of recent research efforts and potential for applications [21].

In contrast to DED, PBF is overwhelmingly used for the manufacturing of full-sized parts and is, therefore, the closest natural alternative to traditional manufacturing in terms of industrial application. The most popular metal AM method is the Laser based PBF or LB-PBF. Its popularity is primarily due to comparatively higher dimensional accuracy, lower machine costs, and shorter build times. Electron beam based PBF, or EB-PBF, is performed in high-vacuum, often below 10^{-4} mbar, providing an ideal low-contamination environment for manufacturing materials with a high affinity for oxygen and nitrogen, such as Ti and Al alloys [6]. Generally, build times with EB-PBF are shorter than those with LB-PBF due to higher energy input and faster scan speed. Parts are usually built on a heated build platform (600–750 °C), leading to a more stable microstructure in the as built (AB) state itself [22]. The major drawbacks of EB-PBF are the inferior surface quality in the printed parts and higher cost compared to LB-PBF.

In DED, the material is commonly deposited through pressured powder injection to the heat source's focus point [6]. Most frequently, DED is used for surface coating and repair of parts where the material is missing due to wear or damage. While an electron beam or an arc heat-source has been used in DED technologies, most of the recent development has been focused on Laser based DED, or LB-DED [11].

Indirect methods such as BJP use a relatively inexpensive process to fabricate a 'green' part, after which several critical post-process operations densify and improve the part's mechanical performance. While the fabrication of the 'green' part is faster than other AM processes, extensive post-processing is required, which takes up most of the fabrication time. BJP has grown to become the most popular indirect metal AM technology in recent years. The working principle consists of bonding powder through precisely jetting a polymer-based binding agent to form a green part. The binding medium is then either removed through ultra-violet radiation or during a sintering process.

The basic principles of the three commonly used metal AM methods are briefly described below. The PBF process is schematically illustrated in Fig. 1a [23]. The powder is distributed on the bed using either a hopper or a reservoir next to the powder bed. Each layer is selectively molten usually one line at a time with an overlap to adjacent lines to form a layer of the desired shape. For the fabrication of the successive layer, the build platform is lowered, a new powder layer of predetermined thickness is spread over the powder bed, and selective melting is repeated. This process is repeated to build the three-dimensional part. After fabrication, the unmolten powder is removed to reveal the part in its AB state, fused to the build platform. Ideally, the part is stress-relieved (SR) before removing support structures and removing the build platform to avoid distortions. Post-processing is typically undertaken, including a heat treatment, such as annealing (AN) and surface finishing steps to increase mechanical properties and refine dimensional tolerances.

The layer thickness in PBF processes can range anywhere between 20 and 200 μm depending on the type of material and the heat source used for consolidation [24,25]. The typical 10th and 90th percentile powder particle diameters have 42 to 92 μm and 60 to 120 μm ranges, respectively [26,27]. For smooth flow and good packing of the powder beds, the particles need to be as spherical as possible with a narrow size distribution [11]. In LB-PBF, the powdered material is selectively molten, typically using an Nd:YAG laser with a wavelength of around 1070 nm and a power that ranges from 20 to 1000 W [28,29]. Typical spot sizes of the laser beam in the focal plane range between 50 to 180 μm [28–30], depending on the manufacturing system used [28,31]. The laser beam is directed using a galvanometer scanner to achieve scan speeds between 100 to 2000 mm/s across the deposited powder layer.

Usually, the sequence of the individual melt tracks follows a scan strategy, which includes a meander / to-and-fro approach [32], a checkerboard pattern, where individual islands are randomly fused [28], or stripes, where individual stripes of specified width are sequentially fused [29]. Some overlap between islands or stripes is typically included in the two latter approaches to reduce porosity. The scan direction is rotated and offset after each layer. In some cases the build platform is heated as, for example, recommended for the production of Al alloys [33–35]. This results in lower solidification rates resulting in a more stable melt and in some cases a higher build density [33].

In EB-PBF, the electron beam, typically accelerated with a voltage of 60 kV and focused using electromagnetic lenses, is directed by a magnetic scan coil to achieve scan speeds between 10 to 10^4 mm/s across the deposited powder layer [36]. In contrast to LB-PBF, the build platform is preheated in this method by defocusing the beam and scanning the bed surface several times [37]. To ensure complete melting, scan speeds are reduced to about 10^2 mm/s using a predefined scan strategy that is similar to LB-PBF. Typical layer thickness values are between 50 to 150 μm with the spot sizes ranging from 140 to 250 μm [31].

A schematical illustration of the DED process is provided in Fig. 1b. A part is built by melting a surface and simultaneously ap-
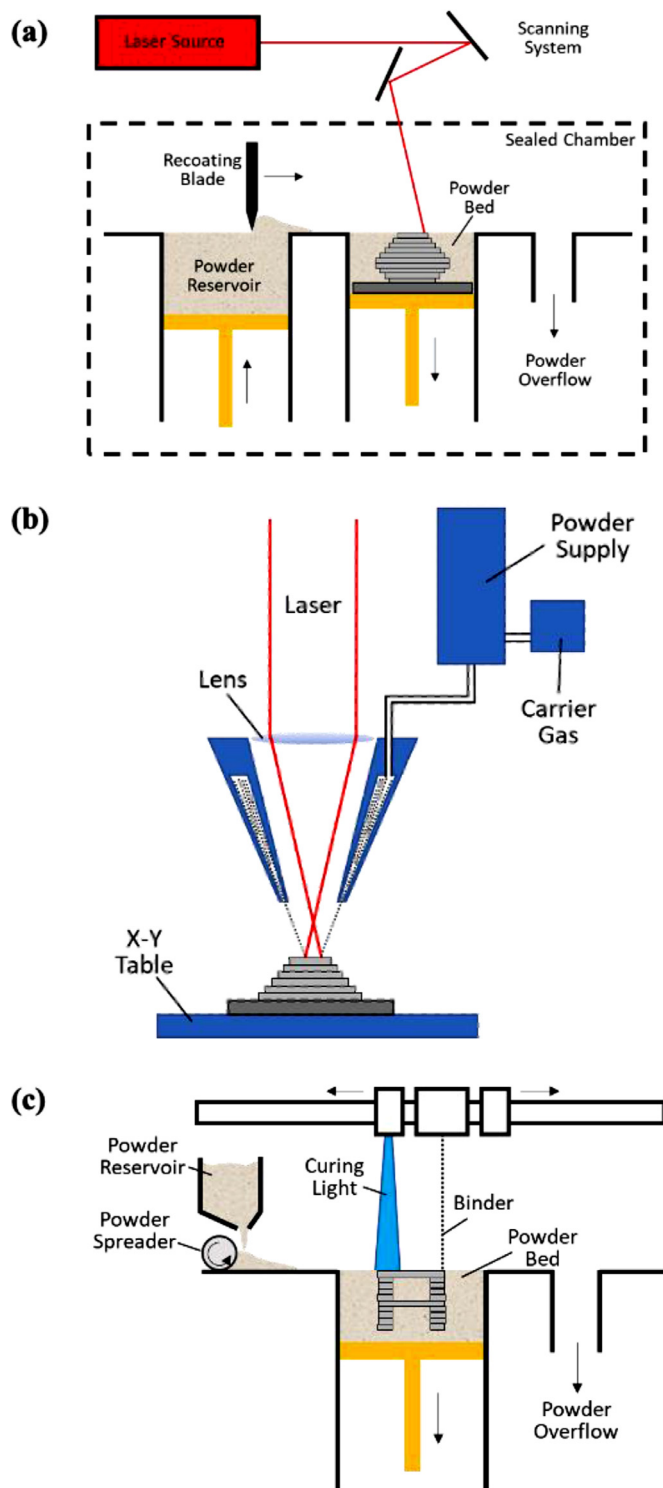
Fig. 1. Schematic diagrams illustrating (a) laser based powder bed fusion (LB-PBP) process, (b) laser based directed energy deposition (LB-DED) process, and (c) binder jet printing (BJP) process.

plying the powder feedstock. The powder is supplied by a nozzle that is mounted coaxially to the heat source. The resultant melt pool is typically protected against oxidation by flooding the build region with an inert gas. While a Nd:YAG laser is commonly used, the use of CO_2, Diode and Yb-doped fibre lasers have also been reported. The utilized power ranges between 800 and 2400 W [14] and the spot size varies between 0.3 and 3 mm [37,38], with a scan speed of around 900 mm/min [14]. A particular advantage

of the LB-DED processes is that they are not restricted to the in-plane layer builds; this provides more design freedom than PBF processes. The part is most commonly stationary while the deposition head is repositioned for each layer by, for example, a five-axis system or a robotic arm [39]. As such, DED processes are far less restricted by size and are therefore more commonly employed to produce large parts. Moreover, DED processes can be utilised in repair applications by depositing alloys onto an existing part [39].

While the BJP method also relies on a powder bed system (Fig. 1c), it employs selective deposition of binding agents to build a green part, which is subsequently subjected to a high-temperature sintering for burning the polymeric binder first and then sintering of the powder particles to achieve final density and strength [5]. The resulting microstructures are free from metastable phases, residual stresses, and are comparable to those produced using conventional means. While believed to be cheaper (and faster in terms of productivity), this process's major drawback is relatively higher porosity [40,41].

2.2. Alloys

A wide variety of metals and alloys are considered for AM; the most reported ones are Ti alloys, steels, Ni-based superalloys, and Al alloys. While studies on alloys such as Hastelloy X, CoCrX [42–44] and high entropy alloys such as FeCoCrNi [45], FeCoCrNiC0.05 [46,47], FeCoCrNiAl0.5 [48], FeMnCoCrSi [49] and FeCoCrNiMn [50–52], produced using laser-based processes, are also reported, in-depth studies that link microstructure to mechanical properties, especially fatigue and fracture, are limited and hence will not be considered in this overview*.

Among the Ti alloys, Ti-6Al-4V (Ti6Al4V), an $\alpha + \beta$ alloy, is the most widely explored, with LB-PBF, EB-PBF, and LB-DED successfully utilised to fabricate parts. Other Ti alloys, such as Ti13Nb13Zr [53] and Ti6Al2Sn4Zr2Mo [54] produced using LB-PBF and Ti6.5Al3.5Mo1.5Zr0.3Si produced using LB-DED [55,56], have also been examined. TiAl based alloys have also been produced, such as Ti48Al2Cr2Nb, using LB-PBF [57] and EB-PBF [58,59], and Ti43.5Al4Nb1Mo0.1B using EB-PBF [60].

Amongst the steels, common austenitic stainless steels (SS, all the designations are as per AISI) 316L, 304L, maraging steel 18Ni300, and precipitation hardenable 17-4PH steel received considerable attention. Most of these have successfully been fabricated via LB-PBF, EB-PBF, LB-DED, and BJP. In addition, H13 tool steel has been produced using LB-PBF [61–63] and LB-DED [64,65], 420 using LB-PBF [66] and BJP [67], and P21 (ASTM) using LB-DED [68], to name a few.

Ni-based superalloys, widely known for high-temperature applications, examined for their printability by using LB-PBF, EB-PBF, and LB-DED include Inconel 625 and 718. Additionally, fabrication of Inconel 100 parts using a Micro-Laser Assisted Machining process was also explored [69].

The number of different Al alloys produced using AM is limited. Alloys that have been successfully produced using LB-PBF, EB-PBF, and LB-DED include the age hardenable AlSi10Mg and the eutectic AlSi12. Other grades that have been reported include AA2139, an AlCuMg alloy produced using EB-PBF [70], and AlMg4.4Sc0.66MnZr produced using LB-PBF [71].

A key challenge with the processing of metals using AM lies in the nature of the interaction between the heat-source and the feedstock material. For example, Al has a high reflectivity for the wavelengths of the lasers that are usually applied in AM, resulting in poor heat-absorption. Moreover, alloying elements with highly different vapour pressures, Al alloyed with Mg and Li for example,

---

* All the compositions are in at.% (unless otherwise explicitly stated).

vaporise preferentially under vacuum conditions. A vast majority of the alloys are susceptible to cracking under the rapid solidification conditions that prevail during LB-PBF, EB-PBF, and LB-DED. In general, easily weldable alloys are also those that are amenable to AM with these methods. In addition to this, the allotropy of the alloy, Ti and Fe based ones for example, in combination with the large temperature gradients and complex thermal cycles usually associated with some of the AM techniques, make the relationship between AM process, microstructure and properties unique. This, in turn, makes the fabricated alloy and its mechanical properties highly sensitive to the process utilized. Therefore, the choice in process parameter combinations need to be made carefully and controlled precisely during the manufacturing of parts for greater reliability.

The quality of the powder feedstock plays a vital role in determining the overall quality of the build part, especially the relative density of it. In PBF processes, the powder particle size and distribution, sphericity, roughness, and microstructure [72] affect its flowability [73] and consequently the ability to deposit material during the AM process [74,75]. Nandwana et al. [72] reported that a broader particle size distributed led to lower porosity levels in EB-PBF Ti6Al4V. In contrast, a larger particle size leads to higher levels of porosity. The reuse of unmolten powder can lead to the pickup of oxygen, which, in turn, can result in embrittlement and a decrease in density. Tang et al. [76] report that the left-over powder in an EB-PBF Ti6Al4V became progressively less spherical with noticeable distortion and roughness, with a narrower distribution that, in turn, affects flaw formation.

Unlike PBF processes, DED methods are less sensitive to feedstock material. However, cracks or scratches on the powder particle surface can lead to porosity in the final AM part [2]. Nandwana et al. [77] reported that the powder size distribution and the alloy chemistry directly impact sintering kinetics of BJP part and, therefore, shrinkage and achievable densification. For example, they recommend that a bimodal powder size distribution with a 10:1 ratio allows for high density of the green part and subsequently the sintered part.

3. Micro- and mesostructures in AM alloys

The rapid solidification of a small volume of the melt at any given instance during AM employing the 'direct' methods imparts a microstructure to the alloy that is akin to those obtained using rapid quenching techniques: fine, metastable (often), and constituent phases with enhanced solid solubility. Repeated heating and cooling of the already deposited layer (during the subsequent layer fabrication over it) make the solidified alloy experience a complex thermal cycling history, which has important consequences both in terms of the microstructure development (columnar grains in some contexts, as we shall see later) and residual stresses. Another inherent feature of these techniques, the line-by-line and layer-by-layer building, imparts a mesostructure that often reflects the line hatch spacing, layer thickness and the scanning strategy. The combination of all these microstructural features, which span several length scales—from nanometre to millimetre (or more) scale—make the mechanical performance of alloys produced by AM unique and significantly different from their conventionally manufactured counterparts. In this section, we first summarise common features across several AM alloy classes and then present features specific to each family of alloys.

3.1. Common microstructural features

3.1.1. Solidification cell structures
A distinct feature in a number of alloys that are fabricated using direct AM techniques (i.e., LB-PBF, EB-PBF, and LB-DED) is the

solidification cellular structure, whose length scale can range from ~ 0.1 to 1 μm in LB-PBF and LB-DED alloys, whereas it is generally larger than ~ 5 μm in alloys fabricated using EB-PBF [78–82]. Representative images of the cellular microstructures in 316L produced by LB-PBF [78] are displayed in Fig. 2. The formation of these structures is a consequence of the constitutional undercooling during solidification. When the liquid's temperature ahead of the solid-liquid interface becomes lower than the liquid's freezing temperature due to a high solute concentration, the interface becomes unstable and thus favours dendritic growth [83]. The dendrite's morphology is controlled by the ratio of the temperature gradient (G) and the solidification rate (H). In the case of LB-PBF, where cooling rates are exceptionally high ($>10^6$ K/s), the time available for solidification is insufficient to form secondary dendrite arms leading to cellular morphology [84]. In the LB-DED process in which the cooling rate is comparatively slower, secondary dendritic arms have been observed [79]. The size of the cellular structure depends on G and H, and therefore the process parameters used [84].

The cellular structures observed in several alloys have been associated with solute segregation and dislocation cell structures. As an example, segregation of Cr and Mo to the cell walls in LB-PBF 316L is illustrated in Fig. 2 [85]. The mechanistic reason for such structural features is still a matter of debate and ongoing research. Several mechanisms have been proposed over the last decade, some of which are the following: (i) Solute segregation along cell boundaries during directional solidification, which induces stresses that arise due to solute enrichment. Such stresses are accommodated by the formation of dislocation structure [84,86]. (ii) Solute segregation along the cell boundaries, which is accompanied by a dislocation substructure that is geometrically necessary, resulting in a net misorientation across the cell boundaries [87]. (iii) The dislocation cell structures are a result of the residual stresses developed due to thermal shrinkage. Such structures later provide for enhanced solute diffusion along them resulting in segregation [88]. Cellular growth is accompanied by the rejection of the solutes with a higher melting point; examples are Si in Al-Si alloy [78,80,89], Cr-Mo in 316L and 304L [85] and Ti-Nb in Ni-based superalloys [90]. Bertsch et al. [79] suggest that even though the solute segregation is related to the cellular growth due to directional solidification, the dislocation cells might form independently due to high residual stresses. While the dislocation cells are independent of cell boundaries in the LB-DED 316L, they are aligned in LB-PBF 316L. This difference was attributed to the relatively smaller cell size in the latter, which energetically favours dislocations to pile up along the cell boundaries. Further investigations are needed to ascertain the origin of solute segregation and dislocation cells. For instance, Marangoni surface instability's role in forming a complex cellular structure yet to be investigated in detail [78].

3.1.2. Mesostructures
The mesostructures in AM alloys can manifest not only in terms of the scanning methods employed [91], but also in terms of texture [92], grain boundaries [93,94], and flaw formation [95,96]. Fig. 3a illustrates the mesostructure in a LB-PBF AlSi12 [80]. In the top view, solidified laser tracks are seen, whereas the side views show overlapping melt-pool cross-sections. The melt pool boundaries correspond to the Gaussian profile of the laser beam [96], i.e., the highest depth is located at the centre of the beam. Si segregates to the melt pool boundaries, as shown in Fig. 3b and c and d show the microstructures of LB-PBF Ti6Al4V, where the scan rotation between the successive layers was changed from 90° to 67°, respectively [97]. The prior-β grain (PBG) structure of the two-phase alloy is visible in the top view, where the 90° scan strategy results in a checkerboard type structure, with the width of
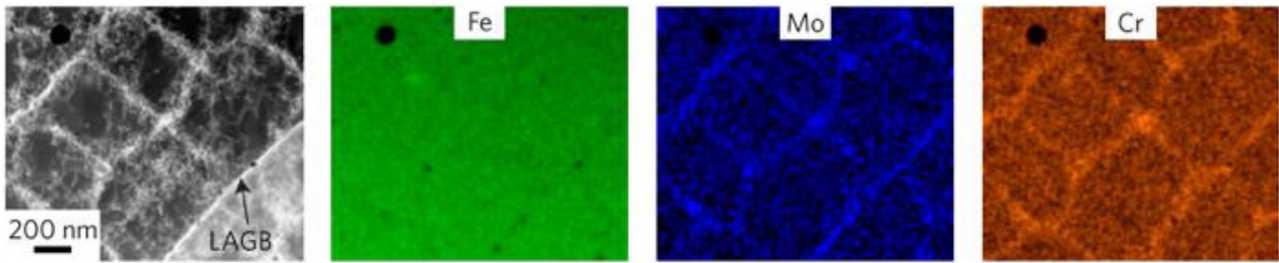
Fig. 2. HAADF STEM image of cellular structure in 316L, where EDS mapping shows segregation of Mo and Cr to the cell boundary. Reprinted with permission from Wang et al. [85]. (Copyright (2018) Springer).
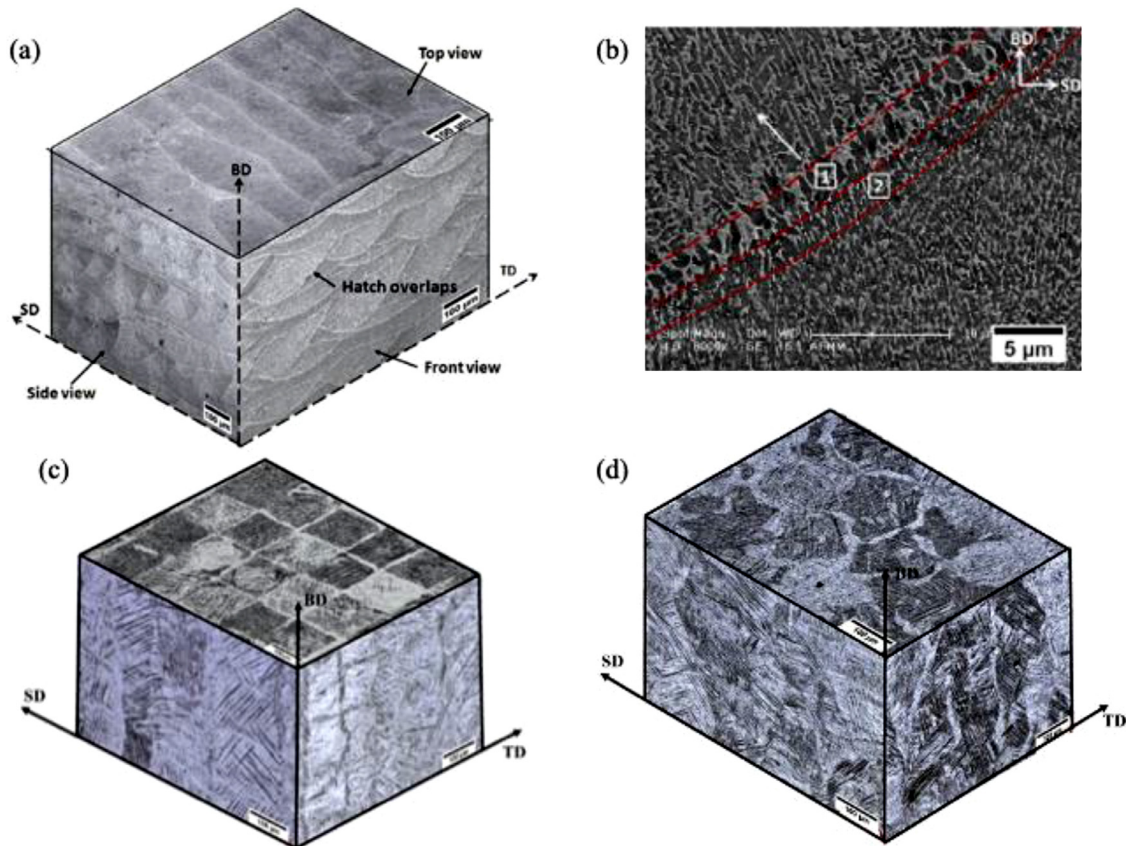

Fig. 3. Representative microstructure of LB-PBF (a) AlSi12 produced by single melt strategy, and (b) SEM image showing melt pool boundary region with Si segregation. Reprinted with permission from Suryawanshi et al. [80]. (c) Ti6Al4V produced using a 90° scan rotation, and (d) 67° scan rotation between subsequent layers. Reprinted with permission from Huang et al. [96]. (Copyright (2016, 2020) Elsevier).

each square corresponding to the scan spacing employed, while the 67° scan rotation results in a more globular and equiaxed structure. The side view shows a columnar PBG structure, which is also seen as a mesostructure, that is commonly reported in AM Ti6Al4V. In many instances, such a mesostructure could impart anisotropy to the tensile, fracture and fatigue behaviour necessitating post-fabrication treatments [3 97–100], as we shall see later.

3.2. Alloy system specific attributes

3.2.1. Ti alloys

The rapid solidification during laser based processes results in a fine microstructure consisting of metastable martensitic α' phase within PBGs, leading to a hierarchical microstructure in most Ti alloys [3,15,97,100,101]. Primary grains tend to extend across an entire PBG. Finer secondary, tertiary, and quartic grains form between primary laths (due to the repeated heating cycles that the solidified alloy layer experiences), resulting in a basketweave structure [102,103]. Columnar PBGs, oriented along the build direction (Z), in LB-PBF Ti6Al4V form due to epitaxial growth along $< 001 >\beta$ [97,104]. They occur due to the absence of heterogeneous grain nucleation sites within the melt pools and the domination of the growth of the grains that are at the bottom of the melt pools during solidification. A transition from the columnar to equiaxed PBG structure can be achieved either by adopting a suitable scan strategy or by adding inoculants that make nucleation of the grains easier [105]. However, significant anisotropy in microstructure and hence properties remain [97,106,107].

The formation of α' or α from β grains follows the $\{ 110 \}\beta || \{ 0001 \}\alpha$ or $< 111 >\beta || < 1120 >\alpha$ Burgers orientation relationship [108,109]. The twelve possible crystallographic variants form randomly from the parent grain [110] and a weak α crystallographic texture in the fabricated alloy is commonly reported.

Table 1

Tensile properties of Ti6Al4V produced by different AM processes and heat treatment conditions.

Process	Source	State	Microstructure	Yield[MPa]	UTS[MPA]	EF[%]
Wrought	[316]	STA	Globular $\alpha + \beta$	900	970	17
Cast	[316]	AB	-	896	1000	8
LB-PBF	[317]	AB	acicular α' in columnar prior-β	$1200 \pm 19^\perp$	$1270 \pm 9^\perp$	$5 \pm 0.5^\perp$
				$1140 \pm 30^=$	$1220 \pm 20^=$	$4.9 \pm 0.6^=$
	[116]	AB	acicular α' in columnar prior-β	$1070 \pm 20^\perp$	$1220 \pm 7.8^\perp$	$8.1 \pm 0.8^\perp$
		SR (480°C for 1 h)	acicular α in columnar prior-β	$1180 \pm 6.1^\perp$	$1290 \pm 3.5^\perp$	$5.66 \pm 0.1^\perp$
		SR (610 °C for 1 h)	ultrafine lamellar $\alpha + \alpha'$ in columnar prior-β	$1110 \pm 17^\perp$	$1180 \pm 15^\perp$	$6 \pm 0.4^\perp$
	[234]	AB	acicular α' in columnar prior-β	$1030 \pm 9.1^\perp$	$1150 \pm 1.8^\perp$	-
				$1010 \pm 8.2^=$	$1150 \pm 4.2^=$	-
		HIP (820 °C for 2 h at 109 MPa in argon, FC)	lamella $\alpha + \beta$ in columnar prior-β	$972 \pm 7.1^\perp$	$1050 \pm 4.1^\perp$	-
				$913 \pm 6.4^=$	$1010 \pm 8.3^=$	-
		HIP (950 °C for 3 h at 109 MPa in argon, FC)	coarse lamella $\alpha + \beta$ in columnar prior-β	$847 \pm 7.8^\perp$	$907 \pm 2.1^\perp$	-
				$812 \pm 4.7^=$	$904 \pm 6.9^=$	-
		BA (1020 °C for 0.5 h, AC)	α colonies $\alpha + \beta$ in globularised prior-β	$717 \pm 2.4^\perp$	$840 \pm 3.5^\perp$	-
				$715 \pm 4.1^=$	$832 \pm 5.9^=$	-
	[318]	SR (650 °C for 3 h)	ultrafine lamellar $\alpha + \alpha'$ in columnar prior-β	$1080 \pm 14^\perp$	$1190 \pm 16^\perp$	$13.6 \pm 1.3^\perp$
		HIP (920 °C at 100 MPa for 2h)	coarsened lamella $\alpha + \beta$ in columnar prior-β	$907 \pm 4^\perp$	$1020 \pm 5^\perp$	$17.7 \pm 0.8^\perp$
	[103]	AN (750 °C for 8 h, FC)	fine lamella $\alpha + \beta$ in columnar prior-β	940 ± 6.4	977 ± 4.5	9.52 ± 2.2
		AN (910 °C for 8 h, FC)	lamella $\alpha + \beta$ in columnar prior-β	890 ± 6.6	950 ± 6.3	11.4 ± 1.3
		AN (910 °C for 8 h, WQ) + AN (750 °C for 4 h, FC	equiaxed α with secondary lamella $\alpha + \beta$ in columnar prior-β	884 ± 2.8	947 ± 5.4	18.5 ± 1.6
	[319]	AB	acicular α' in columnar prior-β	1000 ± 20	1230 ± 15	7.4 ± 0.1
		AN (700 °C for 4 h in vacuum, FC)	fine lamella $\alpha + \beta$ in columnar prior-β	1020 ± 4	1080 ± 4	7.9 ± 1.1
		AN (955 °C for 2 h in argon, WQ) + SR (550 °C for 6 h, AC)	equiaxed α with secondary lamella $\alpha + \beta$ in columnar prior-β	1040 ± 37	1120 ± 39	3.9 ± 1.2
	[224]	HIP (920 °C for 2 h, FC)	lamella $\alpha + \beta$ in columnar prior-β	$914 \pm 20^\perp$	$971 \pm 22^\perp$	$8.6 \pm 2.1^\perp$
		HIP (920 °C for 2 h, WQ) + (500 °C for 1 h)	lamella α with α partially decomposed α' in columnar prior-β	$1088 \pm 9^\perp$	$1194 \pm 4^\perp$	$4.3 \pm 0.3^\perp$
		HIP (920 °C for 2 h, WQ) + (700 °C for 1 h)	lamellae α with secondary fine secondary lamella $\alpha + \beta$ in columnar prior-β	$1012 \pm 6^\perp$	$1047 \pm 1^\perp$	$6.1 \pm 0.8^\perp$
EB-PBF	[320]	AB	lamella $\alpha + \beta$ in columnar prior-β	$823 \pm 0.1^\perp$	$940 \pm 6.5^\perp$	$13.2 \pm 0.7^\perp$
				$852 \pm 5.8^=$	$965 \pm 0.3^=$	$16.3 \pm 0.8^=$
	[317]	AB	lamella $\alpha + \beta$ in columnar prior-β	$869 \pm 7.2^\perp$	$928 \pm 9.8^\perp$	$9.9 \pm 1.7^\perp$
	[321]	AB	lamella $\alpha + \beta$ in columnar prior-β	$812 \pm 12^\perp$	$851 \pm 19^\perp$	$3.6 \pm 0.9^\perp$
	[322]	BA (1110 °C for 2 h, FC)	coarse α colonies + β in globularised prior-β	774 ± 112	913 ± 38	13 ± 2
		BA (1110 °C for 2 h, AC)	α colonies + β in globularised prior-β	847 ± 90	998 ± 52	13 ± 7
		BA (1110 °C for 2 h, WQ)	acicular α' in globularised prior-β	932 ± 80	1200 ± 50	1.8 ± 1.5
	[323]	AB	lamella $\alpha + \beta$ in columnar prior-β	$1000^\perp$	$1070^\perp$	$11^\perp$
				$1010^=$	$1070^=$	$15^=$
		AN (950 °C for 1h, WQ + SR (500 °C for 7 h, AC)	lamella $\alpha + \beta$ in columnar prior-β	$1040^\perp$	$1290^\perp$	$10^\perp$
LB-DED	[230]	AB	α' in $\alpha + \beta$ in columnar prior-β	$1130 \pm 14^=$	$1180 \pm 7^=$	$2.7 \pm 0.9^=$
				$1090 \pm 34^\perp$	$1170 \pm 22^\perp$	$10.7 \pm 0.8^\perp$
	[324]	AB, top of build	fine lamellar $\alpha + \beta$ in columnar prior-β	$945 \pm 13^\perp$	$1040 \pm 12^\perp$	$18.7 \pm 1.7^\perp$
		AB, near the build platform	less fine lamellar $\alpha + \beta$ in columnar prior-	$970 \pm 17^\perp$	$1090 \pm 8^\perp$	$17.6 \pm 0.7^\perp$
				$960 \pm 26^=$	$1060 \pm 20^=$	$13.3 \pm 1.8^=$
	[325]	AN (760 °C in vacuum, AC)	α' in $\alpha + \beta$ in columnar prior-β	$991^=$	$1044^=$	$10^=$

$^\perp$ Parallel to build direction, i.e., specimens loading direction in the Z direction.

$^=$ Perpendicular to build direction, i.e., specimens loading direction in the X or Y direction.

However, primary laths tend to form along the habit planes of approximately $\{334\}_\beta$ and $\{344\}_\beta$ [111,112], resulting in a distinct structural morphology orientated at $\sim 45°$ to the build direction (Z). It has been suggested that an elongated/columnar grain and primary lath morphology will have a larger influence on anisotropy than crystallographic texture [113]. Hence, the underlying properties are affected by the PBG mesostructure and the subsequent α lath formation. To illustrate this, Stephenson et al. [101] employed different scan strategies to promote variant selection during $\beta \rightarrow \alpha$ transformation. The texture of α laths depends on texture of the PBGs and the extent of variant selection [114].

Commonly observed microstructural features of AB Ti6Al4V are summarised in Table 1. The standard approach to transform the metastable microstructure that is prevalent in the AB state of Ti6Al4V is through the use of post-processing heat treatments, during which V diffuses out of the saturated α' to facilitate the formation of β along the α lath boundaries when the cooling rates

are sufficiently low [98,115]. Heat treatment of AM Ti6Al4V is generally categorised into three distinct groups: (a) stress-relieving (SR) treatments carried out between 480 and 650 °C, (b) recrystallisation AN conducted from 705 to ~ 975 °C, i.e., just below the β-transus temperature (T_β), and (c) β annealing (β-AN) performed above 975 °C [103,116]. The microstructural responses to heat treatments are summarised in Table 1. In SR, α' can start to transform towards α. At higher SR temperatures, β precipitates start forming along the lath boundaries and the hierarchical structure starts to decompose [116]. Annealing results in coarsening of α lath structure (consequently, the dissolution of the hierarchical structure) and formation of β along the lath boundaries in significant amounts. β-AN results in a colony type structure, which is commonly seen in conventionally produced Ti6Al4V. While the heat treatments performed below T_β do not alter the PBG mesostructure, those conducted above results in recrystallisation, globularisation and significant PBG growth [98,115]. Duplex
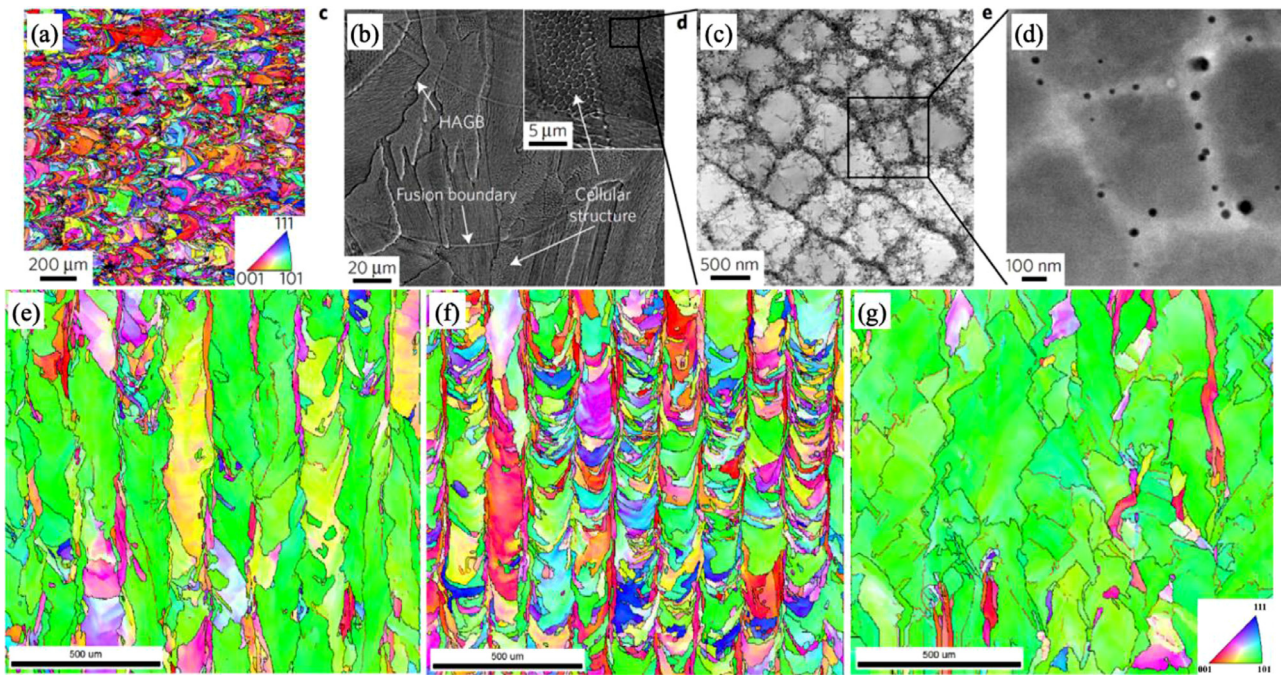
Fig. 4. Micrographs of 316L showing hierarchical structure. Reprinted with permission from Wang et al. [85]. (a) IPF map showing grain orientation, (b) SEM micrograph showing high angle grain boundary across the melt pool, (c) TEM micrograph showing cellular structure, (d) oxides impurities on cellular boundaries. IPF map of 316L showing effect of melt pool on the texture. (e) melt pool width 175 μm, depth 75 μm (f) melt pool width 175 μm, depth 125 μm, and (g) melt pool width 250 μm, depth 125 μm. Reprinted with permission from Andreau et al. [92] (Copyright (2018) Springer and Elsevier).

heat treatments (annealing at 910 °C followed by a water quenching (WQ) and then another annealing at 750 °C followed by air cooling (AC)) have been employed to obtain a bimodal microstructure consisting of fragmented equiaxed primary α grains in a matrix of lamellar secondary $\alpha + \beta$ in LB-PBF Ti-6Al-4V [26,113,117]. As we will discuss later, bimodal microstructures offer a good compromise between ductility and strength and enhance the near-threshold fatigue crack growth resistance.

3.2.2. Steels

Fig. 4 illustrates the hierarchical nature of the microstructure in PBF 316L, which consist fine equiaxed grains within the melt pools and columnar grains at their boundaries. The size range of the characteristic microstructural features in PBF and DED processed steels is wide. At the one end, their size can be in the same order as the melt pool size (Fig. 4a). On the finer scale, they can be few tens of nm, corresponding to those of the solidification cells (Fig. 4b and c) [4,12,85]. The size of the cellular structures increases with decreasing scanning speed, due to the reduced solidification rate [87]. DED processes typically result in the formation of larger grains due to the comparatively larger melt pool size and slower scan speeds. [118].

The crystallographic texture in AM steels could be modified by varying the process parameters [12]. For example, single melt or cross-hatch melt strategies result in a columnar microstructure with strong texture [4,92]. Conversely, increasing the scan speed could result in shorter columnar grains, with a weaker texture in the transverse direction [119]. The anisotropic microstructure is related to epitaxial growth of the austenitic phase in the < 001 > direction [3,12]. Olivier et al. [92] demonstrated that epitaxial growth could be reduced by changing the melt pool's shape and size, as shown in Fig. 4e– g. The crystallographic texture can also be altered by changing the process parameters to some extent [94,120,121]. For example, Zhongji et al. [122] engineered a < 011 > crystallographic texture in place of the preferred < 001 >

texture by employing a multi-scan strategy to produce a stable, deep melt pool with a width-to- height ratio of 2:1.

Commonly observed microstructural phases in AM steels are summarised in Table 2. The alloys 304L and 316L typically exhibit a completely austenitic microstructure after fabrication, specifically when fabricated using LB-PBF [123]. Abd-Elghany et al. [124] did not observe any precipitation of chromium carbides at grain boundaries of LB-PBF 304L. When LB-DED is used, however, retained δ-ferrite (~11 vol.%) that forms along the cellular boundaries was observed in the AB 316L specimens, [125,126]. Subsequent heat treatment at 1150 °C for 2 h followed by air cooling dissolves the cellular segregation and results in recrystallised austenite grains that are equiaxed. Post-processing heat treatments typically improve the grain boundary characteristics of these alloys and thereby tensile and fatigue properties. For equiaxed grains to form, recrystallisation above the solutionising temperature of $\sim$ 1050 °C is required [93].

LB-PBF 18Ni300 maraging steel also exhibits a hierarchical microstructure, with solidification cells inside a martensitic microstructure [127–129]. In the AB condition, the microstructure consists of both martensite and austenite, and no precipitates or small clusters of atoms are observed, indicating a cooling rate high enough to suppress precipitation. This leads to a comparably soft and ductile alloy in the AB state [12]. However, there are indications of early stages of precipitation in the DED material, accompanied by an increased hardness [130]. Solutionising and age hardening heat treatments (815–840 °C for 1 h, AC, 490–530 °C for 8 h, AC), which are similar to those used for conventionally produced maraging steels, are necessary for imparting high strength [129,131,132]. These heat treatments result in the formation of martensite with intermetallic precipitates. With increasing ageing temperature and time, the volume fraction of retained austenite increases by the process of austenite reversion [129,133].

In 17-4 PH steel, the size of the martensitic laths depends on the solidification rate [134]. The lack of coherent Cu precipitates in the AB parts makes ageing treatment necessary to improve this

Table 2
Tensile properties of several steel grades, generated by different AM processes and heat treatment conditions. Reported austenite (A), martensite (M), and omega (σ) phases listed.

Alloy	Process	Source	Condition	Microstructure	YS [MPa]	UTS [MPa]	EL [%]
316L	Wrought	[235]	AN	A	170	485	40
	LB-PBF	[326]	AB	A	430⊥	550⊥	64⊥
		[271]	AB	A	462⊥	565⊥	53.7⊥
		[226]	AB	A	590±17	705±15	44±7
			AN (1095 °C for 1 h in vacuum, FC in argon)	A	375±11	635±17	51±3
		[40]	AG (550 °C for 1 h)	A	511±14⊥ / 430±11=	621±11⊥ / 510±20=	20±2⊥ / 12±1=
		[327]	AB	A	325⊥ / 415=	450⊥ / 565=	8.6±7.3⊥ / 35±3.1=
			HIP (1125 °C for 4 h at 137MPa, FC)	A	225⊥ / 225=	515⊥ / 570=	28.6±17⊥ / 46.7±4.5=
	EB-PBF	[237]	AB	A, F	334±16⊥ / 396±9.0=	572±19⊥ / 652±8.5=	29.3±5.2⊥ / 30.6±3.0=
	LB-DED	[82]	AB	A	253±3⊥	509±5⊥	59±3⊥
		[123]	AB	A	530±5=	670±6=	34±1=
				A	469±3=	628±7=	31±2=
		[328]	AB	87.7% A, 7.84% F, 4.45% σ	533±23=	235±6=	48±2=
			AN (1000 °C for 1 h, WQ)	89.1% A, 3.92% F, 6.98% σ	549±18=	255±25=	41±0=
			AN (1200 °C for 1 h, WQ)	96.0% A, 3.96% F	474±4=	215±12=	57±8=
			AN (1200 °C for 4 h, WQ)	A	494±6=	204±10=	70±5=
		[118]	AB	91% A, 9% F	410±5⊥	640±20⊥	34±4⊥
			AN (1150 °C for 2 h, AC)	A	340±15⊥	610±5⊥	42.5±0.5⊥
	BJP	[40]	AG (550 °C for 1 h)	97.7% A, 2.63% F	193±2.8⊥ / 197±3.2=	548±3.8⊥ / 553±5.7=	67.6±2.8⊥ / 76±2.8=
304L	Wrought	[235]	AN	A	170	485	40
	LB-PBF	[329]	AB	A, F	540±15⊥	660±20⊥	36±12⊥
		[330]	AB	A	568±2=	716±1=	41.7±1.1=
17-4PH	Wrought	[331]	ST + AG	M	1170	1310	10
	LB-PBF	[238]	AB	M	1190⊥	1370⊥	8.3⊥
		[332]	AB	64% M, 36% A	661 ± 24=	1260 ± 3=	16.2 ± 2.5=
			AG (480 °C for 1 h, AC)	59.5% M, 40.5% A	945 ± 12=	1420 ± 6=	15.5 ± 1.3=
			AG (620 °C for 4 h, AC)	94.4% M, 5.6% A	1010 ± 15=	1320 ± 2=	11.1 ± 0.4=
			ST (1040 °C for 0.5 h, AC)	M	939 ± 9=	1190 ± 6=	9 ± 1.5=
			ST (1040 °C for 0.5 h, AC) + AG (480 °C for 1 h, AC)	96.7% M, 3.3% A	1350 ± 18=	1440 ± 2=	4.6 ± 0.4=
		[239]	AG (600 °C for 2 h)	28% M, 72% A	600=	1300=	28=
18Ni300 steel	Wrought	[12]	SA		828 ± 68	1000 ± 130	11.5 ± 5.5
			SA + AG		1930 ± 140	1960 ± 150	8 ± 3
	LB-PBF	[333]	AB	98% M, 2% A	713⊥ / 851=	1060⊥ / 1020=	11.3⊥ / 9.63=
			ST (815 °C for 1h, AC) + AG (520 °C for 5 h, AC)	90.7% M, 9.3% A	920⊥ / 886 =	1530⊥ / 1550 =	10.6⊥ / 10.7 =
		[334]	AB	89.7% M, 10.3% A	915 ± 7	1170 ± 7	12.4 ± 0.14
			AG (490 °C for 6 h, AC)	98% M, 11% A	1970 ± 11	2020 ± 9	3.28 ± 0.05
			ST (840 °C for 1 h, AC)	M	962 ± 6	1030 ± 5	14.4 ± 0.35
			ST (840 °C for 1 h, AC) + AG (490 °C for 6 h, AC)	93.5% M,6.5 A	1880 ± 14	1940 ± 8	5.60 ± 0.08
		[335]	AB	M	915 ± 13=	1190 ± 10=	6.14 ± 1.3=
			ST (815 °C for 0.5 h, AC) + AG (460 °C for 8 h, AC)	84.6% M 15.6% A	1960 ± 43=	2020 ± 58=	1.51 ± 0.2=
			ST (815 °C for 0.5 h, AC) + AG (540 °C for 8 h, AC)	78.7% M 21.3% A	1550 ± 100=	1660 ± 88=	1.77 ± 0.1=
		[336]	AB	M	1060 ± 20⊥ / 975 ± 75=	1160 ± 42⊥ / 1060 ± 50=	12 ± 0.1⊥ / 10.2 ± 1.9=
			ST (840 °C for 1 h, AC)	M, A	808 ± 7.5⊥ / 805 ± 5=	970 ± 20⊥ / 975 ± 25=	13 ± 0.5⊥ / 11.9 ± 0.1=
			ST (840 °C for 1 h, AC) + AG (490 °C for 6 h, AC)	M, A	1750 ± 35⊥ / 1750=	1820 ± 20⊥ / 1850=	4.5 ± 0.1⊥ / 5.1=
		[337]	AB	94.2% M, 5.8% A	1210 ± 99	1290 ± 110	13.3 ± 1.9
			AG (480 °C for 5 h, AC)	90.6% M, 9.4% A	1200 ± 32	2220 ± 73	1.6 ± 0.26
	DED	[338]	AB	M	-	959 ± 20	-
			ST (830 °C for 1 h, AC) + AG (490 °C for 10 h, AC)	M, A	-	1560 ± 17	0.12 ± 0.05

⊥ Parallel to build direction, i.e., specimens loading direction in the Z direction.
= Perpendicular to build direction, i.e., specimens loading direction in the X or Y direction.

Table 3

Tensile properties of Inconel 625 and 718, generated by different AM processes and heat treatment conditions.

Alloy	Process	Source	Condition	Microstructure	YS [MPa]	UTS [MPa]	EL [%]
Inconel 718	Wrought	[339]	-		1100 ± 70	1340 ± 60	16 ± 5
	Cast	[147]	-		550	965	23
	LB-PBF	[148]	AB	fine dendritic structure within visible melt pool boundaries, γ'' precipitates along grain boundaries	830$^=$	1120$^=$	25$^=$
			AN (982 °C for 0.5 h in vacuum) + HIP (1163 °C for 4 h at 100 MPa in argon)	columnar structure, with regularly distributed γ'' precipitates	850$^\perp$ 890$^=$	1140$^\perp$ 1200$^=$	28$^\perp$ 28$^=$
		[340]	AB	fine dendritic structure within visible melt pool boundaries	900 ± 10$^\perp$	1150 ± 10$^\perp$	23 ± 4$^\perp$
			ST (980 °C for 1 h, AC) + AG (720 °C for 8h, FC; 620 for 8 h, AC)	columnar structure, precipitation of needle-like δ along grain boundaries and formation of laves phase	1130 ± 30$^\perp$	1320 ± 40$^\perp$	16 ± 6$^\perp$
		[241]	AG (720 °C for 8 h, FC; 620 °C for 10 h, AC)	columnar structure, precipitation of γ'/γ'' and small amounts of needle-like δ along grain boundaries	572 ± 44$^\perp$ 643 ± 63$^=$	904 ± 22$^\perp$ 991 ± 62$^=$	19 ± 4$^\perp$ 13 ± 6$^=$
			ST (1100 °C for 1 h, WQ) + AG (720 °C for 8 h, FC; 620 °C for 10 h, AC)	homogenization of γ decorated with MC carbides	1070 ± 42$^\perp$ 1160 ± 2$^=$	1320 ± 6$^\perp$ 1380 ± 66$^=$	19 ± 2$^\perp$ 8 ± 6$^=$
	EB-PBF	[242]	HIP (1200 °C for 4 h at 120MPa) + ST (1066 °C for 1 h in vacuum) + AG (760 °C for 10 h followed by 650 °C for 20 h), using linear heat source	columnar structure, γ'' precipitates along grain boundaries	1010$^=$ 752$^\perp$ 834$^=$	1080$^=$ 834$^\perp$ 1060$^=$	38$^=$ 17$^\perp$ 20$^=$
			..., using point heat source	equiaxed structure, γ'' precipitates along grain boundaries	827$^\perp$	1050$^\perp$	8.5$^\perp$
		[341]	HIP (1200 °C for 4h at 100MPa) + ST (1066 °C for 1 h) + AG (760 °C for 10 h followed by 650 °C for 10 h)	columnar structure, γ'' precipitates along grain boundaries	894 ± 24$^=$ 925 ± 20$^\perp$	1060 ± 83$^=$ 1140 ± 24$^\perp$	11.5 ± 6.9$^=$ 15.7 ± 4.3$^\perp$
	LB-DED	[342]	ST (1020 °C for 4 h) + AG (720 °C for 8 h, FC to 620 °C for 8 h, AC)	columnar structure, precipitation of needle-like δ along grain boundaries	-	1310$^\perp$	24$^\perp$
Inconel 625	Wrought	[343]	-	-	413 ± 8.3	914 ± 17	70.2 ± 3.6
	LB-PBF	[240]	AB	fine columnar structure	652 ± 10$^=$	925 ± 13$^=$	32 ± 3$^=$
			AN (900 °C for 1 h)	coarsened columnar structure, γ'' precipitates	567 ± 15$^=$	869 ± 7$^=$	38 ± 1$^=$
			AN (1100 °C for 1 h)	equiaxed structure	409 ± 14$^=$	886 ± 11$^=$	56 ± 5$^=$
	EB-PBF	[344]	AB	columnar structure, γ'' precipitates	410	750	44
			HIP (1120 °C for 4 h at 100MPa)	equiaxed structure, formation of laves phase	330	770	69
	LB-DED	[240]	AB	fine columnar structure	732 ± 23$^=$	1070 ± 5$^=$	26 ± 2$^=$
			AN (900 °C for 1 h)	coarsened columnar structure, γ'' precipitates	654 ± 15$^=$	1080 ± 2$^=$	27 ± 2$^=$
			AN (1100 °C for 1 h)	equiaxed structure, MC carbides	532 ± 22$^=$	991 ± 13$^=$	43 ± 1$^=$
	BJP	[345]	ST (1280 °C for 4 h in vacuum)	equiaxed structure, precipitation of γ'/γ'' and δ along grain boundaries	327 ± 11	612 ± 19	40.9 ± 3.1
			ST (1150 °C for 2 h)	equiaxed structure, precipitation of γ'/γ'' and δ along grain boundaries	311 ± 23	587 ± 57	45.1 ± 3.3
			AG (745 °C for 20 h)	equiaxed structure, precipitation of γ'/γ'' along grain boundaries	373 ± 14	647 ± 27	35.8 ± 5.9
			AG (745 °C for 60 h)	equiaxed structure, precipitation of γ'/γ'' along grain boundaries	392 ± 14	647 ± 29	30.1 ± 6.7

$^\perp$ Parallel to build direction, i.e., specimens loading direction in the Z direction.

$^=$ Perpendicular to build direction, i.e., specimens loading direction in the X or Y direction.

steel's properties [135,136]. Solutionising followed by ageing results in microstructures of both the wrought and AM 17–4 PH steels being similar [122,137,138]. Merely ageing 17–4 PH steel in its AB state also decreases the retained austenite fraction, but not beyond 20% [139]. Moreover, the range of martensite and austenite phase fractions is highly dependent on the ageing time and duration. A heat treatment of 1040 °C for 4 h followed by WQ and aging at 482 °C for 1 h results in a martensitic microstructure with Cu nano precipitates [137–139].

3.2.3. Ni-based Superalloys

Ni-based superalloy parts have been successfully produced using all the major AM processes [13,77,140,141], with Inconel 718 and 625 being the most widely investigated alloys [4,142]. The microstructures in them vary from equiaxed to columnar, depending on the melt pool geometry and process parameters employed, as summarised in Table 3 [142,143]. The grain morphology can be controlled to some extent during the AM process. Using EB-PBF Inconel 718, Körner and co-workers [144–146] have shown that variations in the scanning strategy can produce either a highly textured columnar grain structure or an equiaxed fine-grained structure with a less pronounced texture. Moreover, Gotterbarm et al. [144,146] have demonstrated the ability to grow single crystals through a carefully designed and controlled temperature gradient along a μ-Helix.

Precipitation strengthening does not occur in the AB state as rapid cooling through the precipitation temperature does not allow for γ' and γ'' phases formation [147,148]. Rapid solidification also results in micro-segregation of Nb, Ti and Mo along the cellular boundaries, as illustrated in Fig. 5a–c [4,13,140]. This can lead to the formation of the Laves phases along the cell boundaries or δ phase at cell and grain boundaries [149,150]; some of these phases are detrimental to the mechanical performance of the alloy [4,149]. Moreover, the Laves phases entrap some of the available Nb, Mo
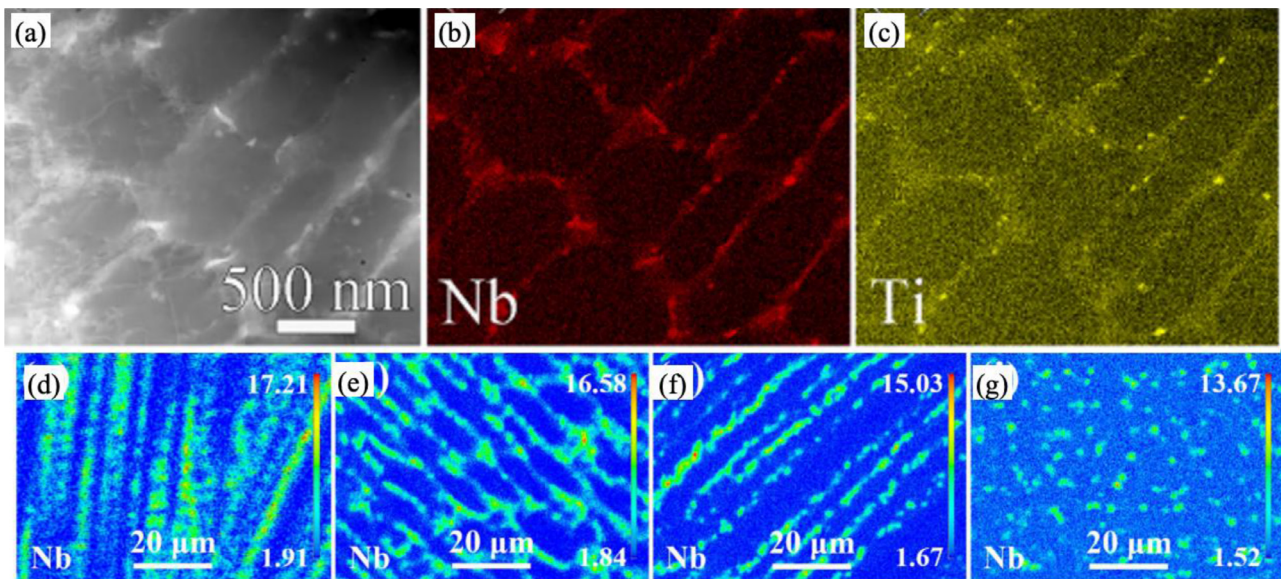
Fig. 5. (a) HAADF-STEM micrograph and STEM-EDX map highlighting segregation of (b) Nb and (c) Ti along the cellular boundaries. Reprinted with permission from Gallmeyer et al. [**140**]. EPMA elemental map showing segregation of Nb in (d) AB specimens, (e) after ageing (AG, 720 °C for 8 h, 620 °C for 8 h), (f) after solutionising and ageing (STA, 980 °C for 1 h, AG), (g) after homogenisation and solutionising (HSTA, 1150 °C for 1 h, STA). Reprinted with permission from Yu et al. [**153**]. (Copyright (2020) Elsevier).

and Ti, which are important for the forming of γ' and γ'' precipitates during ageing [4].

Since the dissolution of Laves phases is necessary to achieve peak strengthening, post-processing heat treatment becomes necessary [140,151]. However, the standard heat treatment recommended for wrought Inconel does not directly apply to AM Inconel. For example, in Inconel 718, the microstructure maintains its columnar nature and traces of the mesostructure, i.e., the layered build of the material. The effect of irregular precipitation of γ' and γ'' phases is marked by intensive etching of interdendritic areas and boundaries of columnar grains during the preparation of the specimens for metallography. Small quantities of needle-like δ-Ni$_3$Nb precipitates appear in the interdendritic regions [140]. Both double ageing and solutionising (at 980 °C) heat treatments were shown to be ineffective in erasing the Nb segregation along the cell boundaries. A homogeneous distribution of Nb could only be achieved after solutionising at temperatures greater than 1050 °C for 1 h and air cooling. Such high solutionising temperatures can lead to grain growth while dissolving the Laves phases; γ' and γ'' precipitates form during subsequent ageing [4,151–153], as shown in Fig. 5d–g.

3.2.4. Al alloys

Among the high strength Al alloys, AlSi12 and AlSi10Mg, together with AA2024 and AA7050, are the most common ones adapted for AM processes. Conventionally produced Al-Si alloys contain significantly coarser Si particles in their microstructure (as compared to those in the AM alloys) [154]. Due to the high cooling rate during PBF and DED processes, Al solidifies through the segregation of Si that, in turn, leads to Si enrichment around the primary Al phase and, consequently, the formation of cellular structures, as summarised in Table 4. The shapes of the cells appear columnar along melt pool boundaries and equiaxed within the scan tracks. Fine Si particles are located primarily at cellular boundaries, as illustrated in Fig. 3a and b [10,80]. The processing parameters influence the microstructure and melt pool morphology. For LB-PBF AlSi10Mg, Paul et al. [155] reported that increasing hatch spacing and layer thickness results in larger columnar grains with a wider cellular sub-structure,

whereas the scan strategy controls the melt pool arrangement and the formation of a melt pool geometry dominated mesostructure.

The Si particle size has been shown to vary with the printed part size; prolonged durations at elevated temperatures allow for the precipitation of Si in the columnar Al grains. The Si concentration in solid solution is $\sim$ 7 wt% (compared to 1.6 wt% in conventionally manufactured alloy), which results in a significant increase in strength for AM Al-Si alloys due to solid solution strengthening [10]. Si particles' heterogeneous distribution in AB parts can simultaneously be both beneficial and detrimental for its mechanical performance [80,156]. Thus, various heat treatments have been employed to improve mechanical properties [10], as we will discuss later. Fig. 6a shows the network of eutectic Si particles segregated along the cellular boundaries, which remains even after a heat treatment (Fig. 6b) [157,158]. However, SR heat treatment at 320 °C for 2 h partially breaks the Si network and coarsens the precipitates (Fig. 6c) [157]. While the standard T6 heat treatment has been shown to eliminate the Si network, solutionising at temperatures > 500 °C, however, releases significant Si from the solid solution, resulting in the formation of coarse Si particles at the grain boundaries (Fig. 6d) [89,156–158].

4. Process-related attributes

The process-related attributes in AM alloys are controlled by an extensive range of process parameters and physical phenomena that include laser exposure strategies, powder quality and the feed system, binder properties in the case of BJP, and build platform temperature. Moreover, part design, orientation, and support structures affect the quality of the final product in terms of flaws (for example keyholing and lack-of-fusion), residual stresses, and surface finish. In addition to the microstructure, these attributes can significantly affect the mechanical performance of the material, especially in the context of the in-service fatigue performance of a part. In this section, we summarise the common process related attributes across several AM systems.

Table 4

Tensile properties of AlSi12 and AlSi10Mg, produced using different AM processes and heat treatment conditions.

Alloy	Process	Source	Condition	Microstructure	YS [MPa]	UTS [MPa]	EL [%]
AlSi12	Cast	[346]	-	eutectic	130	240	1
	LB-PBF	[249]	AB	fine cellular α-Al with intercellular eutectic Si	260$^\perp$	380$^\perp$	3$^\perp$
			AN (450 °C for 6 h)	coarsened cellular α-Al with large Si-agglomerates	95$^\perp$	145$^\perp$	13$^\perp$
AlSi10Mg	Cast	[346]	-		140	240	1
	LB-PBF	[347]	AB	fine cellular α-Al with intercellular eutectic Si	301$^=$ 270$^\perp$	401$^=$ 337$^\perp$	4.30$^=$ 4.09$^\perp$
		[250]	AB	fine cellular α-Al with intercellular eutectic Si	230 ± 5$^\perp$ 240 ± 8$^=$	328 ± 4$^\perp$ 330 ± 4$^=$	6.2 ± 0.4$^\perp$ 4.1 ± 0.3$^=$
			AN (530 °C for 5 h, FC)	coarsened cellular α-Al with large Si-agglomerates	72 ± 7$^\perp$ 131 ± 9$^=$	113 ± 3$^\perp$ 227 ± 4$^=$	12.6 ± 0.9$^\perp$ 6.9 ± 0.8$^=$
			AN (530 °C for 5 h, FC) + AG (160 °C for 12 h)	coarsened cellular α-Al with small intercellular Si	245 ± 8$^\perp$	278 ± 2$^\perp$	3.6 ± 0.8$^\perp$

$^\perp$ Parallel to build direction, i.e., specimens loading direction in the Z direction.

$^=$ Perpendicular to build direction, i.e., specimens loading direction in the X or Y direction.
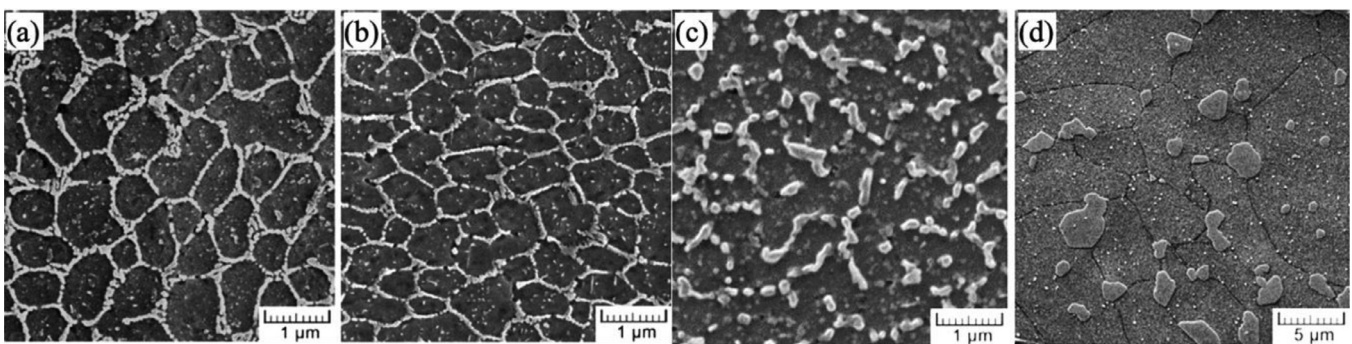
Fig. 6. SEM Micrograph showing Si particle distribution in (a) AB condition, (b) AN (160 °C for 5 h), (c) after SR (320 °C for 2 h), and (d) after T6 treatment, (510 °C for 6 h), followed by AG at (170 °C for 4 h). Reprinted with permission from Fousová et al.[157]. (Copyright (2018) Elsevier).

4.1. Flaws

ASTM E3166 [159] characterises flaws as porosity (that may be isolated or in clusters near the surface or deeply embedded), lack-of-fusion (LOF) discontinuities (that may be between or across layers), start-stop errors, inclusions, layer shifts, under/over-melted material). These flaws commonly result in a loss in density, however, they may also present in the form of cracks. Current AM technologies can readily achieve densities *up to* 99.9% when optimal process parameter combinations are used [16,160]. For example, the reported porosity levels in Inconel 625 are less than 0.12% for LB-PBF [161], 0.01% for DED [162,163] and ∼ 1% for BJP [164]. The generally higher densities obtained in the DED processes are attributed to the larger track widths and layer thicknesses and smaller velocity of the heat source. In BJP, the final density of the part relies directly on the packing density in the green stage, and porosity occurs due to the powder quality and the sintering process [5]. Notably, a compromise between density and shrinkage exists. When a highly dense part is essential, higher temperature and longer sintering times are used, which allow for near-fully dense parts, but with higher dimensional shrinkage [77,164].

Many studies aim at optimising the process parameters, such as the heat-source characteristics, exposure strategy, layer thickness, and part orientation to achieve the highest possible density with the smallest flaw size. An intricate balance between the energy input and melting of the powder material exists; insufficient energy results in partial melting of the powders, resulting in the formation of 'lack-of-fusion (LOF)' and 'unmolten powder particle' type flaws. Excess energy input, in contrast, results in an unstable melt pool

that can lead to spatter and vaporisation and consequently formation of gas-entrapped and keyhole type flaws [165–167]. Non-optimal parameters can also lead to the formation of discontinuous tracks, weak inter-line metallurgical bonding, and delamination [168].

Flaws act as crack initiation sites under cyclic loading conditions and hence adversely affect the fatigue life [168–172]. The flaw diameter (size), shape (including sharp radii and crack-like features) and location (including nearest neighbour flaw and distance to the free surface) play a critical role, and the use of density as a single material parameter is insufficient for a complete assessment of the flaw's influence on the fatigue life of AM alloys. Recognising this, detailed understanding the morphological characteristics of flaws has been the focus of several recent studies [16,165,173,174]. Fig. 7 summarises the observed flaw morphologies in LB-PBF 316L [175]. The three critical characteristics that describe flaw attributes are sphericity (or circularity), aspect ratio, and size (diameter) [165]. Sphericity is a measure of a flaw's irregularity or deviation from a perfect spherical shape and is taken as the ratio of the surface area of a sphere to that of the flaw (with identical volumes). Circularity is sphericity's two-dimensional counterpart and is the ratio of the cross-sectional area of the flaw to the square of its circumference. Aspect ratio is the ratio of the smallest to largest dimension of the flaw, which is computed using a bounding box surrounding the flaw to account for highly irregularly shaped flaws. Pore diameter is its largest dimension and describes its physical size.

The majority of gas flaws is near-spherical and therefore has a high sphericity and a high aspect ratio. LOF flaws, on the other hand, are irregular in shape and are present with sharp edges.
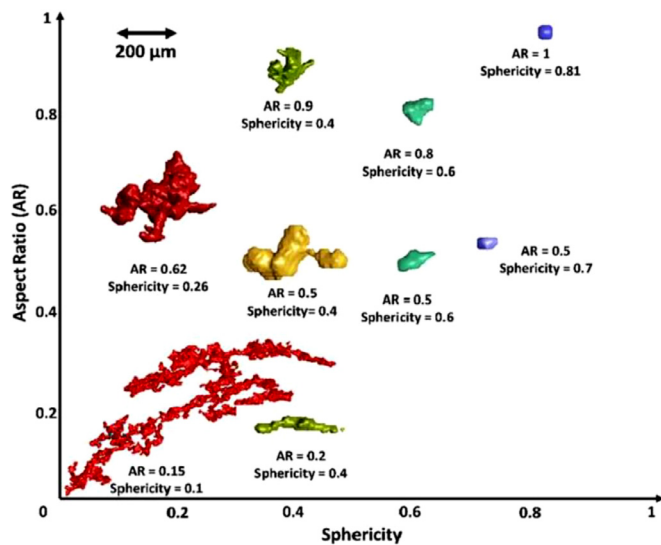
Fig. 7. Aspect ratio (AR) vs sphericity of defects gathered from micro-CT results for LB-PBF Ti6Al4V. Reproduced with permission from Sanaei et al. [165]. (Copyright (2019) Elsevier).

They may contain unmolten powder particles within them and typically have low sphericity and aspect ratio. The size of gas flaws generally correlates with the melt pool size. Often, LB-PBF results in smaller flaws as compared to EB-PBF and LB-DED. The size of LOF flaws is typically in the same order as the hatch spacing [97]. They, however, can reach orders of millimetres in size with a very low sphericity and aspect ratio [165,176]. Thus, LOF defects are considered as the main contributors to poor fatigue failure in PBF and DED processes. In BJP, flaw sizes are significantly smaller and have high aspect ratios.

Kumar and Ramamurty [168] investigated the effect of process parameter combinations on the porosity distribution in LB-PBF Ti6Al4V. Reconstructed micro-CT images show that the flaw sizes and distribution are sensitive to the process parameters utilised. While the flaws were observed to align in the build direction when a scan rotation of 90° is used, they are randomly distributed for scan rotation of 67°, as seen in Fig. 8a and b, even though the volumetric energy densities are similar in both the cases. Kumar and Ramamurty rationalized this observation by recourse to combined effect of Marangoni convection and Rayleigh instability [177]. The frequency of relatively big flaws can be significantly reduced by employing scan rotation of 67° or by reducing the hatch spacing to ensure a larger overlap between adjacent melt pools as shown in Fig. 8c [168].

4.2. Surface roughness

The combination of the layer-by-layer fabrication process along with the half-fused particles attached to the surface and the presence of sub-surface and surface-connected defects result in a highly rough surface for AM alloy parts, as can be seen in Fig. 9. Surface roughness is influenced by the process type and parameters used, powder size, layer thickness, the geometry of the part, and the orientation of the surface with respect to the build direction [16,178]. For example, layering at an inclined angle results in a surface with the 'staircase' morphology, whose slope or curvature is approximated by the position of each layer [176,178]. Additionally, up- and down-facing sides result in different surface morphologies due to the orientation to the heat-source with respect to the build platform; the roughness is significantly higher for down-facing sides compared to up-facing sides [179]. In the PBF processes, for example, down-facing sides are built either on loose

powder or support structures and therefore will result in distinct roughness characteristics.

Generally, the DED process results in the best surface finish and EB-PBF the worst. For example, the reported values of mean surface roughness (R_a) for Ti6Al4V are 18.5 $\pm$ 6.5 μm for LB-DED [38,180], 35 $\pm$ 12.3 μm for LB-PBF [181,182], and 131 $\pm$ 45.5 μm for EB-PBF [183]. (For further comparison, R_a in BJP 316L is 3.73 μm [184].) Laser- and electron beam-based processes use finer powder and layer thicknesses that are prone to 'satellite' formation due to the sintering of powder at the part edges [179]. However, the DED technologies are limited in the use of near net shapes (i.e., shapes produced close to the desired part geometry followed by machining to deliver the final geometry) due to a significantly larger line width and layer height.

While a high surface roughness may be beneficial in some instances, such as biomedical applications where osseointegration is promoted through a rough surface [185], its influence has been shown to adversely—and severely—affect the fatigue performance of AM parts [16]. Like porosity, the aberrations in the surface result in stress concentrations that lead to localised plastic deformations that promote early fatigue crack initiation. Kantzos et al. [186] showed that in LB-PBF Ti6Al4V, stress concentrations caused by the surface asperities can result in a 15-fold amplification of the equivalent applied von Mises stress. Interestingly, this study also notes that the most detrimental surface features are near-surface flaws and surface notches, demonstrating an irrelevance of the adhered powder to the mechanical response. This observation was confirmed by a study by Fatemi et al. [187] under axial, torsional, and combined axial-torsional loadings. Similarly, Beretta et al. [188], who investigated the effect of part orientation in LB-PBF AlSi10Mg, found that specimens with up-facing surfaces exhibit significantly better fatigue performance than those with down-facing surfaces, which include notch-like features. Edwards et al. [189] show that rough surface has a dominant role in crack initiation in AB specimens, while internal cracks have a significant role in the case of machined specimens.

4.3. Residual stresses

Unlike BJP in which the residual stresses in the built part are negligible, the PBF and DED processes are plagued with high residual stresses, which is exacerbated by the fact that they can often vary significantly from one location of the built part to another. These stresses may cause in-situ cracking, delamination, part warpage, and potential build-failure. Such high residual stresses are a result of the localised heat input and rapid cooling that are intrinsic to these processes. The expansion of a localized zone upon being heated rapidly by a high energy beam is suppressed by the neighbouring material, which usually causes compressive plastic strains. Subsequent rapid cooling of the molten alloy and the associated contraction results in high tensile stresses [191]. The localised nature of the heating and cooling cycle also results in a highly irregular residual stress field through the volume of the built part.

Measurements, using neutron diffraction in DED 316L, have shown that residual stresses can be in the order of 50–80% of the yield strength of the alloy [192]. Similar values are reported in LB-PBF Ti6Al4V [193–197] and Inconel 718 [198]. These stresses are highest in magnitude along the build direction (Z) [196], compressive in the part centre, tensile at the outer free surfaces, and more concentrated near the build platform interface [171,192,195,199–201]. If the build platform is heated, however, they can be reduced by an order of magnitude [202,203].

The magnitude of residual stresses increases with increased length of the scan lines. Keeping this in view, the most common approach to reduce the stress build-up during fabrication is to im-
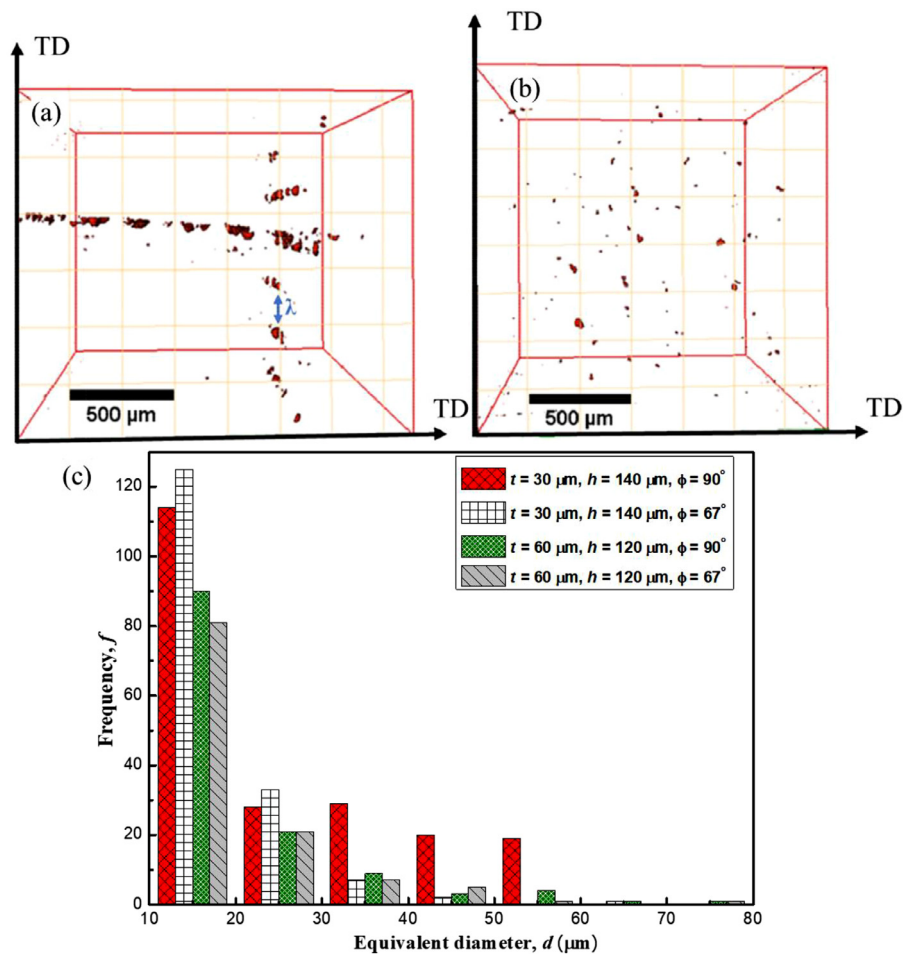
Fig. 8. Top view of reconstructed Micro CT images of LB-PBF Ti6Al4V specimens produced with layer thickness (t) = 30 μm, hatch spacing (h) = 140 μm (a) scan rotation (ϕ) = 90°and (b) ϕ = 67°, (c) Histogram showing flaw size distribution for four different combinations of process parameters used during the LB-PBF process. Reproduced with permission from Kumar and Ramamurty [168]. (Copyright (2020) Elsevier).

plement a scan strategy such that a layer is divided into smaller "islands" or "strips", so that the longest uninterrupted line of travel is reduced. PBF systems mostly deal with the stress build-up by rotating the scan direction of the heat-source after each layer [195]. The layer height has also been shown to directly affect the stress distribution; a finer layer results in higher stress gradients compared to a thicker layer [195]. Since the residual stress build-up is dependent on each layer, overall stress levels depend on the part size. For example, Edwards and Ramulu [181] have shown that the tensile residual stresses in taller and narrower LB-PBF Ti6Al4V specimens are higher and penetrate deeper (up to 250 μm deep) from the surface, whereas they are smaller and shallower (50 μm) in the larger parts.

The effect of high residual stresses poses a problem both during fabrication and in service. Small cracks, formed along the melt pool path, are often observed in hard metals such as Ni-based superalloys [204–206] and tungsten [206], see Fig. 10. More substantial delamination type defects that from between the layer interface [207] or near the stress concentration such as support structures [208] are also reported. The build-up of significant tensile stresses in larger parts has been reported to result in delamination at support structures or from the build platform during fabrication [16,198,207]. Dimensional tolerances are also significantly affected due to part distortion. Residual stresses can act as an additional crack driving force during fatigue, thereby promoting crack initiation and propagation.

4.4. Post-processing treatments to improve process-related attributes

After fabrication, several steps are required to turn the AM part into an end-use part. Typically, the excess powder is removed, the parts are cut from the build platform, and support structures are machined off. Additional post-process treatments may be employed to improve process-related attributes, including thermal treatments to improve the microstructure and/or mitigate residual stresses, hot isostatic pressing (HIP) to reduce porosity, and some form of the surface finishing process to achieve the desired surface finish and geometrical tolerance.

Heat treatment is commonly employed for AM Ti6Al4V, SS, Ni-based superalloys, and Al alloys. SR heat treatments involve recovery. LB-PBF and DED parts are typically stress relieved before they are cut from the build platform to limit deviations from geometrical tolerance requirements. A SR heat treatment is performed at temperatures high enough to allow for atomic mobility but short enough in time to suppress recrystallisation and grain growth. Higher temperature annealing typically result in grain growth, changes in grain orientations, and can promote the formation of a more equiaxed microstructure. This is typically accompanied by a reduction in strength, a concomitant increase in ductility and a decrease in anisotropy (which may be desirable, as AM metals often contain columnar, oriented microstructure, especially those fabricated using the PBF processes). Higher temperature heat treatments, however, do not improve density and the surface finish.
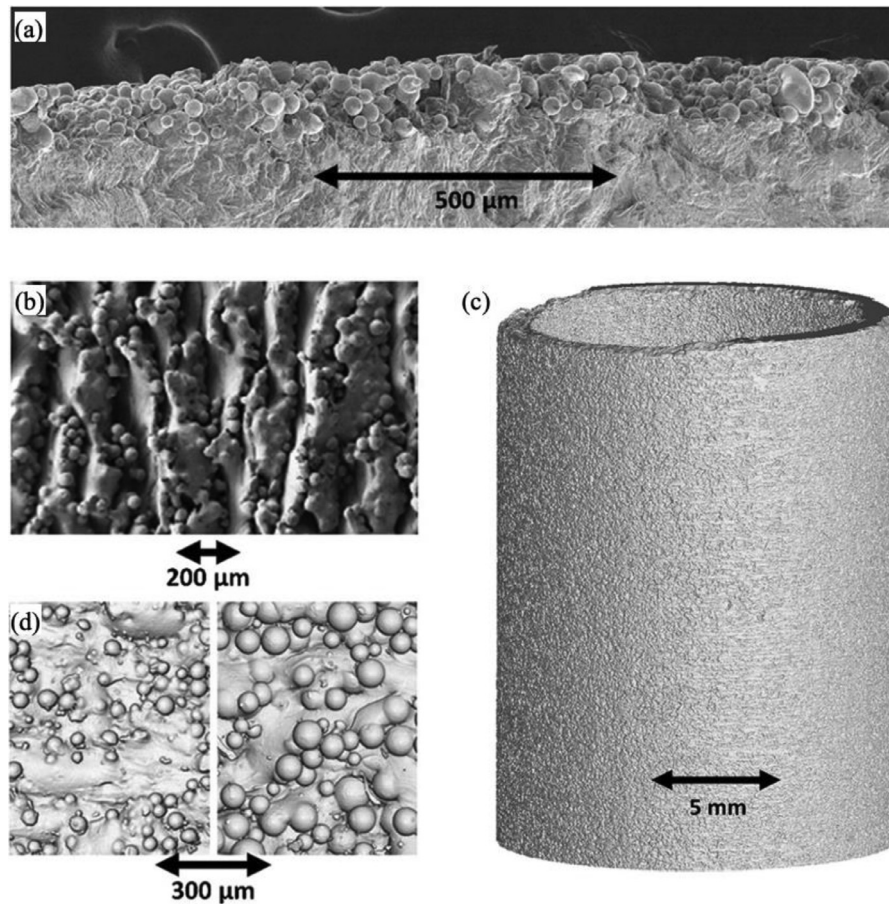
Fig. 9. (a) SEM image of LB-PBF Ti6Al4V. Reproduced with permission from Sanaei et al. [16]. (b) SEM image EB-PBF Ti6Al4V. Reproduced with permission from Karlsson et al. [190]. (c) Micro-CT scan of specimen shown in (a). (d) Synchrotron radiation micro-tomography with a resolution of 1.5 μm of LB-PBF Ti6Al4V. Reproduced with permission from Kantzos et al. [186]. Copyright (2013) Elsevier and (2018) Springer).
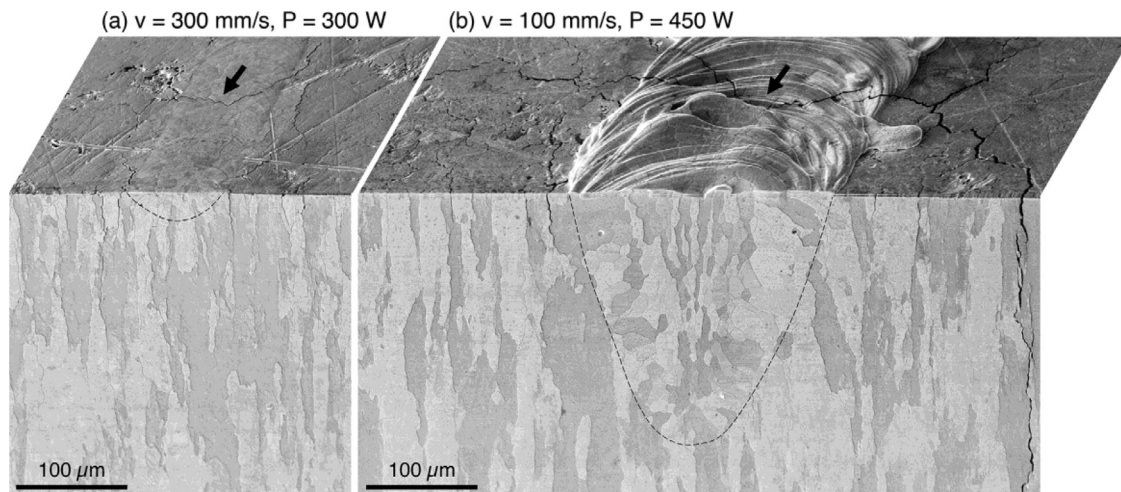

Fig. 10. Crack network in LB-PBF Tungsten. The figures show two laser exposure strategies resulting in varying melt pool sizes: shallow in (a) but deep in (b). The black arrows indicate transversal cracks. Reprinted with permission from Vrancken et al [206]. Copyright (2020) Elsevier.

HIP is a commonly recommended process for reducing porosity in parts fabricated using AM. For example, it has been shown to close internal flaws and cracks in LB-PBF Ni-based superalloy [209] and Ti6Al4V [173,210–212]. Additionally, it can eliminate the residual stresses [74]. If the gas containing flaws are not completely closed, subsequent heat treatments can reopen them [213,214]. A study of on LB-PBF Ti6Al4V [215] showed that while internal flaws were closed during HIP, surface and near-surface flaws remain un-

affected. In some instances, HIP may significantly alter the grain structure of the AM parts through significant grain growth [216].

The most common method to improve the surface finish of an AM part is machining using standard processes such as milling and turning. Due to the geometric complexity that AM allows for, CNC processes may often become necessary [2], mostly in conjunction with near-net shapes process such as DED [217]. However, the geometric freedom that AM offers necessitates undefined geometri-
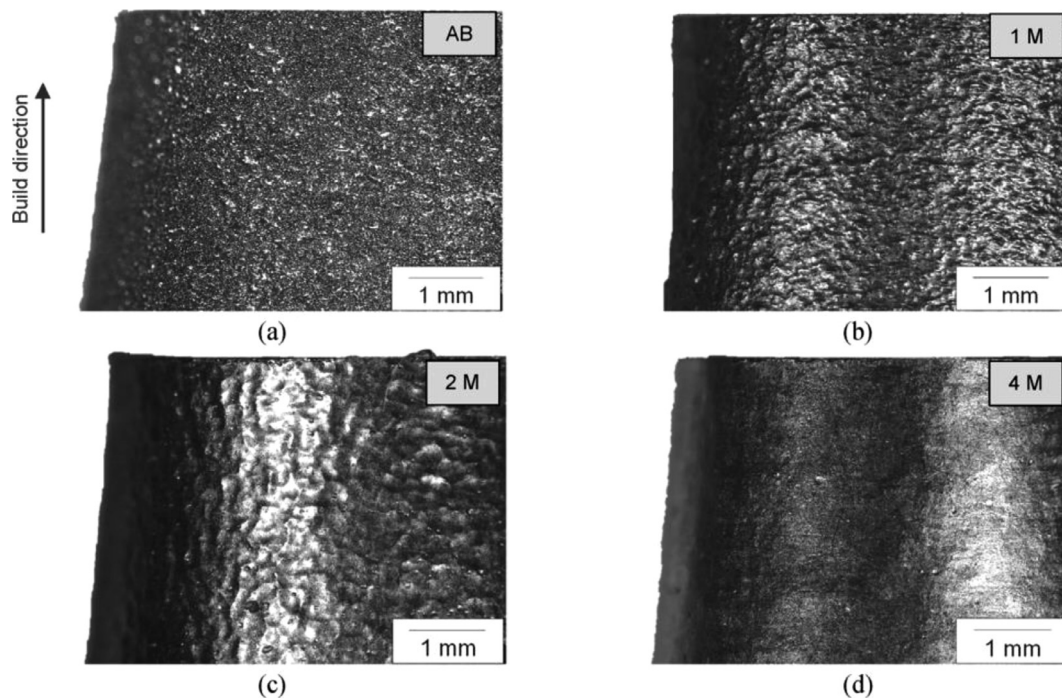
Fig. 11. Surface finish after chemical etching of LB-PBF Ti6Al4V for (a) AB surface (AB), and after chemical etching (b–d) for different molar (M) solution concentrations. Reprinted with permission from Bezuidenhout et al. [219]. (Copyright (2020) Elsevier).

cal process. Techniques that have been reported to help improve the surface finish include vibratory grinding [218], chemical polishing [219], electropolishing [220], surface mechanical attrition treatment (SMAT) [221], and ultrasonic nanocrystal surface modification (UNSF) [222], as well as simple rotary-tool polishing or grinding with a belt sander (for flat surfaces) [16]. Bezuidenhout et al. [219] showed that HF-HNO$_3$ could reduce the surface roughness of LB-PBF Ti6Al4V by up to 90%, as illustrated in Fig. 11. These processes can, however, be challenging to control and do not always meet the standards required for high-quality parts. Shot peening has also been recommended as a surface finishing technique. While it does not necessarily impart a significantly improved surface finish, the mechanical working of the material's surface induces compressive residual stresses that can significantly improve the fatigue life, for example, as shown by Kumar et al. [168] using LB-PBF Ti6Al4V.

5. Tensile properties

The quasi-static tensile properties of AM alloys are predominantly controlled by the microstructures in them, while porosity, surface roughness and residual stresses play a less significant role (unless their levels are far too large, or the tensile ductility is low). As outlined in Section 3, the microstructures of direct fabrication methods are fine with the presence of the solidification cellular structure; such refined (and sometimes metastable) microstructures are attributed for the high static strength and low ductility compared to their conventionally produced counterparts [80,81,85,122,223]. In a number of AM alloys, the yield strength (YS) was found to obey the Hall-Petch relationship, implying that the finer microstructural features are the cause for the observed high YS [224–226]. The properties of the alloys manufactured using BJP, on the other hand, are similar to their conventionally produced counterparts [40].

Tensile properties of AM alloys such as YS, ultimate tensile strength (UTS), and elongation at failure (EF) are often anisotropic with YS and UTS being superior in the build direction (Z).

Anisotropy in EF is often the most pronounced, with higher values in the orientations perpendicular to the build direction (X and Y). This behaviour is attributed to the pronounced mesostructure and in some cases crystallographic texture. In some instances, optimised process parameters can reduce anisotropy by imparting more equiaxed microstructures to the built parts, as discussed later.

In most instances, however, post-process heat treatments are required to improve quasi-static tensile properties. Such treatments often reduce the strength but increase ductility; the resulting strength-ductility combinations still meet standardised requirements in most instances, for example, in Ti6Al4V [15]. Heat treatments generally reduce anisotropy. However, some level of anisotropy often remains due to the inherent mesostructure in AM alloys. In the following, distinct features of the tensile properties of specific alloy systems produced using the AM techniques are summarised.

5.1. Titanium alloys

Table 1 gives an overview of selected tensile properties reported for AM Ti6Al4V. For comparison purposes, properties of the wrought Ti6Al4V are also listed. As seen from it, while the AM alloys can meet or even exceed YS and UTS of the ASTM specification (for example, surgical implants produced by cast [227] and wrought [228] routes), EF is often lower.

LB-PBF often yields an AB alloy with high YS and UTS of ∼ 1030 and ∼ 1200 MPa, respectively, and comparatively low EF between 7–10 %, which is due to the formation of martensite, α'. Xu et al. [224] reported that by careful adjustment of LB-PBF parameters such as layer thickness and volume energy, the temperature cycle during build-up might be controlled in a way that α' decomposes *in-situ*, leading to a more favourable high strength - high ductility combination. LB-DED alloys have lower YS and UTS (∼ 960 and ∼1100 MPa, respectively), with an improved EF that ranges between 10 and 18%, due to the lower cooling rates. The EB-PBF process results in an alloy with an even more reduced YS and UTS

(∼ 880 and ∼ 960 MPa, respectively), but with an improved EF that ranges between 9 and 16%, attributed to the use of a heated build platform in this process. (Far superior EF values of up to 25 % have been reported by Murr et al. [229]).

Compared to LB-PBF, the ductility of AB parts produced using LB-DED and EB-PBF processes is better due to a coarsened and lamella α structure (in a β matrix). This is a consequence of the *in situ* tempering caused by heating of the build platform in EB-PBF and a relativity slower cooling rate in LB-DED. However, ductility as low as 2.7% was reported by Choi et al. [230], which could be due to oxygen contamination [113] in LB-DED due to the difficulty in controlling the environmental conditions in that process. Oxygen pickup by titanium is known to be a significant factor in increasing its strength and reducing ductility [231,232]. Hence, such variations in the chemical composition, even if they are minor, may rationalize the observed variance in the reported properties. This is evident in the LB-PBF processes that employ build platform heating. For example, Vrancken et al. [202], noted a low EF (< 3.9%) when using build platform heating of up to 400 °C, and attributed the substantial reduction in the ductility to the oxygen pickup during processing.

Anisotropy in tensile properties is present (to varying degrees) in all the alloys processed using the AM techniques considered in this overview. The anisotropy is most notable in the EF. For example, lower EF is generally observed in the horizontal orientation (i.e., specimens loaded in either X or Y directions). This was attributed to the columnar PBG structure or elongated grain morphology in Ti6Al4V [233]. A suitable combination of powder layer thickness and hatch strategy can result in a more equiaxed PBG structure that, in turn, reduces the anisotropy and enhances the ductility. The failure mode of AB Ti6Al4V is mostly intergranular [3], with both brittle faceting and ductile tearing fracture modes (depending on the PBG orientation due to their columnar nature) being reported by Kumar et al. [97]. Recently, Ter Haar and Becker [113] argued that anisotropy in the LB-PBF alloy is due to the dominant α' microtexture. Their studies using EBSD and fractographic analyses revealed that α' laths shear preferentially along the maximum shear stress trajectories and plastic flow localises within PBGs. The dominant ∼ 45° habit planes within the columnar PBG structure thus control anisotropy, whereby PBGs in the ZX-plane have larger regions of microtexture promoting slip and hence ductility.

Heat treatment results in the transformation of fine α' or α into coarsened and lamellar α in a β matrix, to form an α + β structure similar to that obtained by the EB-PBF process or through conventional manufacturing routes. These microstructural changes lead to a reduction in YS (and UTS) and an improvement in EF. However, significant grain growth at high AN temperatures can reduce YS to 715 MPa, which is well below that of the wrought alloy [234]. Similar YS and UTS values between LB-PBF and EB-PBF are achievable after an appropriate heat treatment. However, ductility of LB-PBF Ti6Al4V is often lower than that of wrought and cast alloys. A bimodal microstructure consisting of equiaxed primary α phase and lamellar secondary α + β structure can be obtained in LB-PBF Ti6Al4V by using a duplex heat treatment; EF of this alloy is substantially enhanced to 16–20% [103].

5.2. Steels

The tensile properties for selected AM steels, along with the volume fractions of different microstructural phases in them, are listed in Table 2. In most cases, the properties often meet or exceed the specified values required for industrial applications in the AB state itself. For example, LB-PBF 316L achieves YS and UTS of ∼ 440 and ∼ 660 MPa, respectively, whereas the respective properties of wrought 316L are 170 and 485 MPa [235]. Similarly, YS

and UTS of LB-PBF 304L are∼ 450 and ∼ 670 MPa, respectively. The considerable increase in both YS and UTS of most AM steels is due to the fine solidification cell sizes in them. Importantly, these strength enhancements do not get offset by a marked reduction in EF, with reported values for LB-PBF 316L and 304L ranging between 35 and 60%. However, high porosity levels can lead to a significant reduction in EF (for example in BJP steels), whereby the failure shifts from ductile to brittle failure mode [226]. Kumar et al. [40] report that in BJP 316L the unique combination of planar slip, which prevails in the early stages of plastic deformation, and other microstructural factors leads to the arrest of small cracks that nucleate at the corners of the flaws and hence the ductility of the steel is *flaw-insensitive*. However, if the flaw size is significant enough, an order of magnitude reduction in EF is noted, as for example in LB-DED 316L [236]. Like titanium alloys, the reported strengths depend on the processing methods employed as well as the microstructure obtained. The slower cooling rates in EB-PBF, due to build platform heating, results in a comparatively lower YS and UTS of ∼ 360 and 570 MPa, respectively. Steels produced with BJP, on the other hand, work harden considerably after densification and ageing, with YS and UTS of ∼ 180 and ∼ 550 MPa, respectively, with an EF of ∼ 70%.

Precipitation hardened steels 17-4PH and 18Ni300 are relatively softer in the AB state as compared to their wrought counterparts, as the rapid solidification rates that prevail in most AM processes do not allow sufficient time for the precipitation to take place [237–239]. 18Ni300 produced by LB-PBF displays lower YS and UTS in the non-aged condition (∼ 950 and ∼ 1150 MPa, respectively) despite the finer microstructure in it. Retained austenite and austenite reversion have been observed to result in transformation induced plasticity, and consequently, exceptional work hardening. After AG (both with and without ST), a significant increase in UTS (to ∼ 2020 MPa) accompanied by a reduction in ductility is observed, as expected.

Anisotropy in tensile properties of AM steels is also commonly observed, attributed to the aforementioned columnar microstructure with a strong texture. This, however, can be overcome through an appropriate heat treatment. For example, a solutionising temperature of > 1050 °C is required for LB-PBF 316L for recrystallization to occur [93].

5.3. Ni-based superalloys

The tensile properties of AM Ni-based superalloys, summarised in Table 3, are highly sensitive to the thermal history experienced by the alloy during and after fabrication. As a result, the reported properties of alloys produced using different AM systems and heat treatment solutions range widely. This is due to the precipitation of γ' and γ" and needle-like δ along grain boundaries in some of them. More consistent properties are achieved after the appropriate ST + AG treatment is given. As previously highlighted, Inconel 718 requires slow heating and soaking at a temperature that is above 1050 °C, so as to enable the dissolution of the metastable Laves phase that forms during AM. This reduces the degree of Nb micro-segregation by back-diffusion from the solute-rich regions into the γ matrix. After ageing, the strength level of the AM alloy is similar to the wrought Inconel 718 [148,240,241]. UTS of ∼ 1150 and ∼ 1000 MPa with EF of ∼ 18 and ∼ 35 % in Inconel 718 and 625, respectively, can achieved. Typical of Ni-based superalloys, a strong correlation between the ageing time and strength exists.

Alloys produced with the direct AM techniques tend to have a fine dendritic microstructure in the AB state, due to the high cooling rates, and as a consequence, exhibit a strong texture that results in significant mechanical anisotropy [148]. However, a suitable combination of the process parameters can reduce anisotropy despite the directional solidification [241]. For example, equiaxed

microstructure with a near-isotropic tensile strength was obtained in Inconel 718 by using a point heat-source fill strategy (over a linear heat-source). However, anisotropy in EF remained [242].

5.4. Al alloys

A significant increase in the strength of Al alloys due to AM is commonly reported. For example, YS and UTS of $\sim$ 260 and $\sim$ 340 MPa are measured on LB-PBF AlSi10Mg. Such strength enhancements often come at the expense of EF, which vary between 1–8%. The improved strength is believed to be due to sub-grain boundaries and interdendritic Si that hinders the motion of dislocations [243]. Tensile properties of AlSi12 and AlSi10Mg are summarised in Table 4; typical properties of conventionally manufactured alloys are also listed for comparison.

The anisotropic microstructure and crystallographic texture that arise in LB-PBF AlSi10Mg, lead to anisotropy in mechanical behaviour. For example, the ductility of AlSi12 in the build direction is only half of that in the transverse orientation, even though differences in strength are insignificant [80,244–248]. Variations in the grain size, grain orientation, cellular morphology, and melt pool arrangement due to the variations in process parameters can result in strong anisotropy in both the UTS and EF. Paul et al. [155] reported that loading along the build direction shows more pronounced strain hardening resulting in premature failure along the melt pool boundaries at a tensile strain of only $\sim$ 3.5% as compared to 5–7% failure strains for the orientation loaded perpendicular to the build direction. Failure occurs along the melt pool boundaries when loaded in the build direction (Z), indicating a weakened interface at the melt pool mesostructure, where the cell structures are coarser and mostly elongated [10].

It was demonstrated that such anisotropy can be reduced by subsequent heat treatment. However, this generally comes with a significant loss in strength; for example, YS of LB-PBF AlSi12 reduced to 95 MPa upon annealing [80,244,249]. A standard T6 heat treatment has been shown to eliminate the Si network [157]. During subsequent ageing, the original fine grain structure coarsens and at the same time precipitates are formed. The former effect counteracts the intended strengthening by the latter, and thus results in the same YS as in the AB state [250].

6. Fracture toughness

Fracture toughness (K_{Ic}) of a material defines the resistance offered by it to cracking and is an essential property to ensure structural integrity and reliability. In AM, the combination of a metastable microstructure, mesostructure, porosity and high residual stresses can adversely affect the alloy's ability to resist fracture. Hence, heat treatment of the AB parts is often mandated to impart a fracture toughness that is similar to that of the conventionally produced alloy. This enables them to meet specified standards; for example, Ti6Al4V for biomedical applications [227,228].

Broadly, K_{Ic} depends on the following factors: the size of plastic zone ahead of the crack tip (r_p), crack tip blunting, and crack tortuosity or mixivity in the cracking mode. For example, a larger plastic zone size, often accompanied by crack tip blunting, induces substantial toughening. Similarly, crack mode mixivity can lead to substantial toughness enhancement due to shear-type (or mode II / III) fracture that promotes crack deflection (from mode I). While plastic zone formation and crack blunting are intrinsic mechanisms (that can lead to a conflict between strength and toughness; an increase in ductility leads to an improvement in K_{Ic}, but could come at the cost of YS and UTS), crack tortuosity is an extrinsic mechanism that can increase the toughness without affecting the strength [251]. Such extrinsic toughening mechanisms have been observed in AM alloys, where crack tortuosity

arises from the mesostructure described in Section 3.1. This can result in a substantial increase in both K_{Ic} and crack resistance ('R curve behaviour') of some AM alloys over their conventionally produced counterparts; examples are LB-PBF AlSi12 and AlSi10Mg reported by Suryawanshi et al. [252] and Paul et al. [155], respectably. As such, both the cellular and mesostructures considerably affect an AM alloys' fracture toughness and both need to be considered. While ductility increases fracture toughness, the unique mesostructure that can enhance strength and toughness properties by careful parameter selection.

Along with the alloy's microstructure, the roles of residual stresses and the size and distribution of defects need to be considered carefully when determining the fracture toughness of AM alloys. For example, Cain et al. has reported an inverse correlation between the residual stress and anisotropy in K_{Ic} of LB-PBF Ti6Al4V [253]. Similarly, Seifi et al. [173] reported a correlation between porosity and K_{Ic} for EB-PBF Ti6Al4V, as we will discuss below. Because of these factors, significant anisotropy (and heterogeneity in some cases) in K_{Ic} is observed for AM alloys [15]. While the process-specific attributes of residual stresses and defect distribution can be detrimental to K_{Ic}, the mesostructure can significantly improve them. In the following, we summarise fracture properties and features of the AM alloys specific to each family of alloys.

6.1. Titanium alloys

The typical K_{Ic} of wrought Ti6Al4V ranges from 30 to 100 MPa$\sqrt{m}$, depending on the materials microstructure [254]. In comparison, K_{Ic} of AB LB-PBF Ti6Al4V could be as low as 16 to 31 MPa$\sqrt{m}$, primarily because of the presence of defects and residual stresses [15]. After achieving densities above 99.5% and heat treatment, K_{Ic} improves between 48 to 67 MPa$\sqrt{m}$ [97,189]. These can be improved further; for example, Kumar et al. [98] and Dhansay [255] report K_{Ic} values ranging between 75 to 106 MPa$\sqrt{m}$ after duplex heat treatments.

The observed enhancement in fracture toughness upon heat treatment is due to the formation of lamella α–β microstructure, which is considerably more ductile. K_{Ic} is highest in $\alpha + \beta$ Ti alloys with lamellar microstructure [8]. Unlike rolled Ti6Al4V, where the crystallographic texture can induce anisotropy, the lack of a strong crystallographic texture in the AM alloy suggests that the columnar PBG structure is responsible for the anisotropy observed. The mesoscopic columnar PBG structure aids crack tortuosity, where the PBG boundaries act as weakened interfaces. Kumar et al. [98] conducted a detailed investigation into the link between microstructure and K_{Ic} in LB-PBF Ti6Al4V. Their results show that anisotropy is related to r_p, which is only $\sim$ 0.2 mm in the AB condition and increases by an order of magnitude to 2–3 mm after heat treatment. Since r_p in the AB condition is similar to the spacing between the PBGs ($\sim$ 0.14 mm), preferential crack growth along the boundary is possible only when a crack tip is close to a PBG boundary. A columnar to near-equiaxed PBG transition can be induced by altering the scan rotation from 90° to 67°, as illustrated in Fig. 3c and d. The specimens with equiaxed PBGs obtain a near isotropic K_{Ic} in the AB condition ($\sim$ 48–54 MPa$\sqrt{m}$) as well as after the AN treatment ($\sim$ 96–93 MPa$\sqrt{m}$) [97,98].

In the AB state, Ti6Al4V produced using EB-PBF generally exhibits higher K_{Ic} than its LB-PBF counterpart, predominantly because of the $\alpha + \beta$ lamellar microstructure in it. Seifi et al. [173] reported that K_{Ic} of AB EB-PBF Ti6Al4V ranges widely (between 43 and 95 MPa$\sqrt{m}$) and noted a significant narrowing in the range (to 61–3 MPa$\sqrt{m}$) after HIP. On this basis, the wide range of K_{Ic} in the AB state was ascribed to the combination of porosity and residual stresses since HIP reduces both. The reduction in the average K_{Ic} value after HIP is due to a twofold coarsening of

the α laths, which reduced the alloy's strength [15,173]. Seifi et al. also characterised the defects in EB-PBF Ti6Al4V and observed a correlation between defect size and the measured toughness; the variation in defect size was attributed to the material's heterogeneity that was dependent on the building height. Similar to Kumar et al.'s [98] findings, anisotropy exists (even after HIP) due to the columnar PBG structure that provides an easy fracture path [173].

6.2. Steels

Compared to conventionally produced 316L, whose K_{Ic} can range between 112 and 278 MPa$\sqrt{}$m, the AM alloy's K_{Ic} is lower. For example, K_{Ic} ranges between 63 and 87 MPa$\sqrt{}$m for LB-PBF 316L [256]. This is likely due to defects, reduced ductility, and the absence of transformation-induced plasticity (TRIP). The latter was illustrated by Kumar et al. [257] who observed a substantial reduction (by $\sim$ 40%) in fracture toughness and a concomitant enhancement in anisotropy (by $\sim$ 16 %) with a mere 50 °C increase in the test temperature (from room temperature at which TRIP gets activated to 75 °C where TRIP is no longer activable and the deformation mechanism is dominated by dislocation glide and twinning) in LB-PBF 304L [257,258].

Though a mesostructure in the form of melt-pool boundaries can be observed in most steels fabricated using different AM techniques, no elemental segregation to those boundaries or misorientation across them could be seen. Whether the grain growth occurs within or across the melt-pool depends on its geometry as well as the heat transfer mode (keyhole versus conduction modes), as illustrated in Fig. 4e–g. Crack tortuosity induced by the melt-pool structure is possible, due to the intrinsically intertwined nature of melt pool and grain structures and, can result in toughness anisotropy [259].

K_{Ic} of aged LB-PBF 18Ni300 (70-75 MPa$\sqrt{}$m) is similar to that of the conventional alloy [127]. Yadollahi et al. [138] estimate (from the FCG data) K_{Ic} of LB-PBF 17-4PH after ageing (H900 condition) to be $\sim$ 70 MPa$\sqrt{}$m, which is purportedly higher than a K_{Ic} of 50 MPa$\sqrt{}$m of CM PH-17-4 steel in H900 condition, this is likely due to the higher ductility of the AM alloy. The number of studies that investigate the fracture toughness of AM steels is rather small. Detailed studies on the influence of the AM specific features such as solidification cells, localised crystallographic texture, and mesostructures on fracture behaviour are yet to be performed.

6.3. Ni-based superalloys

Like that of steels, not much fracture toughness data of AM Ni-based superalloys is available. Results of the few studies suggest that the fracture toughness of AM Inconel alloys is strongly dependent on the microstructure and thus thermal history experienced, as with tensile properties. Puppala et al. [260] reported that fracture toughness of LB-DED Inconel 625, estimated using the crack-tip opening displacement (CTOD) technique, is close to that of its welded counterpart but inferior to that of the wrought counterpart. They suggested that porosity influences fracture toughness markedly as an increase in porosity (from 0.1 to 2.7%) resulted in a significant reduction in K_{Ic} (from 95 to 65 MPa$\sqrt{}$m), which was accompanied by a ductile to brittle fracture mode transition [261]. Michael et al. [262] report that K_{Ic} is location- and orientation-dependent in AB LB-PBF Inconel 718. This was attributed to the effective porosity that the propagating encounters; a lower porosity in the vertical specimen (Z) results in a K_{Ic} of 110 MPa$\sqrt{}$m, whereas it is 116 MPa$\sqrt{}$m in a horizontal specimen (X or Y orientations). HIP (at 980 °C) followed by SA and AG treatments reduce K_{Ic} to 82 MPa$\sqrt{}$m. This could be due to the strengthening of the alloy, and hence a reduction in ductility. Conversely, K_{Ic} in AB LB-DED Inconel 718 is 86 MPa$\sqrt{}$m and nearly-doubles to 164 MPa$\sqrt{}$m after

homogenisation (at 1100 °C) followed by ST and AG. (For comparison, K_{Ic} of the wrought alloy is 103 MPa$\sqrt{}$m) [153]. Here, the low K_{Ic} in AB conditions was attributed to the absence of γ''/γ' precipitates in the γ matrix whereas high toughness after ageing is imparted by the precipitation strengthening by γ'' and γ'. However, direct ageing treatment does not improve K_{IC} due to the presence of coarse Laves phases and heterogeneous γ''/γ' precipitates. Therefore, both high ST and AG treatments are required to achieve a K_{Ic} that is comparable to CM counterparts [153]. As previously discussed, dissolution of the Laves phases and homogeneous distribution of Nb can only be achieved by solutionising above 1050 °C, which also leads to an equiaxed grain structure and grain growth [151–153].

6.4. Al alloys

The presence of a contiguous network of inter-dendritic Si phase at the melt-pool boundaries in LB-PBF Al-Si alloys in the AB state provides an easy path for crack propagation and consequently promotes extensive crack deflection [155]. Hence, the mesostructures in these alloys exert a pronounced and often positive effect on the fracture toughness due to the mesostructure-induced crack tortuosity. In LB-PBF AlSi12, Suryawanshi et al. [252] reported that K_{Ic} values are 2–4 times higher than that of the cast alloy [252]. This toughness enhancement accrues despite the fact that the YS is also $\sim$ 2 times higher, i.e., AM imparts simultaneous enhancements in strength and toughness, which is in contrast to most conventional alloys wherein a strength enhancement often comes at the cost of toughness and vice versa. Suryawanshi et al. [252] attribute the significant improvement in strength to both the microstructural refinement and relatively higher Si in solid solution. The improvement in toughness is solely due to the mesostructure, which enhances the crack tortuosity through crack deflection at the melt pool boundaries [155]. Naturally, the mesostructure imparts toughness anisotropy, with the fracture toughness in the build direction (Z) being higher, as the crack plane normal is parallel to the build layers and crack propagation essentially occurs between the individual layers. Annealing reduces K_{Ic} of these alloys, although ductility is improved at the cost of strength. The decomposition of the melt pool boundary's structure, including Si precipitates, is believed to be the reason behind the lower resistance to crack propagation, i.e., lower K_{Ic}. Nevertheless, the toughness of the heat-treated material is still double that of the cast alloy.

Leonhard et al. [263] reported K_{Ic} values ranging between 40 to 60 MPa$\sqrt{}$m for LB-PBF AlSi10Mg. The K_{Ic} values, although significantly higher than values of cast Al-Si alloys, e.g., AlSi10Mg has a K_{Ic} of 11 to 20 MPa$\sqrt{}$m [264], may be somewhat elevated as a result of specimen size effects [252] and a lack of fatigue pre-cracking [263] before testing.

In a recent paper, Paul et al. [155] reported equivalent fracture toughness values ranging between 23 to 30 MPa$\sqrt{}$m for LB-PBF AlSi10Mg in its AB state, similar to K_{Ic} of 27 to 31 MPa$\sqrt{}$m reported by Liu et al. [265]. They noted that an increase in either the hatch spacing or layer thickness results in a larger columnar grain structure with a wider cellular sub-structure. In contrast, the scan strategy controls the melt pool arrangement, and the formation of a melt pool dominated mesostructure. K_{Ic} was found to be more sensitive to the scan strategy, whereas hatch spacing, and layer thickness exert a bigger impact on tensile properties (as discussed in Section 5.4). The alloy coupons built with a 90° scan strategy has reduced fracture toughness (19–27 MPa$\sqrt{}$m) compared to material built with a 67° scan strategy (25–31 MPa$\sqrt{}$m). This was attributed to the crack tortuosity; a less tortuous crack path is observed in specimens built with the 90° scan strategy that results in the formation of two distinct melt pool orientations, compared to a random melt pool arrangement in the 67° material [155]. Crack

propagation across the melt pool boundaries occurs through inter- and trans-granular failure; intergranular failure is more likely to occur along elongated grain boundaries where the crack passes the melt pool perpendicularly; transgranular failure is more likely to occur where the crack crosses the melt pool boundary at an angle. Moreover, crack deflection at the interface of the individual melt pools was observed in regions where crack deflection is energetically more favourable than crossing a melt pool. Paul et al. [155] suggest this indicates a difference in crack propagation resistance across the melt pool and along the melt pool boundary.

7. Fatigue crack growth characteristics

Understanding fatigue crack growth (FCG) characteristics is of particular importance in safety-critical applications. This allows for the use of damage tolerant design methodologies in structural integrity and reliability assessments, where load fluctuations are inevitable. Since several different types of defects are inherent to AM, notably porosity and a rough surface finish, both of which are highly detrimental to the fatigue behaviour of structural components, such understanding becomes critical for life prediction and hence part certification and widespread adaption of AM metals.

Three regimes categorise the FCG behaviour of metals: Initiation or near-threshold *regime I*, steady-state growth or Paris *regime II*, and fast fracture *regime III*. Regime III entails unstable, rapid crack growth that is sensitive to variations in microstructure and stress state and is directly related to the alloy's fracture toughness. It is important to note that the presence of the mesostructure is likely to make ductility and K_{Ic} of AM alloys uncorrelated, as previously discussed. This implies that structural integrity assessments require an in-depth understanding of fracture toughness properties related to the underlying micro- and meso-structures, i.e., process, orientation and heat treatment specific fracture toughness properties are required. Conversely, both residual stress and porosity do not adversely influence the fast fracture regime in a significant manner (unless their quantity is too large, which would make the printed part's suitability for application moot anyway) [211].

Regime II entails an incremental cycle-dependent advancement of the crack, visible through localised plastic deformation at the crack tip, and is less sensitive to variations in the microstructure, load ratio (R) and the part geometry. This is because the size of r_p is several times the characteristic microstructural length scale. In the near-threshold *regime I*, crack growth either initiates or diminishes and is dominated by shear mechanisms susceptible to the microstructure (as the size of r_p and microstructural scales are similar), R and the environment.

The FCG behaviour of AM alloys is investigated reasonably-widely. Results of these are summarised in Table 5–8 for Ti6Al4V, Steels, Ni superalloys and Al-Si alloys. Broadly, the FCG performance of AM alloys is comparable to that observed in respective cast or wrought counterparts. However, the fine AB microstructure inherent to many AM alloys has been linked to the lowered FCG threshold values ($\triangle K_{th}$). Conversely, roughness induced closure effects are correlated with the mesostructure, such as the columnar PBG structure in LB-PBF Ti6Al4V or melt pool structure in Al- alloys. This implies that at low R, extrinsic factors such as the interaction between asperities in the crack surface and other crack shielding mechanisms reduce the effective crack driving force and hence improve the near-threshold FCG behaviour. Generally, for $R > 0.5$ these effects are less prevalent, and an intrinsic threshold value is measured. The strong influence of the underlying microstructure in the near-threshold regime means that through heat treatment and subsequent grain growth, threshold values can be increased, and anisotropy reduced.

Keeping the above in view, we summarise the common features of the FCG behaviour with respect to the steady-state FCG charac-

teristics (regime II) as well as the near-threshold FCG characteristics (regime I) first. We then highlight the specific characteristics of the near-threshold behaviours of each alloy system. Fracture toughness (regime III) is already discussed in Chapter 6.

7.1. Steady-state FCG characteristics

Regime II of the fatigue crack growth behaviour in most metals and alloys is described using the widely employed Paris relationship, $da/dN = C\triangle K^m$, where da/dN is the crack length advancement per load cycle, $\triangle K$ is the cyclic stress intensity factor range, and m (FCG rate exponent) and C (FCG rate coefficient) are material-specific constants. It is understood that the steady state FCG behaviour of AM alloys that were heat treated is generally similar to their wrought or cast counterparts. This is expected as steady-state FCG rates are less sensitive to the microstructure; m is a global indicator that does not necessarily reflect information about local effects such as microstructural features. However, alloys in the AB state generally exhibit higher FCG rates, as for example in LB-PBF, EB-PBF, and LB-DED Ti6Al4V [97,181,266], mostly due to a shift in C to higher values. This is in-part due to the presence of high and nonuniform residual stresses; tensile residual stresses provide an addition crack driving force causing a shift to a higher R, i.e., a shift in the mean applied stress while the cyclic applied stress remains constant [181,211,267]. The study by Becker et al. [197] on LB-PBF Ti6Al4V showed that at a low R (< 0.3), high residual stresses resulted in a highly variable crack growth behaviour, which was not apparent at higher R. This implies that at a low R, the influence of residual stresses is significant enough to influence the crack driving forces and thus the FCG behaviour. Similarly, Cain et al. [268] reported that FGC rates correlate with the residual stress levels; a faster FCG was observed at higher stress levels. This may result in anisotropic behaviour (Section 4.3). Since the residual stresses are known to be printing machine, scanning strategy, part size and orientation specific, the FCG behaviour of AM alloys in the AB state may well differ on different machines and setup, as is evident from the data provided in Tables 5–8.

FCG behaviour of AM Ti6Al4V has been most extensively studied. The FCG behaviour is similar between HIP, AN and DA states. In most cases, a m value of ~ 3.5 is reported after heat treatment, which is similar to that of the wrought material [254,269]. In the AB state, a relativity lower $m \sim 2.7$ is reported and is attributed to the presence of the fine α' in it (in contrast to a $\alpha + \beta$ structure in the heat treaded condition). In the relatively-brittle α' phase, fatigue cracks propagate predominantly trans-granularly – between parallel alpha laths – with potential for deflection at primary α' lath boundaries, resulting in decreased FCG rates [270]. Leuders et al. [211] show that flaws have little influence on the crack propagation behaviour in LB-PBF Ti6Al4V that has relatively low levels of porosity, as localised stress concentration associated with the flaws does not provide any significant additional crack driving force. This is in agreement with the observations of Poulin et al. [261], who investigated FCG behaviour of Inconel 625 with varying levels (0.1, 0.3 and 2.1%) of porosity. While the FCG behaviour is affected only marginally by the porosity level, it affects the fracture toughness significantly, as previously discussed.

While the overall FCG behaviour of AM steels, including 316L and 18Ni300 grades, is similar to their wrought counterparts (with m of ~ 3.9, and 2.5, respectively), it could be orientation-dependent, as reported by Riemer et al. [271] for LB-PBF 316L in AB and SR conditions . This behaviour was attributed to the presence of columnar cells in the microstructure, which enhances the crack path tortuosity, when the crack front is parallel to the columnar structure and, in turn, lowers the FCG rates. This anisotropy is less apparent after HIP that results in a more equiaxed microstructure. This suggests that more optimised process parameters, as re-

Table 5

FCG behaviour of Ti6Al4V, generated by different AM processes and heat treatment conditions.

Process	Source	Condition	R	Orientation	ΔKth[MPa√m]	m	KIc[MPa√m]
Wrought	[254,269]		0.1		4-5	3-4.8	65 ± 35
LB-PBF	[234]	AB	0.1	Z-X	1.52	-	-
				X-Z	1.82		
		HIP (820 °C for 3 h, FC at 3 °C/min)	0.1	Z-X	3.3		
				X-Z	3.46		
		HIP (950 °C for 3 h, FC at 3 °C/min)	0.1	Z-X	4.13		
				X-Z	4.53		
		BA (1020 °C for 1 h, AC)	0.1	Z-X	6.22		
				X-Z	7.29		
	[267,270]	AB	0.1	X-Y	2.7	2.77*	-
			0.3	Z-X	2.0		
				X-Y	2.1		
			0.45	X-Z	1.7		
			0.6	Z-X	1.9		
				X-Z	1.6		
				X-Y	1.7		
			0.77	X-Z	1.5		
			0.8	X-Y	1.6		
			0.84	X-Z	1.5		
			0.85	X-Y	1.5		
			0.88	Z-X	1.8		
			0.92	Z-X	1.8		
		SR (480 °C for 8 h, FC)	0.1	Z-X	2.7	2.77*	-
				X-Z	2.1		
				X-Y	3.1		
			0.3	Z-X	2.2		
				X-Z	2.0		
				X-Y	2.7		
			0.6	Z-X	2.0		
				X-Z	1.8		
				X-Y	2.0		
			0.75	Z-X	1.9		
			0.85	X-Y	1.6		
			0.86	X-Z	1.5		
			0.88	Z-X	1.9		
	[270]	AN (910 °C for 8 h, WQ) + AN (750 °C for 8 h, FC)	0.1	Z-X	5.6	3.51*	-
				X-Z	6.0		
				X-Y	6.2		
			0.3	Z-X	4.5		
				X-Z	4.9		
				X-Y	5.3		
			0.6	Z-X	3.1		
				X-Z	3.7		
				X-Y	4.1		
			0.77	X-Y	4.3		
			0.82	Z-X	2.7		
			0.88	X-Z	3.3		
			0.90	X-Z	2.8		
			0.91	X-Y	3.7		
	[97]	SR (650 °C for 3 h)	0.1	Z-X	5.7 ± 0.1	3.53 ± 0.02	52
				X-Z	5.75 ± 0.05	3.28 ± 0.2	55
	[97,348]	SR (650 °C for 3 h)	0.1	Z-X	4.12	-	-
				X-Z	3.07		
	[348,349]	SR + HIP	0.1	X-Y	3.74 ± 1.1	-	-
	[350]	AN (720 °C for 2 h, FC)	0.1	Z-X	3.2	-	49.5 ± 1.5*
		HIP (920 °C for 2 h at 105 MPa, FC)			4.4		-
		AN (720 °C for 2 h, FC)	0.7	Z-X	2.0		-
	[268]	AB	0.1	X-Y	-	3.37	28 ± 2
				X-Z		3.83	23 ± 1
				Z-X		5.84	16 ± 1
		SR (650 °C for 4 h, FC)	0.1	X-Y		4.17	28 ± 2
				X-Z		3.11	30 ± 1
				Z-X		3.24	31 ± 2
		RA (890 °C for 2 h, FC)	0.1	X-Y		4.41	40 ± 1
				X-Z		2.94	49 ± 2
				Z-X		3.35	49 ± 1
	[189]	AB	0.1	X-Y	6.3	2.61 ± 0.25	66.9 ± 2.6
				X-Z	5.8	2.36 ± 0.27	64.8 ± 17 7
				Z-X	5.9	2.45 ± 0.64	41.8 ± 1.7
	[255]	DA (950 °C for 1 h, AC) + AN (700 °C for 2 h, AC)	-	X-Y	-	-	75 ± 1
				X-Z			75.7 ± 0.4
				Z-X			79.6 ± 1.1

Table 5 (*continued*)

Process	Source	Condition	R	Orientation	ΔKth[MPa√m]	m	KIc[MPa√m]
	[351]	AB	-	X-Y	-	-	37
		AN (950 °C for 2 h, FC)		X-Y			86
		HIP (915 °C for 2 h at 105 MPa, FC at 11 °C/min)		X-Y			58
	[352]	SR (650 °C, FC)	0.1	Z-X	3.9	-	-
	[211]	AB	0.1	Z-X	1.4 ± 0.1	-	-
				X-Z	1.75 ± 0.15		
		RA (800 °C for 2 h, FC)		Z-X	3.7		
				X-Z	4.15 ± 0.45		
		BA (1050 °C for 2 h, FC)		Z-X	3.7 ± 0.6		
				X-Z	5.35 ± 0.75		
		HIP (920 °C for 2 h, FC)		Z-X	4.2		
				X-Z	6.1		
	[353]	AB	-	X-Y	-	-	52.4 ± 3.5
EB-PBF	[354]	AB	0.1	Z-X	3.7	-	56.6*
			0.5	Z-X	2.7		
			0.8	Z-X	2.2		
			0.1	X-Z	4.2		49.8*
			0.5	X-Z	3.0		
			0.8	X-Z	2.9		
		BA (1100 °C for 0.5 h, FC)	0.1	Z-X	6.0	-	-
			0.5	Z-X	4.8		
			0.8	Z-X	4.5		
			0.1	X-Z	6.0	-	82*
			0.8	X-Z	4.6		
	[355]	AB	0.1	X-Z	5.4 ± 0.3	-	82.6 ± 7.5
				X-Y	3.8		88
			0.3	Z-X	3.8		69
				X-Z	4.25 ± 0.65		79 ± 8
				X-Y	3.85 ± 0.05		89.5 ± 6.5
			0.7	X-Z	3.6 ± 0.1		70 ± 7
				X-Y	3.4		78
	[266]	AB	0.1	Z-X	3.75	-	-
				X-Z	4.31		
		AN (950 °C for 1 h, WQ) + SR (500 °C for 7 h, AC)	0.1	Z-X	3.95	-	-
				X-Z	5.5		
	[173]	AB	0.1	X-Z	3.8 ± 0.3	-	74.5 ± 21
				X-Y	2.9		91
			0.3	Z-X	4.4 ± 0.4		82.5 ± 9.5
				X-Y	4.2 ± 0.8		90.5 ± 2.5
			0.7	X-Z	3.6 ± 0.1		70 ± 7
				X-Y	3.4		78
		HIP (950 °C for 3 h at 100MPa, FC)	0.3	Z-X	4.05 ± 0.65		81.5 ± 16
				X-Y	4.9 ± 0.1		71.5 ± 12
	[350]	AN (720 °C for 2 h, FC)	0.1	Z-X	4.2	-	49.5 ± 1.5*
		HIP (920 °C for 2 h at 105 MPa, FC)			4.8		-
		AN (720 °C for 2 h, FC)	0.7	Z-X	2.9		-
LB-DED	[348]	AN (704 °C for 2 h, FC to 538C, AC)	0.0	Z-X	3.11	-	-
				X-Z	8.59		
	[266]	AB, low power laser	0.1	Z-X	2.88	-	-
				X-Z	2.97		
		AB, high power laser		Z-X	3.74		
				X-Z	3.72		
		AN (950 °C for 1 h, WQ) + AN (500 °C for 7 h, AC), low power laser		Z-X	3.14		
				X-Z	3.34		
		AN (950 °C for 1 h, WQ) + AN (500 °C for 7 h, AC), high power laser		Z-X	3.5		
				X-Z	4.05		

Z-X Crack opening in Z, crack direction in X or Y.
X-Y Crack opening in X, crack direction in Y (or vice versa).
X-Z Crack opening in X or Y, crack direction in Z.
 * Reported independent of *R*.

ported by Olivier et al. [92], can reduce the anisotropy in the FCG behaviour.

Similarly, the columnar cellular structure can lead to weakened interfaces as, for example, highlighted in LB-PBF 17-4 PH in the precipitation-hardened state [272]. When the notch is perpendicular to the build direction (Fig. 12), the crack initially propagates in mode I and then turns into mode II. This behaviour indicates the crack's tendency to propagate along the columnar grain boundaries. The presence of δ-ferrite along the elongated grain boundaries, forming a weakened interface, is argued to be the primary reason for the observed deviation in the crack path.

The significant role that the mesostructure plays on the FCG behaviour of AM alloys is most apparent in Al-Si alloys whose melt pool boundaries are characterised by the transition from fine to coarse cellular-dendritic microstructural features [80]. Moreover, directional solidification within each melt pool results in a cellular solidification structure with the ⟨ 100 ⟩ texture; the most favourable growth direction in the cubic materials [273]. The mesostructures, whose boundaries are decorated with a dense array of Si particles that are brittle, lead to the formation of cracks along the laser tracks [188]. Consequently, the relative orientation of crack propagation with respect to that of the laser track

Table 6
FCG behaviour of several stainless-steel grades, generated by different AM processes and heat treatment conditions.

Alloy	Process	Source	Condition	R	Orientation	ΔK_{th}[MPa$\sqrt{}$m]	m	K_{Ic}[MPa$\sqrt{}$m]
316L	Wrought	[256]	-	-	-	12.5 ± 0.25	2.5 ± 0.3	195 ± 83
	LB-PBF	[81]	AB (single melt strategy)	0.1	Z-X	9.9	4.0	72.3
			AB (single melt strategy)	0.1	X-Z	9.1	4.1	62.9
			AB (checkerboard strategy)	0.1	Z-X	8.1	3.7	86.8
			AB (checkerboard strategy)	0.1	X-Z	7.8	3.8	79.6
		[271,348]	AB	-1	Z-X	2.59	-	-
			AB	-1	X-Z	3.92		
			HIP	-1	Z-X	3.57		
			HIP	-1	X-Z	3.88		
18Ni300	Wrought	[127]	-	-	-	5.6 ± 0.1	2.5	77.5 ± 7.5
	LB-PBF	[356]	AB	0.05	-	2.9	-	-
			AN (635 °C for 6 h, FC to 360 °C, AC)	0.05	-	3.8		
		[127]	AB	0.1	Z-X	5.6	2.5	75.6
			AG (480 °C for 5 h, AC)	0.1	X-Z	5.8	2.5	70.2
17-4 PH	Wrought	[357]		0.1			3.4 ± 0.7	50-120
	LB-PBF	[138]	AB	0.1	Z-X	5.5 ± 0.5	-	70*
					X-Z	2.68 ± 4.3		
				0.4	Z-X	5.5 ± 0.5		
				0.7	Z-X	3.35 ± 0.65		
			ST (1040 °C for 0.5 h, AC)	0.1	Z-X	5.25 ± 0.25	-	-
				0.7	Z-X	3.6 ± 0.6		

Table 7
FCG behaviour of Inconel 625 and Inconel718, generated by different AM processes and heat treatment conditions.

Alloy	Process	Source	Condition	R	Orientation	ΔK_{th}[MPa$\sqrt{}$m]	m	K_{Ic}[MPa$\sqrt{}$m]
Inconel 625	LB-PBF	[358]	ST (1100 °C for 1 h)	0.1	Z-X	9.3	4.22	-
					X-Z	8.2	4.39	
				0.5	Z-X	6.9	3.99	
					X-Z	5.4	3.68	
				0.7	Z-X	5.35	3.80	
		[261]	SR (870 °C for 1 h, FC), 0.1 % porosity	0.1	X-Z	7.5	3.07	94.8
					Z-X	7.1	2.91	96.4
			…, 0.3 % porosity		X-Z	7.0	3.11	88.7
					Z-X	7.1	3.15	82.5
			…, 0.9 % porosity		X-Z	6.8	3.07	82.0
					Z-X	7.2	3.53	76.7
			…, 2.1 % porosity		X-Z	7.3	3.21	78.1
					Z-X	7.5	3.67	65.5
Inconel 718	Wrought	[269]		0.1		8.3 ± 1.8		
	LB-PBF	[281]	AB	0.1	X-Z	1.5	-	-
	LB-DED	[359]	AB	0.1	Z-X	3.0	2.22	-
			AG (720 °C for 8 h, FC; 620C for 8 h, AC)	0.1	Z-X	3.5	3.42	
			ST (980 °C for 1 h, WQ) + AG (720 °C for 8 h, FC; 620 °C for 8 h, AC)	0.1		5.0	4.76	
			HSAT (1100 °C for 1.5 h, WQ) + SA (980 °C for 1 h, WQ) + AG (720 °C for 8 h, FC; 620 °C for 8 h, AC)	0.1	Z-X	10.8	4.97	

Z-X Crack opening in Z, crack direction in X or Y.
X-Z Crack opening in X or Y, crack direction in Z.

is an important factor that determines the FCG rates, leading to orientation-specific crack path profiles, as illustrated in Fig. 13. Similarly, the columnar PBG structure in LB-PBF Ti6Al4V, has been linked to orientation dependent FCG behaviour. In an AB state the PBG imparts varying levels of crack tortuosity, which effects the crack closure, as we will later discuss.

7.2. Near-threshold FCG characteristics

The near-threshold FCG behaviour, which is highly sensitive to the microstructure of the alloy, depends on the loading conditions due to crack closure mechanisms associated with crack geometry (crack deflection or branching), crack tip shielding (phase transformation, plasticity or residual stresses) and environmentally induced effects [274]. The interaction between crack closure and FCG pivots on the contacting crack faces absorbing a portion of the load during each loading cycle; therefore, locally decreasing the driving force [275].

The threshold behaviour of AM alloys is reported in several papers, as summarised in Tables 5–8. The fine microstructure inherent to many of the AM processes (especially in the AB state) results in a relatively low FCG threshold value as compared to those of the wrought or cast counterparts in which the microstructure is relatively coarser. Notably, roughness induced closure effects are linked to the mesostructure common in AM produced metals, such as for example in Ti6Al4V due to the columnar PBG structure [197] or melt pool structure in AlSi10Mg and Al12Si alloys [188]. The strong influence of the underlying microstructure means that

Table 8
FCG behaviour of AlSi12 and AlSi10Mg, produced using different AM processes and heat treatment conditions.

Alloy	Process	Source	Condition	R	Orientation	ΔK_{th}[MPa$\sqrt{}$m]	m	K_{Ic}[MPa$\sqrt{}$m]
AlSi10Mg	Cast	[127,264]		0.1		3 ± 1	5.4	15 ± 5
	LB-PBF	[188]	AB	0	X-Z	1.30 ± 0.05	-	-
				0.7	Z-X	1.2 ± 0.05		
					X-Z	1.03		
				-1	X-Z	3.20		
		[360]	AG (300 °C for 2 h, FC)		X-Y	-	-	27.7 ± 4
		[361]	AB	-1	Z-X	-	-	37.4
			AG (300 °C for 2 h)					30.4
			AG (300 °C for 2 h) + HIP (250 °C for 2 h at 180MPa)					27.3
AlSi12	Cast	[80]		0.1		3.4	5.4	11.1
	LB-PBF	[33]	AG (240 °C for 2 h)	-1	Z-X	3.2	-	-
			AG ((240 °C for 2 h) (build platform heating)			3.5		
		[80]	AB	0.1	Z-X	1.4	3.7	37.9
					X-Z	1.1	3.1	46.7
			AG (300 °C for 6 h)		Z-X	3.1	3.7	19.3
					X-Z	2.0	3.1	21.7
		[155]	AB (90° layer rotation)		X-Z	-	-	23.8 ± 1.1
					Z-X	-	-	19.4 ± 1.8
			AB (67° layer rotation)		X-Z	-	-	30.4 ± 0.1
					Z-X	-	-	24.9 ± 0.4

Z-X Crack opening in Z, crack direction in X or Y.
X-Z Crack opening in X or Y, crack direction in Z.
*Reported independent of R
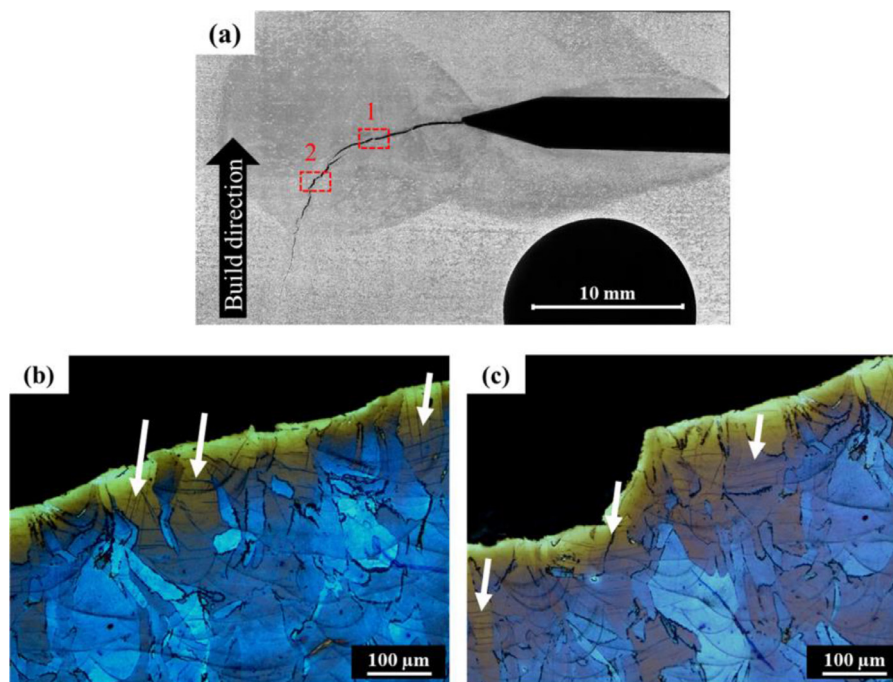
Fig. 12. (a) Crack path in 17-4PH steel having undergone a precipitation hardening heat treatment. Locations 1 and 2 show (b) microstructure at 1, and (c) microstructure at 2. Arrows indicate shear bands that are attributed to δ-ferrite, which accelerates crack growth due to the weak interface of δ-ferrite and martensite as well as low plasticity and brittleness behaviour of δ-ferrite. Reprinted with permission from Nezhadfar et al. [272]. Copyright (2019) Elsevier.

through heat treatment and subsequent grain growth, the threshold behaviour and anisotropy in it can be improved. This is particularly relevant, as most of FCG and hence part life, is spent in regime I. Improvements in near-threshold behaviour directly impact the material's sensitivity to flaws and surface roughness and therefore the fatigue life.

The orientation-specific nature of the mesostructures inherent in AM alloys means significant anisotropy in the regime I as well, both in terms of the measured ΔK_{th} and closure behaviour. Thus, unlike tensile properties, near-threshold FCG behaviour of AM al-

loys is often orientation dependent. While commonly reported only in Z and X or Y directions, the mesostructure of the material ideally necessitates investigations into the two crack planes, i.e., normal to the XY- and XZ- or YZ-planes, and the two crack propagation directions, i.e., in the Z and X or Y directions, resulting in three unique orientations, namely Z-X, X-Y and X-Z, where the first letter represents the direction normal to crack plane and the second letter represents the crack propagation direction. While eight different variations are possible [276], as is with extruded or rolled materials, the commonly employed layer rotation of the line-by-
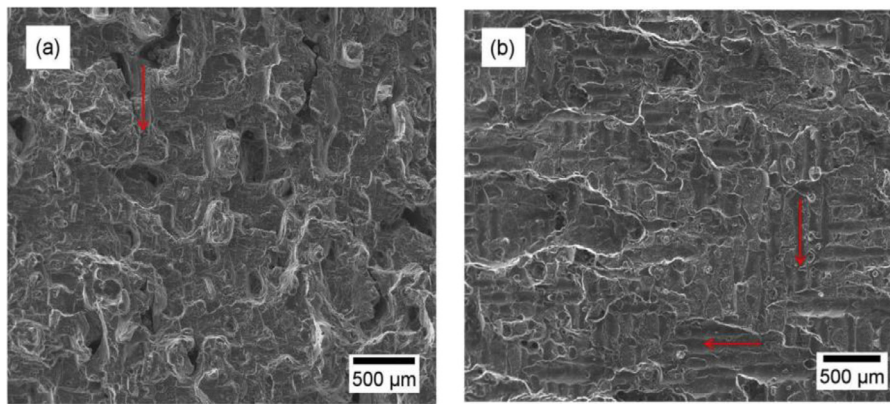
Fig. 13. Scanning electron micrographs showing fracture surface along laser tracks in LB-PBF AlSi12 in the (a) Z-X and (b) X-Z direction. Reprinted with permission from Suryawanshi et al. [80]. Copyright (2016) Elsevier.

line build strategy creates a *likeness* in X and Y, resulting in only three unique crack plane and growth direction combinations.

7.2.1. Ti alloys

In the AB condition, the LB-PBF Ti6Al4V has a relatively low ΔK_{th} (1.5–1.8 MPa$\sqrt{}$m for $R > 0.5$) that is similar to the welded material. This was attributed to the fine, needle-like α' microstructure [267]. In contrast, ΔK_{th} values measured on the EB-PBF alloy are significantly higher, ranging between 2.7 to 3.4 MPa$\sqrt{}$m for $R > 0.5$. This is because the EB-PBF alloy has an $\alpha + \beta$ microstructure with a bigger lath size in the AB state itself, due to significantly slower cooling rate inherent to this process. After heat treatment, ΔK_{th} of both EB-PBF and LB-PBF alloys increase substantially to between 3.1 to 4.6 MPa$\sqrt{}$m at $R > 0.5$. Zhai et al. [266] reported ΔK_{th} for heat treated EB-PBF and LB-DED materials, that are similar to the wrought material (3–4 MPa$\sqrt{}$m).

Anisotropy in the near-threshold FCG behaviour is most apparent in the alloys that are in the AB state. For understanding this, both ΔK_{th} and closure effects need to be considered. Becker at al. [267] suggest that the anisotropy is due to the morphological texture; the primary α laths orientated at $\sim 45°$, , act as barriers to crack growth, resulting in crack deflection and branching at their boundaries. This leads to a different ratio of transgranular vs. intergranular fracture facets in the Z-X orientation as compared to that obtained on the X-Z and X-Y planes. The required crack driving force will, therefore, differ between the crack planes. This is in agreement with the observations of Xu et al. [277], who compared the fracture morphologies in the X-Z and Z-X orientations. Similarly, Kumar et al. [168] showed that the PBG structure exerts a direct influence on the FCG behaviour in the near-threshold regime in LB-PBF Ti6Al4V; crack deflection is observed along lath boundaries and through the β phase along grain boundary α (after heat treatment). Such deflections reduce the mode I crack driving force significantly, which may lead to the arrest of the crack from propagating altogether. This is particularly evident when comparing the cracking orientation relative to the columnar PBG structure, as shown in Fig. 14. In some instances, a preferential crack path along PBG boundaries is visible, that is perpendicular to the crack plane, causing a mixivity in the fracture mode, whereby shear-type cracking (mode II / III) occurs over that of the opening mode (mode I).

The level of crack deflection is also orientation-specific, mostly due to the influence of the primary lath morphology that is dependent on the PBG structure. Cracks propagating in the Z-X and X-Z orientations encounter an equiaxed PBG structure ahead of them, whereas cracks with the X-Y orientation experience an elongated one. The net effect will be varying levels of asperities in the crack wake, leading to differences in the roughness induced closure effects. Macallister et al. [270] show that a DA heat treatment, which results in a bimodal microstructure, removes this mesostructural effect, confirming that crack closure is driven by the PBG structure. As such, the columnar PBG structure is considered a major drawback as it results in anisotropy in terms of crack growth kinetics.

7.2.2. Steels

The FCG behaviour of AM steels, including 316L, 17-4 PH and 18Ni300 steels, has been investigated. Riemer et al. [271] reported orientation-dependent ΔK_{th} in AB and SR conditions for LB-PBF 316L and reported a marginally lower threshold value (9.1 MPa$\sqrt{}$m) in the X-Z orientation as compared to that in the Z-X orientation (9.9 MPa$\sqrt{}$m). This difference is attributed to the tortuosity that crack experiences; crack propagation along columnar grains (X-Z) results in a smooth, less tortuous crack path whereas, crack growth in the Z-X orientation leads to a more tortuous crack path, resulting in fracture mode mixivity and consequently lowered ΔK_{th}. An equiaxed grain structure obtained through HIP results in isotropic crack growth properties that are comparable to those of the wrought 316L.

Unlike LB-PBF 316L, 18Ni300 does not seem to exhibit any pronounced anisotropy. A m of 2.5 and ΔK_{th} of ~ 5.7 MPa$\sqrt{}$m at $R = 0.1$ is reported, which are similar to those obtained on the wrought counterparts (2.5 and 5.6–5.8 MPa$\sqrt{}$m, respectively). Suryawanshi et al. [127] attributed the lack of anisotropy they observed in LB-PBF 18Ni300 to the absence of pronounced crystallographic texture and the negligible role of the mesostructure on strength. Notably, the scale of crack tortuosity is considerably small; crack deflections are similar in length scale to the solidification cell sizes of about 0.5 µm in the X-Z orientation. Since such deflections do not retard crack growth, roughness induced crack closure would not play any significant role in determining ΔK_{th}. However, near-threshold behaviour for $R > 0.5$ has not been extensively studied in AM maraging steels. It is likely that the preferentially orientated cellular structure and mesostructure may lead to differences in closure effects [138].

BJP 316L presents with an improved near-threshold FCG performance compared to the LB-PBF material [40]. This is because the microstructural features resulting from BJP process contain an abundance of effective barriers for FCG in regime I, such as the annealing twin boundaries with a misorientation of 60°, δ-ferrite phases, and large angle grain boundaries. Conversely, in the LB-PBF material, plastic deformation is readily aided through dislocation cross-slip because of the presence of fine solidification cellular structure. Moreover, since the misorientation in 50% of columnar grain boundaries is $< 5°$, LB-PBF microstructures are less effective

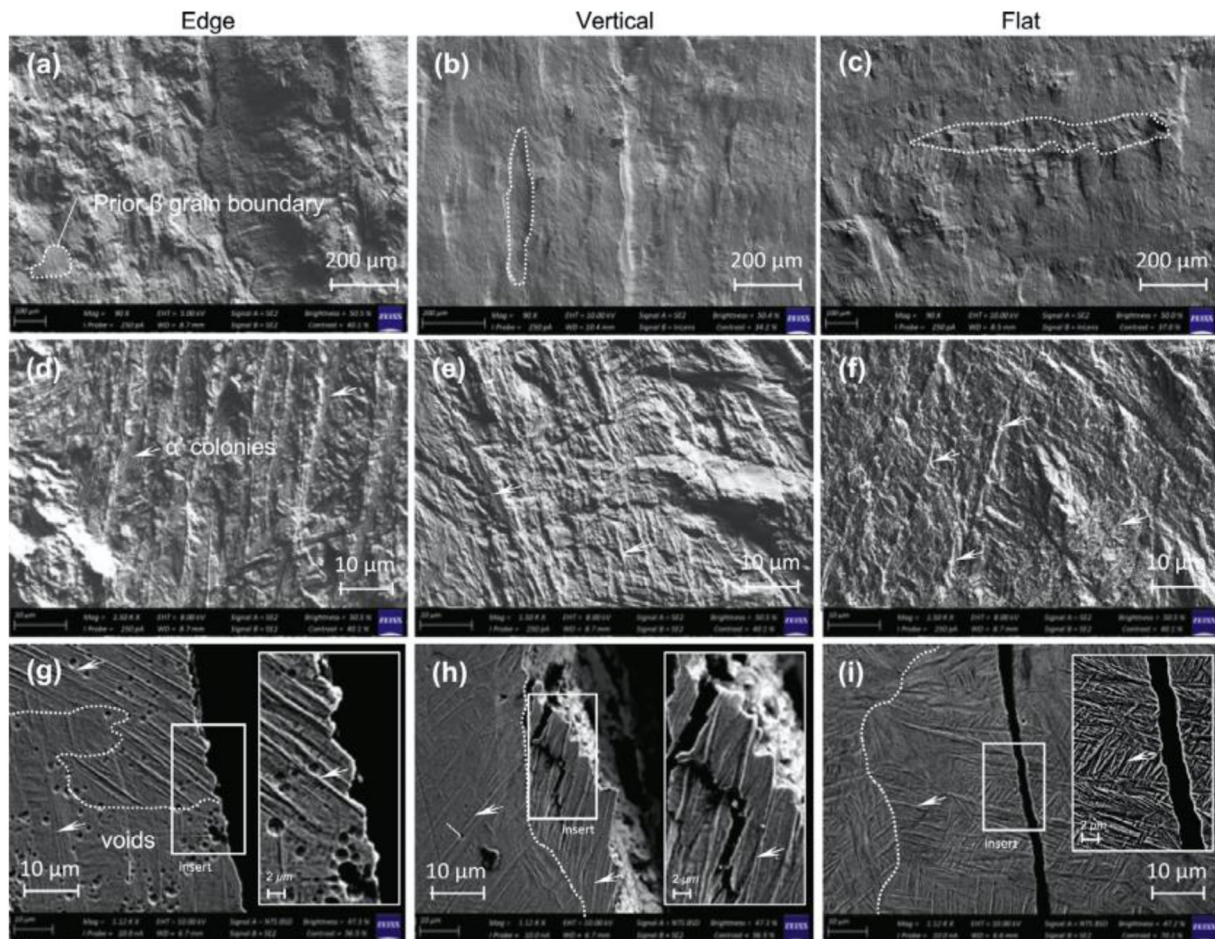**Fig. 14.** Crack profile in the Z–X (Edge), X–Z (Vertical) and X–Y (Flat) orientations of LB-PBF Ti6Al4V. All micrographs are in the AB state and were taken at locations in the near-threshold regime ($<$ da/dN = 10^{-9} m/cycle). Reprinted with permission from Becker at al. [267]. Copyright (2020) Elsevier.

in arresting the growth of the fatigue cracks. This, in conjunction with a relatively smaller flaw size geometry significantly improves the unnotched fatigue performance of BJP 316L, as we will later discuss.

7.2.3. Ni-based superalloys

The study of Ganesh et al. [278] focused on the FCG behaviour of LB-DED Inconel 625 and found that the FCG behaviour is considerably inferior to those of its wrought counterpart at the lower stress intensity range, ΔK, of 14 and 24 MPa$\sqrt{}$m, while no differences were seen in the steady-state regime with a m of $\sim$ 3.2. Near-threshold FCG was observed to occur along the columnar facets that lay along the macroscopic crack growth direction. A distinct feature of these alloys is that fine non-equilibrium Laves particles can remain at the interdendritic regions after a non-optimal heat treatment (see Section 3.2, typically associated with overageing) [279]. These regions can become relatively weaker sites, initiating fractures during tensile testing, and are likely to promote FCG in the near-threshold regime.

The role of building direction and heat treatment process in the FCG behaviour of LB-PBF Inconel 625 was reported by Poulin et al. [261]. The ΔK_{th} value stayed independent of porosity levels at 7.18 MPa$\sqrt{}$m at $R = 0.1$, which is to be expected. While the FCG resistance in the AB state is highly dependent on the orientation, heat treatments such as SR and HIP not only improve the FCG behaviour but also reduce its anisotropy. Konečná et al. [280,281] reported an inferior FCG resistance of LB-PBF Inconel 718 in the near-threshold

regime, compared to the wrought alloy, which was attributed to a low content of boron, finer microstructures and residual stress. Boron content was previously shown to enhance the grain boundary cohesion by minimising the deteriorative effect of oxygen and the increase in the resistance to the dislocation movement at the crack tip [282]. A three-fold increase in ΔK_{th} value after HSAT was reported, as some of the aforementioned causes were mitigated through the heat treatment.

7.2.4. Al alloys

Measured values of ΔK_{th} in both AM AlSi12 and AlSi10Mg alloys range between 1 to 1.3 MPa$\sqrt{}$m in its AB state. Although they improve considerably, to between 2 to 3 MPa$\sqrt{}$m, after ageing, they are still lower that the values of 3–3.4 MPa$\sqrt{}$m reported for the cast alloy. This is possibly due to a lower YS of the cast alloy, which results in a relatively larger r_p and hence plasticity-induced crack closure, elevating ΔK_{th}. The higher value of m in the cast alloy of $\sim$ 5, compared the LB-PBF alloy of $\sim$ 3.4, is a result of the presence of significantly larger Si dendrites in the cast alloy's microstructure, whose fracture and debonding within r_p increases the crack velocity per load cycle. Although Si dendrites are also observed in the LB-PBF alloy, the cast alloy exhibits a eutectic structure of Al and Si along with dispersed primary α-Al phase, which are characteristic of a hypo-eutectic composition. This is absent in the LB-PBF alloy. Also, the LB-PBF alloy has a much finer microstructure. Suryawanshi et al. [80] argue that tortuosity arising from the mesostructure results in roughness-induced crack closure and hence reduces the

crack driving force and FCG rates [80]. While LB-PBF AlSi12 exhibits lower ΔK_{th}, it also exhibits slower FCG rates and a significant increase in fracture toughness [80].

8. Unnotched Fatigue

The process-related attributes of AM discussed in Section 4 are particularly detrimental to the high cycle fatigue (HCF) performance of AM alloys. The low HCF strength is most often attributed to the high surface roughness [283–285]; asperities in the surface act as fatigue crack initiation sites. Also, internal defects (in size or number), in particular LOF defects with a low aspect ratio, act as fatigue crack initiation sites [181,182,218]. Thus, both the surface roughness and porosity play a dominant role in controlling the overall fatigue life in AM parts [218]. While residual stresses may also affect the near-threshold FCG, as discussed in Section 7, their influence is less apparent. The material's microstructure exerts a relatively less dominant and indirect influence. However, it affects the incubation period for fatigue crack initiation, which is particularly important for the HCF life, as we will discuss below.

The HCF strength can be improved, for example, by recourse to HIP treatments that transform the microstructure and reduce porosity, and by machining to improve the surface finish. Given the critical role that HCF properties play in selecting both materials and manufacturing methods in the design of structural components, fatigue properties of AM materials must be thoroughly characterised, and strategies for alleviating a low HCF strength identified and implemented. Below, we discuss the HCF behaviour of AM alloys, with emphasis on the structure-property correlations. Unless indicated otherwise, HCF strength is defined by the stress amplitude at which fatigue failure did not occur even after 10^7 cycles. In most cases, it is evaluated using the rotating bending fatigue (RBF) testing methodology where the cyclic stress is fully reversed, i.e., $R = -1$. In some instances, axial fatigue (AXF) tests in tension-tension (typically at $R = 0.1$) are reported, as indicated. The available HCF data for each alloy system are summarised in Tables 9–12.

8.1. Ti6Al4V

Among the possible Ti alloys, only the HCF strength of AM Ti6Al4V has been reported in literature. In the AB condition, the HCF strength of LB-PBF Ti6Al4V is considerably inferior (ranging from 75 to 200 MPa) to that of the wrought alloy (500–650 MPa) [286,287]. Improving the surface finish significantly increases the alloy's HCF strength (200–350 MPa) [182,284,285]. The overall density of the built part has a similar role; Gong et al. [182] reported an improvement from 45 to 180 MPa and 50 to 270 MPa (AXF, $R = 0.1$) for LB-PBF and EB-PBF Ti6Al4V, respectively, by improving the density. Even if the part is subjected to SR, no noticeable improvement in the HCF behaviour is observed [288,289], suggesting that residual stress does not play a critical role in determining the HCF strength.

Both HIP and shot peening considerably improve the HCF strength by closing flaws in the volume and near the surface, respectively. However, the effect of a HIP is limited if a high surface roughness remains unaltered [285,290]. With shot peening, the surface roughness is reduced, allowing for fatigue strength as high as 575 to 610 MPa, which is comparable to the wrought alloy's HCF strength [218,285]. Shot peening offers the advantage of introducing compressive residual stresses near the surface, reducing the surface roughness sensitivity [168,220,288]. More recently, the use of laser shock peening has been proposed by Lan et al. [291], which results in considerably larger case depths of ~ 450 μm with a compressive stress of ~ 350 MPa. Concomitantly, grain refinement and globalisation of the α phase in the peened

regions are observed. The potential improvement in HCF strength was, however, not examined by them.

In the AB state, the HCF strength obtained on machined and polished specimens with highest densities is still inferior to those of the wrought alloys, highlighting the role of the microstructure. AN enhances the fatigue performance by modifying the microstructure to improve the inherent defect tolerance, which is directly related to near-threshold FCG rate, as detailed in Section 7. A detailed analysis of size, shape and distribution of flaws and their effect on HCF behaviour of four different LB-PBF Ti6Al4V, which were produced using different combinations of layer thickness and scan rotations, was carried out by Kumar and Ramamurty [168] so as to examine the influence of flaw characteristics and microstructure on the HCF behaviour. RBF tests were conducted in the AB, heat-treated and shot-peened (SP) conditions. X-ray tomography was utilised to characterise the size, shape, and distribution of the flaws in the alloys. Their results show a significant difference between the HCF strengths of alloys produced using different process parameter combinations (Fig. 15). The HCF strength of alloy produced with a layer thickness (t) of 30 μm and scan rotation (ϕ) of 90° is significantly lower (340 MPa) as compared to that produced with the combination of 60 μm and 67° (475 MPa), even though their relative densities are almost similar (99.63 and 99.83%, respectively). The tomography results show that the flaw sizes and distribution are sensitive to the process parameters utilised. By recourse to the Kitagawa-Takahashi (KT) diagram that predicts the failure envelope, Kumar and Ramamurty [168] rationalised the relatively lower HCF strength in samples built with $\phi = 90°$ to the higher probability of finding flaws with a size greater than a critical size a_i. The value of a_i is directly linked to applied stress and ΔK_{th} of the material within the fracture mechanics framework through:

$$a_i = \frac{1}{\pi} \left(\frac{\Delta K_{th}}{Y \sigma_a} \right)^2 \tag{1}$$

where Y is a geometry factor based on the specimen and flaw geometry, and σ_a is the cyclic stress amplitude. With the known value of ΔK_{th}, a_i can be plotted as a function of σ_a, as shown in Fig. 15a and b shows that the cumulative probability of flaws with $d > 36.5$ μm (a_i corresponding to the HCF strength) is 18% in case coupons built with $\phi = 90°$, as compared to only 2% in those built with $\phi = 67°$. In other words, most of the flaws in the latter case are benign, resulting in a higher HCF strength.

Furthermore, based on the study by Macallister et al. [270], a higher damage tolerance may be possible after DA. Using the same rational as above, a ΔK_{th} of 5.6 MPa$\sqrt{m}$ (in the Z-X direction, $R = 0.1$) results in an increase of $\sim 50\%$ in the critical flaw size. In Kumar and Ramamurty's study [168], the respective increase in HCF performance after DA is due to the increase in ΔK_{th} and the cumulative probability of flaws having a larger diameter than a critical size.

This relationship between the process related attributes of flaw size and distribution as well as surface roughness and the microstructurally dependent ΔK_{th} with HCF strength is critical for the widespread adoption of AM parts in load bearing application as it can be used to predict fatigue life. Moreover, the relationship will hold for other AM metals. For example, Beretta and Romano [292] examined the defect sensitivity of fatigue strengths in LB-PBF AlSi10Mg, while Romano et al. [293] on LB-PBF 17-4PH. Zerbst et al. [294] provides an overview on a damage tolerant design approach for AM metals that is based on the above process related attributes.

Table 9

HCF strength of Ti6Al4V, generated by different AM processes, heat treatment conditions.

Process	Source	Condition	R	Orientation	HCF strength [MPa]	Crack initiation site	Size of defect [µm]	Density [%]
Wrought	[311]		-1		500-600	-	-	-
LB-PBF	[168]	SR (650 °C for 3 h, AC), MP	-1	Z	407 ± 68	near-surface flaw	30-80	99.61-
		DA (920 °C for 0.5 h, FC) + (700 °C for 2 h, AC), MP			425 ± 50	near-surface flaw		99.83
		DA (920 °C for 0.5 h, FC) + (700 °C for 2 h, AC), SP			487 ± 38	internal flaw		
	[181]	AB	0.2	Z	80	internal flaw	200-300	-
		AB, MP		X	200	internal flaw		
	[283]	AB	-1	45° to Z	98 ± 23	surface	-	-
	[290]	AN (820 °C for 4 h, 820 °C for 1.5 h, FC) MP	-1	-	220	Near-surface flaw	-	-
		HIP (920 °C for 2 h, 102MPa)			230	surface		
		HIP, MP			350			
	[289]	SR (650 °C for 3 h, AC)	0.1	45° to Z	210	surface	30-80	99.6
	[288,289]	SR (650 °C for 3 h, AC), MP	0.1	45° to Z	510	LOF flaw	30-80	99.6
	[288]	AB, SP	0.1	45° to Z	435	internal flaw	30-80	99.6
	[362]	SR (800 °C for 2 h), MP	-1	Z	310 ± 40	surface and internal flaw	94-200	-
		SR, HIP (920 °C for 2 h, 100MPa), MP		Z	550	internal flaw		
	[284]	AB	-1	-	200	surface	-	98.6-99.3
		AB, MP			350	internal flaw		
		HIP (900 °C for 2 h, 100 MPa), MP			500	surface		
	[182]	AB, MP	0.1	Z	45	LOF flaw	-	95
					180 ± 20	LOF flaw		99
	[218]	SR (540 °C for 4 h, FC)	0.1	45° to Z	135	surface	-	-
		SR+HIP (810 °C for 2 h, 200 MPa), VP		45° to Z	220 ± 40	surface		
		SR+HIP, MP		45° to Z	225	internal flaw		
		SR+HIP, SB		45° to Z	259	surface		
		SR+HIP, MP		45° to Z	270	internal flaw		
	[285]	AB	-1	Z	155	surface	20-100	-
		HIP (920 °C for 2 h, 100 MPa)		Z	208 ± 13	surface		
		AB, MP		Z	370	near-surface flaw		
		HIP, MP		Z	610	internal flaw		
	[220]	SR (670 °C for 5 h)	-1	Z	221	near-surface flaw	-	99.5
		SR (670 °C for 5 h)	0.1	Z	141	near-surface flaw		
		SR (670 °C for 5 h)	-3	Z	308	near-surface flaw		
		SR, AN (920 °C for 2 h, FC)	-1	Z	191	near-surface flaw		
		SR (670 °C for 5 h), EP	-1	Z	242	near-surface flaw		
		SR (670 °C for 5 h), SP	-1	Z	340	internal flaw		
		HIP (920 °C for 2 h, 100 MPa), VP	-1	Z	350	surface	-	99.9
	[317]	AB, MP	0.1	-	250	internal flaw	-	-
EB-PBF	[362]	AB, MP	-1	Z	375 ± 25	surface	-	-
	[363]	DA (935 °C for 1.75 h, AC), (705 °C for 2 h, AC)	-1	X	221 ± 11	surface	-	-
		DA, CP		X	406 ± 11	internal flaw		
		DA, LSP		X	450 ± 3	internal flaw		
		AB, SP		X	371 ± 7	internal flaw		
	[182]	AB, MP	0.1	Z	50	internal flaw	-	95
		AB, MP		Z	270	internal flaw	99-100	99
	[285]	AB	-1	Z	140	surface	50- 500	-
		HIP (920 °C for 2 h, 100 MPa)		Z	195	surface	-	-
		AB, MP		Z	250 ± 10	near-surface flaw		
		HIP (920 °C for 2 h, pressure of 100 MPa), MP		Z	590	internal flaw		
	[317]	AB, MP	0.1	-	153	near-surface flaw	-	-

8.2. Steels

The available literature on the HCF strength of steels produced using EB-PBF and DED processes is limited, with most of the work reported hitherto being on alloys fabricated using LB-PBF processes. The HCF strengths of austenitic stainless steels such as 316L and 304L produced via AM can be as low as 100 MPa when LOF flaws in them are large [295,296]. Reducing the porosity and surface roughness improves the HCF strength to between 200 to 250 MPa, which is similar to the HCF strengths of the conventionally manufactured steels of similar grain size [297–299]. Wood et al. [300] observed that SR had little effect on the HCF strength. However, as with Ti6Al4V, shot peening results in a significant improvement (20 to 40%) in HCF

Table 10

HCF strength of selected steel grades, generated by different AM processes, heat treatment conditions.

Process/material	Source	Condition	Orientation	R	HCF strength [MPa]	Crack initiation site	Size of defect [μm]	Density [%]
316L, LB-PBF	[297]	AB, MP	Z	-1	210	near-surface flaw	-	-
		AB, MP	X		190	near-surface flaw		
	[295]	AB, Z	Z	0.1	90	surface	-	-
		AB, MP	Z		121	-		
	[296]	AB	Z	-1	90	near-surface flaw	-	-
		AB, VP			125	near-surface flaw		
		AB, MP			160	near-surface flaw		
	[298]	SR (388 °C for 4 h)	X	-1	270	surface	-	-
		SR (388 °C for 4 h)	Z		100	surface		
		SR, HIP (1190 °C for 4 h, 145 MPa)	Z		150	surface		
	[364]	AB, MP	Z	-1	101	LOF flaw		97.7
	[365]	AB, MP	Z	-1	300*	near-surface flaw	-	99.5 ± 0.1
		SR (470 °C for 5 h), MP			300*	near-surface flaw		
	[366]	AB	Z	-1	108*	-	-	-
		AB, MP		-1	267*			
		SR (650 °C for 2 h, FC), MP		-1	294*			
		HIP (1150 °C for 4 h, pressure 100 MPa), MP		-1	317*			
	[300]	AB	X	0.1	90	surface		99.1
			Z	0.1	90	near-surface flaw		
		AB, MP	X	0.1	203	near-surface flaw		
			Z	0.1	135	near-surface flaw		
		SR (470 °C for 5 h), MP	X	0.1	203	internal flaws		
			Z	0.1	68	LOF flaws		
		SP	Z	0.1	124	internal flaw		
	[299]	AB, MP	Z	0.1	125	near-surface flaw	-	-
				-1	250**	unmolten particles		
304L, LB-PBF	[301]	AB	Z	-1	200	surface	-	-
		AB, MP			300	near-surface flaw		
	[302]	AB, MP	Z	-1	250	near-surface flaw	-	>99.0
		AB, MP	Inclined	-1	270	near-surface flaw		
		AB, MP	X	-1	360	near-surface flaw		
18Ni300, LB-PBF	[128]	AB, MP	Z	-1	350	inclusions [Ti/Al]-O	10-30	-
		AB, MP	X	-1	450	near-surface flaw	90-150	
		AB, MP	Z 400 °C	-1	440	internal flaws	10-30	
		AB, MP	X 400 °C	-1	312	LOF flaw	90-150	
	[367]	AB, MP	Z	-1	200*	LOF flaws	200-700	-
		AB, MP	X	-1	105*	LOF flaws	200-700	
	[304]	AG (490 °C for 6h)	Z	-1	400*	near-surface flaw	0-100	-
		AG (490 °C for 6h)	X	-1	250*	near-surface flaw	0-100	
17-4PH, LB-PBF	[298]	AB	X	-1	450	internal flaw	-	-
			Z	-1	250	LOF flaws		
	[368]	AB, MP	X	-1	350	near-surface flaw	-	-
		SA (1050 °C for 4 h), MP	Z	-1	400	near-surface flaw		
	[134]	AB, MP	Z	-1	~175*	near-surface flaw	-	-
		SA (1040 °C for 0.5 h, AC), AG (482 °C for 1 h, AC), MP	Z	-1	~250*	near-surface flaw		
		AB, MP	X	-1	~200*	near-surface flaw		
		SA (1040°C for 0.5 h, AC), AG (482°C for 1 h, AC), MP	X	-1	~300*	Pores near surface		
	[303]	AG (482°C for 1 h, AC), MP	Z	-1	400	near-surface flaw	-	-
		AG (552 °C for 4 h, AC), MP	Z	-1	400	near-surface flaw		
		SA (1050 °C for 0.5 h, AC), AG (482 °C for 1 h, AC)	Z	-1	200	near-surface flaw		
		SA (1050 °C for 0.5 h, AC), AG (482 °C for 1 h, AC), MP	Z	-1	400	near-surface flaw		
		SA (1050 °C for 0.5 h, AC), AG (552 °C for 4 h, AC)	Z	-1	300	near-surface flaw		
		SA (1050 °C for 0.5 h, AC), AG (552 °C for 4 h, AC), MP	Z	-1	400	near-surface flaw		
		SA (1050 °C for 0.5 h, AC), AG (621 °C for 4 h, AC)	Z	-1	300	near-surface flaw		
		SA (1050 °C for 0.5 h, AC), AG (621 °C for 4 h, AC), MP	Z	-1	400	near-surface flaw		

* Run out at 2×10^6 cycles.

** Run out at 10^9 cycles.

Table 11
HCF strength of Inconel 718, generated by different AM processes, heat treatment conditions.

Process	Source	Condition	Orientation	R	HCF strength [MPa]	Crack initiation site	Size of defect [µm]	Density [%]
Wrought	[308]	AMS 5663		-1	450	-	-	-
LB-PBF	[307]	AMS5663, MP	Machine 1, Z	-1	325	near-surface flaw	10-80	-
			Machine 1, X		350	near-surface flaw	10-80	
			Machine 2, Z		200	near-surface flaw	10-160	
			Machine 2, X		300	near-surface flaw	10-119	
	[306]	HIP (1163°C for 3h, 100 MPa), SA+AG -AMS5663	Z, Parallel gauge	-1	292 ± 8	near-surface flaw	50-100	-
		HIP, SA+AG-AMS5663	Z, Parallel gauge	0.1	202	near-surface flaw	-	
		HIP, SA+AG-AMS5663, MP	Z, Parallel gauge	0.1	281	-	-	
		HIP, SA+AG-AMS5663	Z, Hourglass gauge	-1	300	near-surface flaw	-	
		HIP, SA+AG-AMS5663	Z, Hourglass gauge	0.1	202	near-surface flaw	-	
		HIP, SA+AG-AMS5663, MP	X, Parallel gauge	-1	450	-	-	
		HIP, SA+AG-AMS5663 MP	X, Parallel gauge	0.1	281	-	-	
		HIP, SA+AG-AMS5663, MP	X, Parallel gauge	0.5	238	-	-	
		HIP, SA+AG-AMS5663	30° of Z, Parallel gauge	-1	350	near-surface flaw	-	
		HIP, SA+AG-AMS5663	30° of Z, Parallel gauge	0.1	211 ± 9	near-surface flaw	-	
		HIP, SA+AG-AMS5663	30° of Z, Parallel gauge	0.5	141 ± 3	near-surface flaw	-	
	[305]	AB	X	0-0.1	150*	surface	-	-
	[369]	HIP+SA+AG	X	-1	300	surface	100-250	-
		HIP+SA+AG, MP		-1	300	near-surface flaw		
		HIP+SA+AG, H-Charged		-1	350	surface		
		HIP+SA+AG, H-Charged, MP		-1	300	near-surface flaw		
	[370]	SR, MP	X, 400 °C	0.1	234	near-surface flaw	-	-
			X, 600 °C	0.1	180	near-surface flaw		
			Z, 400 °C	0.1	225	near-surface flaw		
			Z, 600 °C	0.1	189	near-surface flaw		
	[169]	AB, MP	Z	-1	~425	surface	75-125	-
					~400**	internal flaw	150-275	-
	[371]	HIP (1163 °C for 3h, 102 MPa) +AG	Z	-1	~220	internal flaw	-	
		HIP (1163 °C for 3h, 102 MPa) +AG, MP			~220	internal flaw		
	[308]	AMS5663, MP	X	-1	350	surface	0.18 flaw, inclusion	-
		AMS5663, MP	X, 500 °C	-1	500	surface		
		AMS5663, MP	45°of Z	-1	400	surface		
		AMS5663, MP	45°of Z, 500 °C	-1	600	surface		
		HIP (1163 °C, 4h, 100MPa) + AMS5663, MP	X, 500 °C	-1	450	surface	twin boundary	
LB-DED	[149]	DA (720 °C for 8h, FC, 620 °C for 8h, AC), MP	650 °C	0.1	~600	non-metallic inclusions		
EB-PBF	[312]	HIP (1200 °C for 4h, 120 MPa), SA (1066 °C for 1h, FC), AG (760 °C for 10h, FC, 649 °C for 10h, AC), MP	X, 650 °C	-1	400**	non-metallic inclusions	-	-
		HIP+SA+AG, MP	Z, 650 °C		550**	non-metallic inclusions		
		HIP+SA+AG, MP	X, 650 °C		450**	non-metallic inclusions		
	[372]	HIP (1200 °C for 4h, 120 MPa), SA (1066 °C for 1h, FC), AG (760 °C for 10h, FC, 649 °C for 10h, AC), MP	Z	0.1	~270	near-surface flaw		

AMS5663 – SA at 954 °C, AC, AG at 718 °C-8 h, FC, 621 °C-10 h, FC.
* Run out at 2 × 10⁶ cycles. ** Run out at 10⁹ cycles.

strength. In general, 304L have a higher HCF strength than 316L [301,302].

Todd et al. [298] reported HCF strengths of 100 and 270 MPa for vertically (Z) and horizontally (X) built LB-PBF 316L specimens, respectively. This anisotropy remains even after HIP, implying that it is related to the difference in the surface roughness arising from the differences in the build directions. Conversely, Mohammad et al. [302] reported HCF strengths of ∼ 250 and ∼ 360 MPa in the Z and X orientations, respectively, after machining and polishing. An HCF strength of ∼ 70 MPa was recorded when the specimen axis is oriented at 45° to the build direction. Based on these results, Mohammad et al. [302] suggest that the anisotropy in HCF strength is related to the inherent weak interfacial strength between the built layers.

Kumar et al. [40] compared the fatigue resistances of 316L produced using the LB-PBF and BJP processes and found that while the HCF strength of LB-PBF alloy is only ∼100 MPa, it is ∼ 250 MPa for the BJP alloy. Notably, the significantly higher HCF strength of the BJP alloy, which is comparable to that of the conventionally manufactured alloy, comes even though its porosity is substantially larger (ranging between 3.7 to 5.6%) as compared to ∼ 2.3 % porosity in LB-PBF alloy. The flaws in BJP specimens are relatively smaller and uniformly distributed, which could be one reason for its better HCF performance. The key reason, however, has microstructural origins. Fatigue cracks that nucleate at internal stress concentrators such as flaw corners, were observed to get arrested at microstructural features such as high angle grain boundaries, annealing twin boundaries, and δ-ferrite phases (see Fig. 16).

Table 12
HCF strength of Al alloys, generated by different AM processes, heat treatment conditions.

Process /material	Source	Condition	Orientation	R	HCF strength [MPa]	Crack initiation site	Size of defect [μm]	Density/porosity [%]
AlSi10Mg, LB-PBF	[315]	SR (300 °C for 2h), MP	Z	-1	75	near-surface flaw	-	98.9 ± 0.1
		SR (300 °C for 2 h), MP, SP (steel balls)			100	internal flaw		
		SR (300 °C for 2 h), MP, SP (ceramic balls)			100	internal flaw		
		SR (300 °C for 2 h), MP, polis hed, SP (steel balls)			110	internal flaw		
		SR (300 °C for 2 h), MP, polished, SP (ceramic balls)			110	internal flaw		
		SR (300 °C for 2 h), MP, SP, EP/MP			105	internal flaw		
	[314]	AB (build platform at 165 °C), MP	Z	-1	120	near-surface flaw		
	[34]	AB (build platform at 180 °C), MP	Z	0.1	28	near-surface flaw	<0.5%	-
		AB (build platform at 180 °C), SA (520 °C for 1 h, WQ), AG (160 °C for 6 h)			42	Surface defects		
		AB (build platform at 180 °C), SA (520 °C for 1 h, WQ), AG (160 °C for 6 h), MP			57	near-surface flaw		
	[156]	AB		-1	100	near-surface flaw	<0.2%	
	[298]	AB, polished	X	-1	~ 80	near-surface, internal flaw	-	>99%
		AB	X	-1	~ 48	near-surface flaw		
			Z	-1	~ 52	near-surface flaw		
	[35]	AB (build platform 150 °C)	Z	-1	36*	Surface defects	-	0.8%
		AB (build platform at 150 °C), SA (560 °C for 1 h, WQ), AG (160 °C for 6 h, WQ)			83*	near-surface flaw		1.6%
		AB, SB			161*	near-surface flaw		0.8%
		AB, SP			176*	near-surface flaw		0.8%
		SA (560 °C for 1 h, WQ), AG (160 °C for 6 h, WQ), SB			162*	surface		1.5%
		SA (560 °C for 1 h, WQ), AG (160 °C for 6 h, WQ), SP			101*	surface		1.5%
	[313]	AB, MP	Z	-1	~ 120	near-surface flaw	-	-
		SR (300°C for 2 h), MP			~ 70	near-surface flaw		
		SR (300°C for 2 h), hIP (250°C for 2 h, 180 MPa), MP			~ 75	near-surface flaw		
AlSi12, LB-PBF	[80]	AB (single melt strategy), MP	Z	-1	60	near-surface flaw	-	-
		AN (300°C for 6 h), MP			110	near-surface flaw		
		AB (cross hatch strategy), MP			70	near-surface flaw		
	[33]	AB, SR (240°C for 2 h), MP	Z	-1	~65	near-surface flaw	-	0.25%
		AB (build platform at 200°C), MP			~100	near-surface flaw		0.12%

* Run out at 2×10^6 cycles.
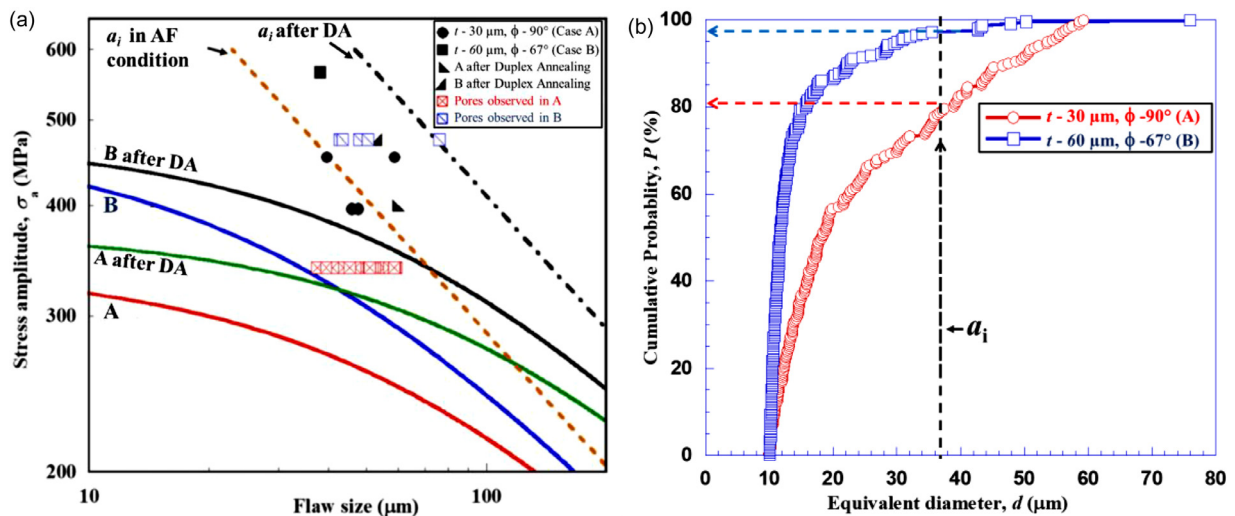
Fig. 15. (a) Kitagawa-Takahashi diagram based on El-Haddad formula for specimens produced with t-ϕ, 30 μm-90° and 60 μm- 67° in AB and heat-treated conditions. Variations of the critical flaw size, a_c, with stress amplitude, σ_a, are plotted along with the flaw sizes. (b) Cumulative probability distribution of the flaw sizes in specimens produced with t-ϕ, 30 μm-90° and 60 μm- 67°. Reprinted with permission from Kumar and Ramamurty [168]. Copyright (2020) Elsevier.
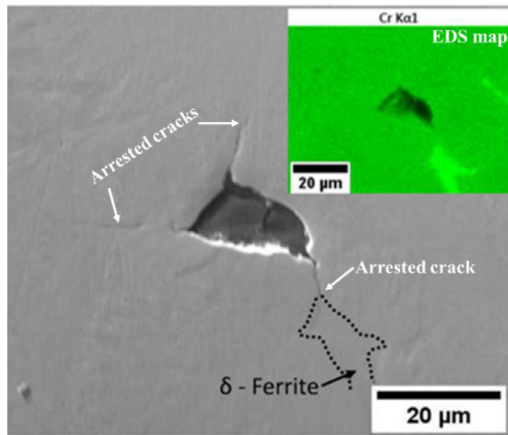
Fig. 16. Micrographs of BJP 316L specimen showing small fatigue crack initiating from all the corners of a flaw observed in the gauge length of fatigue specimens that survived 10^7 cycles at a stress amplitude, σ_a, of 270 MPa. EDS map shown in the inset shows that one of the corner cracks gets arrested by the δ–ferrite present in the matrix. Reprinted with permission from Kumar et al. [40]. Copyright (2020) Elsevier.

Kumar et al. [40] argued that the microstructure resulting from BJP is substantially more effective in arresting the cracks that nucleate under cyclic loading conditions. This is because short cracks maintain their crystallographic nature due to prevalence of planar slip (related to the microstructure in AB condition) and hence get deflected. In the case of LB-PBF specimens, however, a substantially finer microstructure consisting of solidification cells and columnar grains means the fatigue cracks that initiated (from LOF flaws with sizes of 300 to 400 μm) grow unhindered by them.

Nezhadfar et al. [303] measured the HCF strength on machined and polished 17-4 PH steels specimens to be ∼ 400 MPa irrespective of the ageing conditions. If the surface condition remains unaltered after printing (i.e., no machining and polishing was done), HCF strength increases with the increasing ageing temperature, i.e., 200 MPa for H900 and 300 MPa for both H1025 and H1150 treatments. This suggests that over ageing is more beneficial when defects are present.

The HCF strength of AM 18Ni300 specimens in machined and polished conditions are ∼ 350 and ∼ 450 MPa in Z and X-directions, respectively, [128]. During fatigue loading, fatigue cracks can also initiate from [Ti/Al]-O inclusions along with the flaws near the surface. A converse behaviour was observed when testing at a temperature of 400 °C; the measured HCF strengths are ∼ 440 and ∼ 310 MPa in Z and X orientations, respectively, with cracks predominantly initiated from LOF flaws. Ageing treatment (at 490 °C for 6 h) nearly doubled the room temperature HCF strength [304], which suggest in-situ hardening might be the reason behind the improvement in high-temperature fatigue resistance, translating into a higher HCF strength.

8.3. Ni-based superalloys

Most HCF studies that are published on this alloy system to date were focused on Inconel 718, which is also the most popular variant of Ni-based superalloys explored with AM. A low HCF strength of 150–200 MPa (AXF, $R = 0.1$) in the AB state, as compared to 450 MPa for its wrought counterpart, is commonly attributed to the high surface roughness and near-surface defects [305,306].

Yoichi et al. [307] reported two distinct HCF strengths were obtained (between 325 to 350 MPa and 200 to 300 MPa in Z and X orientations, respectively) for the Inconel 718 specimens, which were SR+ST+AG treated as per AMS 5663, produced using two dif-

ferent LB-PBF machines. The relatively lower strength and more pronounced anisotropy in the second set were attributed to a more significant and anisotropic flaw size distribution (10–160 μm in Z and 10–119 μm in X orientated samples), while the first set of specimens had a smaller and similar flaw size distribution (10–80 μm in both the directions).

Witkin et al. [306] evaluated the effect of R, surface condition, and the build orientation of LB-PBF Inconel 718. They obtained a similar HCF strength of ∼ 300 MPa in both the Z and X orientations. Specimens built at an inclination of 30° to Z obtained HCF strength of ∼ 350 MPa. Upon machining, the HCF strength increased to ∼ 450 MPa. Moreover, the effect of R on machined specimens resulted in a decrease to 280 and 240 MPa for AXF for $R = 0.1$ and 0.5, respectively. This is to be expected as the HCF is also controlled by the maximum applied stress.

Little evidence is available on the microstructural attributes, including the presence of Laves and δ phases, on the HCF strength of AM Inconel alloys. Since crystallographic texture is weak, grain size, porosity, content of δ precipitates, and grain boundaries are the main microstructural features that are likely to compete for dictating the fatigue strength. On the one hand, the AM material presents with finer grain structure and the fatigue performances are expected to be better. However, porosity and large content of δ precipitates is likely to overcome this positive effect [308]. In some instances fatigue failure has occurred due to crack initiation from the oxides/carbide inclusions [149,309,310]. Carbides are known to initiate fatigue cracks in the wrought and cast alloy [311]. Their presence is suggested to have originated from the powder itself rather than the LB-PBF process. These types of inclusions are brittle and facilitate easy crack initiation, similar to a pore. Although these inclusions are generally small compared to pores, their effect is difficult to overcome; they cannot be removed with the use of, for example, a HIP treatment.

Shang et al. [149] employed a direct ageing on LB-DED Inconel 718 and measured an HCF strength of 500 MPa (AXF, $R = 0.1$) at 650 °C, which is higher than the room temperature HCF strength. The authors observed that at high-temperature fatigue cracks initiated from the Laves phases rather than flaws. Moreover, cracks were observed to propagate around the Laves phase, indicating an easier crack path in the γ matrix. The authors suggest that the presence of Laves phases may have played a role in hindering crack propagation, which led to the superior high temperature HCF strength. Kirka et al. [312] observed a similar behaviour in EB-PBF Inconel 718, after HIP, SA at 1066 °C, and ageing under a low cycle fatigue regime. Gribben et al. [308] argues that the presence of δ phase results in retardation effect on crack propagation that varies with temperature. While the lack of γ'' weakens the room temperature behaviour, crack retardation is more significant above 500 °C. More work is required to identify the role of the microstructure resultant of AM on the material's HCF strength.

8.4. Al alloys

Siddique et al. [33] reported HCF strength of ∼ 65 MPa for Al-Si parts without build platform heating, compared to ∼ 100 MPa when the build platform was heated to 200 °C. In both cases, an SR heat treatment at 240 °C for 2 h was employed. The 50% improvement in the fatigue strength is attributed to lower porosity (0.12%) in the latter as compared to 0.25% porosity in the former. However, build platform heating also increases the size of the cellular structure due to a reduction in cooling rate, which could also contribute to the 54% improvement in the HCF strength.

An interesting phenomenon observed in both AlSi12 and AlSi10Mg alloys is the effect of SR heat treatment, which increases the overall porosity and flaw size [33,313]. Naor et al. [313] reported an HCF strength of ∼ 120 MPa for machined and polished

AB specimens. However, it dropped to ∼ 70 and ∼ 75 MPa after specimens underwent SR at 300 °C for 2 h and a HIP treatment (at 250 °C, 180 MPa for 2 h), respectively. The SR specimens had the lowest density amongst all the specimens, followed by HIP and AB specimens. The observed reduction in density due to SR and HIP, which is counterintuitive, was attributed to the formation of thermally induced flaws. However, SR at 500 °C followed by HIP resulted in near-fully dense parts. The HCF strength of the AB specimens was attributed to a network of Si particles segregated on the cellular boundaries, apart from the low porosity. Prolonged exposure to high temperature during SR and HIP can break the Si network (as illustrated in Fig. 6), deteriorating tensile and HCF strengths. Coarsened Si particles can act as sites for fatigue crack initiation [313]. Changchum et al. [156] reported a significant drop in HCF strength after SR, solutionising and ageing heat treatments. However, these findings contradict Suryawanshi et al. [80] who reported an improvement in the HCF strength of AlSi12 from 60 MPa to 110 MPa after AN at 400 °C for 6 h.

The coarsening of Si particles during heat treatment, and reduction in their number, in AM AlSi12 and AlSi10Mg alloys depends on the heat treatment temperature. The microstructural changes discussed in Section 3.2 likely affect the fatigue strength, which would explain (in conjunction with flaw size variation) the variation in HCF strength data. For example, Uzan et al. [313] reported an improvement of ΔK_{th} by 80% after T6 heat treatment. Similarly, Aboulkhair et al. [34] reported an improvement in the HCF strength from 28 MPa to 57 MPa after duplex heat treatment at 520 °C for 1 h and 160 °C for 6 h).

Todd et al. [298] reported a negligible effect of the building direction on the HCF strength of LB-PBF AlSi10Mg in the AB condition, i.e., 48 and 52 MPa in specimens build in the X and Z direction, respectively (machining and polishing resulted in a 50% increase in the HCF strength [80,156,298,314]). Naor et al. [315] investigated the effect of shot peening of SR AlSi10Mg before and after mechanical polishing: Polished specimens resulted in a slightly higher HCF strength of ∼ 110 MPa than the shot-peened specimens of ∼ 100 MPa. An AB surface finish resulted in an HCF strength of ∼ 75 MPa. Specimens that were shot-peened and polished (electrochemically and mechanically) resulted in an HCF strength of ∼ 105 MPa. Although compressive residual stresses are present after shot peening (that should significantly reduce the likelihood of crack initiation), the remaining asperities in the surface still resulted in a measurable reduction in HCF strength.

9. Closing remarks

The advent of AM promises to revolutionise metal part fabrication in an unprecedented way. For this potential to be realised such that AM alloys are successfully adapted in industrial practice, an in-depth understanding of the processing-microstructure-mechanical properties is a must. The additional features inherent to AM, such as mesostructures, porosity, residual stresses, and the complex interplay between them complicate this significantly. While considerable effort has already gone into researching the manufacturing aspects of AM and evaluation of the microstructure and tensile properties, research on fracture toughness and fatigue properties is relatively less. Since those properties are critical for ensuring the structural integrity of AM parts (and hence certification), a lot more effort focusing on fatigue and fracture of AM alloys is essential for understanding how these properties are controlled by the features mentioned above. Such knowledge, in turn, can be utilized to design damage-tolerant structural components. In this context, the following unique aspects of AM alloys need to be kept in mind.

- While ductility is an important property that often determines an alloy's applicability in engineering practice, it might not be an all-important one in the context of AM alloys. This is because components in net-shape are fabricated directly, without any need for further 'secondary mechanical processing,' that would, otherwise, make alloy's ductility an important factor. Since the fracture toughness—a key property for which ductility acts as a proxy in most conventionally manufactured alloys—can be enhanced through the mesostructural design, it would be better to focus on the evaluation of fracture toughness directly and how best to further optimize the strength—toughness combinations.

- The rapid solidification conditions that prevail laser-based processes induce metastable and fine microstructural features with extended solid solubilities of the alloying elements in some contexts, while the build strategies impart mesostructural features. While the former enhance strength, the latter can enhance toughness. These additional 'degrees of freedom' offered by AM for designing alloys with enhanced strength-toughness combinations are not fully exploited yet.

- The starting material for most metal AM is in the powder form. Consequently, porosity is inevitable in the as built parts. While post-fabrication treatments such as HIP can significantly reduce (or even eliminate) porosity and lack-of-fusion flaws, they offset the unique advantage of AM in terms of its ability to produce the final part in one step. (Besides, HIP of a part with complex and intricate design features—another key feature of AM—might not that be simple.). In view of this, it appears that the adaption of the 'damage tolerant design' philosophy for components fabricated with AM is the best way for ensuring structural integrity and reliability. In this approach, the existence of defects is taken for granted, which makes the role of the micro and mesostructure on the near-threshold fatigue crack growth and crack closure behaviour important. An improvement in ΔK_{th} imparts a considerable increase in HCF performance by allowing for a larger critical flaw size. Then, fracture mechanics-based approaches are used to ensure the size of the flaws or the lengths of cracks that emanate from them under cyclic loading conditions never exceed the critical flaw sizes. For this, a detailed understanding as to how the processing conditions affect porosity is a must. Since aspects such as the flaw size, shape, and location play a critical role in determining the fatigue life of the part, they need to be characterised in detail.

- The service environment, if it is hydrogen-rich and corrosive, could have a significant effect on the structural integrity of AM alloys as metastable phases, mesostructures, porosity and residual stresses inherent to them can degrade the performance. Hence, aspects such as stress corrosion cracking and hydrogen embrittlement of the alloys produced using AM, which received hardly any attention up to now, need to be investigated.

- While considerable efforts continue to be made in modelling the AM process itself and the microstructural development, mechanics-based modelling of the structure-fracture/fatigue property relations in AM alloys are yet to be investigated. Insights gained through such efforts can be especially useful in tailoring the processing conditions for enhanced damage tolerance, for example in fine tuning the mesostructures for enhanced crack resistance.

Currently, a major impediment to the widespread acceptance of metal AM parts in industry is the spatial variations in the microstructure, high residual stresses, surface finish and the presence of flaws, which is compounded by feedstock, built-to-build and machine-to-machine variability. A thorough understanding of the process-structure (including the attributes)-mechanical property connections would enable insights into which of those are

critical, if at all, and hence easier integration of AM parts with ensured reliability.

Declaration of Competing Interest

The authors declare that they have no known competing financial interests or personal relationships that could have appeared to influence the work reported in this paper.

Acknowledgements

References

[1] D.D. Gu, W. Meiners, K. Wissenbach, R. Poprawe, Laser additive manufacturing of metallic components: materials, processes and mechanisms, Int. Mater. Rev. 57 (2012) 133–164, doi:10.1179/1743280411Y.0000000014.

[2] W.J. Sames, F.A. List, S. Pannala, R.R. Dehoff, S.S. Babu, The metallurgy and processing science of metal additive manufacturing, Int. Mater. Rev. 61 (2016) 315–360, doi:10.1080/09506608.2015.1116649.

[3] D. Herzog, V. Seyda, E. Wycisk, C. Emmelmann, Additive manufacturing of metals, Acta Mater 117 (2016) 371–392, doi:10.1016/j.actamat.2016.07.019.

[4] T. DebRoy, H.L. Wei, J.S. Zuback, T. Mukherjee, J.W. Elmer, J.O. Milewski, A.M. Beese, A. Wilson-Heid, A. De, W. Zhang, Additive manufacturing of metallic components – Process, structure and properties, Prog. Mater. Sci. 92 (2018) 112–224, doi:10.1016/j.pmatsci.2017.10.001.

[5] A. Mostafaei, A.M. Elliott, J.E. Barnes, F. Li, W. Tan, C.L. Cramer, P. Nandwana, M. Chmielus, Binder jet 3D printing – Process parameters, materials, properties, and challenges, Prog. Mater. Sci. (2020) 100707, doi:10.1016/j.pmatsci.2020.100707.

[6] B. Dutta, F.H. Sam Froes, The additive manufacturing (AM) of titanium alloys, in: Titanium Powder Metallurgy Science, Technology and Applications, Elsevier, 2015, pp. 447–468, doi:10.1016/B978-0-12-800054-0.00024-1.

[7] D. Agius, K. Kourousis, C. Wallbrink, A review of the as-built SLM Ti-6Al-4V mechanical properties towards achieving fatigue resistant designs, Metals 8 (2018) 75, doi:10.3390/met8010075.

[8] C. Romero, F. Yang, L. Bolzoni, Fatigue and fracture properties of Ti alloys from powder-based processes – A review, Int. J. Fatigue. 117 (2018) 407–419, doi:10.1016/j.ijfatigue.2018.08.029.

[9] S. Liu, Y.C. Shin, Additive manufacturing of Ti6Al4V alloy: A review, Mater. Des. 164 (2019) 107552, doi:10.1016/j.matdes.2018.107552.

[10] N.T. Aboulkhair, M. Simonelli, L. Parry, I. Ashcroft, C. Tuck, R. Hague, 3D printing of aluminium alloys: additive manufacturing of aluminium alloys using selective laser melting, Prog. Mater. Sci. 106 (2019) 100578, doi:10.1016/j.pmatsci.2019.100578.

[11] H. Fayazfar, M. Salarian, A. Rogalsky, D. Sarker, P. Russo, V. Paserin, E. Toyserkani, A critical review of powder-based additive manufacturing of ferrous alloys: process parameters, microstructure and mechanical properties, Mater. Des. 144 (2018) 98–128, doi:10.1016/j.matdes.2018.02.018.

[12] P. Bajaj, A. Hariharan, A. Kini, P. Kürnsteiner, D. Raabe, E.A. Jägle, Steels in additive manufacturing: a review of their microstructure and properties, Mater. Sci. Eng. A. (2020) 772, doi:10.1016/j.msea.2019.138633.

[13] S.S. Babu, N. Raghavan, J. Raplee, S.J. Foster, C. Frederick, M. Haines, R. Dinwiddie, M.K. Kirka, A. Plotkowski, Y. Lee, R.R. Dehoff, Additive manufacturing of nickel superalloys: opportunities for innovation and challenges related to qualification, Metall. Mater. Trans. A Phys. Metall. Mater. Sci. 49 (2018) 3764–3780, doi:10.1007/s11661-018-4702-4.

[14] A.N. Jinoop, C.P. Paul, K.S. Bindra, Laser-assisted directed energy deposition of nickel super alloys: a review, Proc. Inst. Mech. Eng. Part L J. Mater. Des. Appl. 233 (2019) 2376–2400, doi:10.1177/1464420719852658.

[15] J.J. Lewandowski, M. Seifi, Metal additive manufacturing: a review of mechanical properties, Annu. Rev. Mater. Res. 46 (2016) 151–186, doi:10.1146/annurev-matsci-070115-032024.

[16] N. Sanaei, A. Fatemi, Defects in additive manufactured metals and their effect on fatigue performance: a state-of-the-art review, Prog. Mater. Sci. (2020) 100724, doi:10.1016/j.pmatsci.2020.100724.

[17] N. Shamsaei, A. Yadollahi, L. Bian, S.M. Thompson, An overview of direct laser deposition for additive manufacturing; part II: mechanical behavior, process parameter optimization and control, Addit. Manuf. 8 (2015) 12–35, doi:10.1016/j.addma.2015.07.002.

[18] S.M. Thompson, L. Bian, N. Shamsaei, A. Yadollahi, An overview of direct laser deposition for additive manufacturing; part I: transport phenomena, modeling and diagnostics, Addit. Manuf. 8 (2015) 36–62, doi:10.1016/j.addma.2015.07.001.

[19] B. Fotovvati, N. Namdari, A. Dehghanghadikolaei, Fatigue performance of selective laser melted Ti6Al4V components: state of the art, Mater. Res. Express 6 (2018) 012002, doi:10.1088/2053-1591/aae10e.

[20] ISO/ASTM, ISO/ASTM 52900 Additive Manufacturing - General Principles - Terminology, 2015.

[21] R. Liu, Z. Wang, T. Sparks, F. Liou, J. Newkirk, Aerospace applications of laser additive manufacturing, in: M. Brandt (Ed.), Laser Additive Manufacturing: Materials, Design, Technologies, and Applications, Elsevier, 2017, pp. 351–371, doi:10.1016/B978-0-08-100433-3.00013-0.

[22] S. Tammas-Williams, H. Zhao, F. Léonard, F. Derguti, I. Todd, P.B.B. Prangnell, XCT analysis of the influence of melt strategies on defect population in Ti-6Al-4V components manufactured by selective electron beam melting, Mater. Charact. 102 (2015) 47–61, doi:10.1016/j.matchar.2015.02.008.

[23] W.E. Frazier, Metal additive manufacturing: a review, J. Mater. Eng. Perform. 23 (2014) 1917–1928, doi:10.1007/s11665-014-0958-z.

[24] C.Y. Yap, C.K. Chua, Z.L. Dong, Z.H. Liu, D.Q. Zhang, L.E. Loh, S.L. Sing, Review of selective laser melting: materials and applications, Appl. Phys. Rev. 2 (2015) 041101, doi:10.1063/1.4935926.

[25] T. Kurzynowski, E. Chlebus, B. Kuźnicka, J. Reiner, Parameters in selective laser melting for processing metallic powders, High Power Laser Materials Processing: Lasers, Beam Delivery, Diagnostics, and Applications, 2012, doi:10.1117/12.907292.

[26] G. Chen, S.Y. Zhao, P. Tan, J. Wang, C.S. Xiang, H.P. Tang, A comparative study of Ti-6Al-4V powders for additive manufacturing by gas atomization, plasma rotating electrode process and plasma atomization, Powder Technol. 333 (2018) 38–46, doi:10.1016/j.powtec.2018.04.013.

[27] P. Sun, Z.Z. Fang, Y. Zhang, Y. Xia, Review of the methods for production of spherical Ti and Ti alloy powder, JOM 69 (2017) 1853–1860, doi:10.1007/s11837-017-2513-5.

[28] Concept Laser GmbH, (n.d.). 2020 www.concept-laser.com.

[29] EOS Electro Optical Systems GmbH, (n.d.). 2020 www.eos.info.

[30] SLM Solutions GmbH, (n.d.). 2020 www.slm-solutions.com.

[31] Arcam EBM, (n.d.). 2020 http://www.arcam.com.

[32] Realizer GmbH, (n.d.). 2020 www.realizer.com.

[33] S. Siddique, M. Imran, F. Walther, Very high cycle fatigue and fatigue crack propagation behavior of selective laser melted AlSi12 alloy, Int. J. Fatigue 94 (2017) 246–254, doi:10.1016/j.ijfatigue.2016.06.003.

[34] N.T. Aboulkhair, I. Maskery, C. Tuck, I. Ashcroft, N.M. Everitt, Improving the fatigue behaviour of a selectively laser melted aluminium alloy: Influence of heat treatment and surface quality, Mater. Des. 104 (2016) 174–182, doi:10.1016/j.matdes.2016.05.041.

[35] S. Bagherifard, N. Beretta, S. Monti, M. Riccio, M. Bandini, M. Guagliano, On the fatigue strength enhancement of additive manufactured AlSi10Mg parts by mechanical and thermal post-processing, Mater. Des. 145 (2018) 28–41, doi:10.1016/j.matdes.2018.02.055.

[36] X. Gong, T. Anderson, K. Chou, Review on powder-based electron beam additive manufacturing technology, Manuf. Rev. 1 (2014), doi:10.1051/mfreview/2014001.

[37] S.S. Al-Bermani, M.L. Blackmore, W. Zhang, I. Todd, The origin of microstructural diversity, texture, and mechanical properties in electron beam melted Ti-6Al-4V, Metall. Mater. Trans. A Phys. Metall. Mater. Sci. 41 (2010) 3422–3434, doi:10.1007/s11661-010-0397-x.

[38] G.P. Dinda, L. Song, J. Mazumder, Fabrication of Ti-6Al-4V scaffolds by direct metal deposition, Metall. Mater. Trans. A Phys. Metall. Mater. Sci. 39 (2008) 2914–2922, doi:10.1007/s11661-008-9634-y.

[39] I. Gibson, D. Rosen, B. Stucker, M. Khorasani, I. Gibson, D. Rosen, B. Stucker, M. Khorasani, Directed energy deposition, in: Additive Manufacturing Technologies, Springer International Publishing, 2021, pp. 285–318, doi:10.1007/978-3-030-56127-7_10.

[40] P. Kumar, R. Jayaraj, J. Suryawanshi, U.R. Satwik, J. McKinnell, U. Ramamurty, Fatigue strength of additively manufactured 316L austenitic stainless steel, Acta Mater 199 (2020) 225–239, doi:10.1016/j.actamat.2020.08.033.

[41] F. Dini, S.A. Ghaffari, J. Jafar, R. Hamidreza, S. Marjan, A review of binder jet process parameters; powder, binder, printing and sintering condition, Met. Powder Rep. 75 (2020) 95–100, doi:10.1016/j.mprp.2019.05.001.

[42] T. Fujieda, M. Chen, H. Shiratori, K. Kuwabara, K. Yamanaka, Y. Koizumi, A. Chiba, S. Watanabe, Mechanical and corrosion properties of CoCrFeNiTi-based high-entropy alloy additive manufactured using selective laser melting, Addit. Manuf. 25 (2019) 412–420, doi:10.1016/j.addma.2018.10.023.

[43] T. Fujieda, H. Shiratori, K. Kuwabara, M. Hirota, T. Kato, K. Yamanaka, Y. Koizumi, A. Chiba, S. Watanabe, CoCrFeNiTi-based high-entropy alloy with superior tensile strength and corrosion resistance achieved by a combination of additive manufacturing using selective electron beam melting and solution treatment, Mater. Lett. 189 (2017) 148–151, doi:10.1016/j.matlet.2016.11.026.

[44] P. Wang, P. Huang, F.L. Ng, W.J. Sin, S. Lu, M.L.S. Nai, Z.L. Dong, J. Wei, Additively manufactured CoCrFeNiMn high-entropy alloy via pre-alloyed powder, Mater. Des. 168 (2019) 107576, doi:10.1016/j.matdes.2018.107576.

[45] D. Lin, L. Xu, H. Jing, Y. Han, L. Zhao, Y. Zhang, H. Li, A strong, ductile, high-entropy FeCoCrNi alloy with fine grains fabricated via additive manufacturing and a single cold deformation and annealing cycle, Addit. Manuf. 36 (2020) 101591, doi:10.1016/j.addma.2020.101591.

[46] W. Wu, R. Zhou, B. Wei, S. Ni, Y. Liu, M. Song, Nanosized precipitates and dislocation networks reinforced C-containing CoCrFeNi high-entropy alloy fabricated by selective laser melting, Mater. Charact. 144 (2018) 605–610, doi:10.1016/j.matchar.2018.08.019.

[47] R. Zhou, Y. Liu, C. Zhou, S. Li, W. Wu, M. Song, B. Liu, X. Liang, P.K. Liaw, Microstructures and mechanical properties of C-containing FeCoCrNi high-entropy alloy fabricated by selective laser melting, Intermetallics 94 (2018) 165–171, doi:10.1016/j.intermet.2018.01.002.

[48] P.F. Zhou, D.H. Xiao, Z. Wu, X.Q. Ou, Al0.5FeCoCrNi high entropy alloy prepared by selective laser melting with gas-atomized pre-alloy powders, Mater. Sci. Eng. A 739 (2019) 86–89, doi:10.1016/j.msea.2018.10.035.

[49] P. Agrawal, S. Thapliyal, S.S.S. Nene, R.S.S. Mishra, B.A.A. McWilliams, K.C.C. Cho, Excellent strength-ductility synergy in metastable high entropy alloy by laser powder bed additive manufacturing, Addit. Manuf. 32 (2020) 1–7, doi:10.1016/j.addma.2020.101098.

[50] Z.G. Zhu, Q.B. Nguyen, F.L. Ng, X.H. An, X.Z. Liao, P.K. Liaw, S.M.L. Nai, J. Wei, Hierarchical microstructure and strengthening mechanisms of a CoCrFeNiMn high entropy alloy additively manufactured by selective laser melting, Scr. Mater. 154 (2018) 20–24, doi:10.1016/j.scriptamat.2018.05.015.

[51] R. Li, P. Niu, T. Yuan, P. Cao, C. Chen, K. Zhou, Selective laser melting of an equiatomic CoCrFeMnNi high-entropy alloy: Processability, non-equilibrium microstructure and mechanical property, J. Alloys Compd. 746 (2018) 125–134, doi:10.1016/j.jallcom.2018.02.298.

[52] S. Xiang, H. Luan, J. Wu, K.F. Yao, J. Li, X. Liu, Y. Tian, W. Mao, H. Bai, G. Le, Q. Li, Microstructures and mechanical properties of CrMnFeCoNi high entropy alloys fabricated using laser metal deposition technique, J. Alloys Compd. 773 (2019) 387–392, doi:10.1016/j.jallcom.2018.09.235.

[53] L. Zhou, T. Yuan, J. Tang, J. He, R. Li, Mechanical and corrosion behavior of titanium alloys additively manufactured by selective laser melting – A comparison between nearly β titanium, α titanium and $\alpha+\beta$ titanium, Opt. Laser Technol. 119 (2019) 105625, doi:10.1016/j.optlastec.2019.105625.

[54] H. Fan, S. Yang, Effects of direct aging on near-alpha Ti–6Al–2Sn–4Zr–2Mo (Ti-6242) titanium alloy fabricated by selective laser melting (SLM), Mater. Sci. Eng. A 788 (2020) 139533, doi:10.1016/j.msea.2020.139533.

[55] Y. Zhai, H. Galarraga, D.A. Lados, Microstructure evolution, tensile properties, and fatigue damage mechanisms in Ti-6Al-4V alloys fabricated by two additive manufacturing techniques, Procedia Eng. (2015) 658–666, doi:10.1016/j.proeng.2015.08.007.

[56] H. REN, X. TIAN, D. LIU, J. LIU, H. WANG, Microstructural evolution and mechanical properties of laser melting deposited Ti–6.5Al–3.5Mo–1.5Zr–0.3Si titanium alloy, Trans. Nonferrous Met. Soc. China 25 (2015) 1856–1864, doi:10.1016/S1003-6326(15)63792-X.

[57] X. Zhang, B. Mao, Y. Liao, Y. Zheng, Selective laser melting of graphene oxide-reinforced Ti-48Al-2Cr-2Nb: improved manufacturability and mechanical strength, J. Mater. Res. 35 (2020) 1998–2005, doi:10.1557/jmr.2020.63.

[58] M. Seifi, A.A. Salem, D.P. Satko, U. Ackelid, S.L. Semiatin, J.J. Lewandowski, Effects of HIP on microstructural heterogeneity, defect distribution and mechanical properties of additively manufactured EBM Ti-48Al-2Cr-2Nb, J. Alloys Compd. 729 (2017) 1118–1135, doi:10.1016/j.jallcom.2017.09.163.

[59] B. Lin, W. Chen, Y. Yang, F. Wu, Z. Li, Anisotropy of microstructure and tensile properties of Ti–48Al–2Cr–2Nb fabricated by electron beam melting, J. Alloys Compd. 830 (2020) 154684, doi:10.1016/j.jallcom.2020.154684.

[60] J. Bieske, M. Franke, M. Schloffer, C. Körner, Microstructure and properties of TiAl processed via an electron beam powder bed fusion capsule technology, Intermetallics (2020) 126, doi:10.1016/j.intermet.2020.106929.

[61] M.J. Holzweissig, A. Taube, F. Brenne, M. Schaper, T. Niendorf, Microstructural characterization and mechanical performance of hot work tool steel processed by selective laser melting, Metall. Mater. Trans. B 46 (2015) 545–549, doi:10.1007/s11663-014-0267-9.

[62] R. Mertens, B. Vrancken, N. Holmstock, Y. Kinds, J.P. Kruth, J. Van Humbeeck, Influence of powder bed preheating on microstructure and mechanical properties of H13 tool steel SLM parts, Phys. Procedia (2016) 882–890, doi:10.1016/j.phpro.2016.08.092.

[63] M. Mazur, P. Brincat, M. Leary, M. Brandt, Numerical and experimental evaluation of a conformally cooled H13 steel injection mould manufactured with selective laser melting, Int. J. Adv. Manuf. Technol. 93 (2017) 881–900, doi:10.1007/s00170-017-0426-7.

[64] J. Mazumder, J. Choi, K. Nagarathnam, J. Koch, D. Hetzner, The direct metal deposition of H13 tool steel for 3-D components, Jom 49 (1997) 55–60, doi:10.1007/BF02914687.

[65] L. Xue, J. Chen, S.H. Wang, Freeform laser consolidated H13 and CPM 9V tool steels, Metallogr. Microstruct. Anal. 2 (2013) 67–78, doi:10.1007/s13632-013-0061-0.

[66] X. Zhao, Q. Wei, B. Song, Y. Liu, X. Luo, S. Wen, Y. Shi, Fabrication and characterization of AISI 420 stainless steel using selective laser melting, Mater. Manuf. Process 30 (2015) 1283–1289, doi:10.1080/10426914.2015.1026351.

[67] S.L. Lu, G.K. Meenashisundaram, P. Wang, S.M.L. Nai, J. Wei, The combined influence of elevated pre-sintering and subsequent bronze infiltration on the microstructures and mechanical properties of 420 stainless steel additively manufactured via binder jet printing, Addit. Manuf. 34 (2020) 101266, doi:10.1016/j.addma.2020.101266.

[68] D.K. Kim, W. Woo, E.Y. Kim, S.H. Choi, Microstructure and mechanical characteristics of multi-layered materials composed of 316L stainless steel and ferritic steel produced by direct energy deposition, J. Alloys Compd. 774 (2019) 896–907, doi:10.1016/j.jallcom.2018.09.390.

[69] F. Weng, Y. Liu, Y. Chew, X. Yao, S. Sui, C. Tan, F.L. Ng, G. Bi, IN100 Ni-based superalloy fabricated by micro-laser aided additive manufacturing: correlation of the microstructure and fracture mechanism, Mater. Sci. Eng. A 788 (2020) 139467, doi:10.1016/j.msea.2020.139467.

[70] C. Brice, R. Shenoy, M. Kral, K. Buchannan, Precipitation behavior of aluminum alloy 2139 fabricated using additive manufacturing, Mater. Sci. Eng. A 648 (2015) 9–14, doi:10.1016/j.msea.2015.08.088.

[71] K. Schmidtke, F. Palm, A. Hawkins, C. Emmelmann, Process and mechanical properties: applicability of a scandium modified Al-alloy for laser additive manufacturing, Phys. Procedia 12 (2011) 369–374, doi:10.1016/j.phpro.2011.03.047.

[72] P. Nandwana, M.M. Kirka, V.C. Paquit, S. Yoder, R.R. Dehoff, Correlations between powder feedstock quality, in situ porosity detection, and fatigue behavior of Ti-6Al-4V fabricated by powder bed electron beam melting: a step towards qualification, JOM 70 (2018) 1686–1691, doi:10.1007/s11837-018-3034-6.

[73] Y. Sun, M. Aindow, R.J. Hebert, Comparison of virgin Ti-6Al-4V powders for additive manufacturing, Addit. Manuf. 21 (2018) 544–555, doi:10.1016/j.addma.2018.02.011.

[74] A.T. Sutton, C.S. Kriewall, M.C. Leu, J.W. Newkirk, Powder characterisation techniques and effects of powder characteristics on part properties in powder-bed fusion processes, Virtual Phys. Prototyp. 12 (2017) 3–29, doi:10.1080/17452759.2016.1250605.

[75] J.M. Benson, E. Snyders, The need for powder characterisation in the additive manufacturing industry and the establishment of a national facility, S. Afr. J. Ind. Eng. 26 (2015) 104–114, doi:10.7166/26-2-951.

[76] H.P. Tang, M. Qian, N. Liu, X.Z. Zhang, G.Y. Yang, J. Wang, Effect of powder reuse times on additive manufacturing of Ti-6Al-4V by selective electron beam melting, JOM 67 (2015) 555–563, doi:10.1007/s11837-015-1300-4.

[77] P. Nandwana, A.M. Elliott, D. Siddel, A. Merriman, W.H. Peter, S.S. Babu, Powder bed binder jet 3D printing of Inconel 718: densification, microstructural evolution and challenges☆, Curr. Opin. Solid State Mater. Sci. 21 (2017) 207–218, doi:10.1016/j.cossms.2016.12.002.

[78] K.G. Prashanth, J. Eckert, Formation of metastable cellular microstructures in selective laser melted alloys, J. Alloys Compd. 707 (2017) 27–34, doi:10.1016/j.jallcom.2016.12.209.

[79] K.M. Bertsch, G. Meric de Bellefon, B. Kuehl, D.J. Thoma, Origin of dislocation structures in an additively manufactured austenitic stainless steel 316L, Acta Mater. 199 (2020) 19–33, doi:10.1016/j.actamat.2020.07.063.

[80] J. Suryawanshi, K.G. Prashanth, S. Scudino, J. Eckert, O. Prakash, U. Ramamurty, Simultaneous enhancements of strength and toughness in an Al-12Si alloy synthesized using selective laser melting, Acta Mater. 115 (2016) 285–294, doi:10.1016/j.actamat.2016.06.009.

[81] J. Suryawanshi, K.G. Prashanth, U. Ramamurty, Mechanical behavior of selective laser melted 316L stainless steel, Mater. Sci. Eng. A 696 (2017) 113–121, doi:10.1016/j.msea.2017.04.058.

[82] Y. Zhong, L.E. Rännar, L. Liu, A. Koptyug, S. Wikman, J. Olsen, D. Cui, Z. Shen, Additive manufacturing of 316L stainless steel by electron beam melting for nuclear fusion applications, J. Nucl. Mater. 486 (2017) 234–245, doi:10.1016/j.jnucmat.2016.12.042.

[83] D. Dai, D. Gu, R. Poprawe, M. Xia, Influence of additive multilayer feature on thermodynamics, stress and microstructure development during laser 3D printing of aluminum-based material, Sci. Bull. 62 (2017) 779–787, doi:10.1016/j.scib.2017.05.007.

[84] D. Wang, C. Song, Y. Yang, Y. Bai, Investigation of crystal growth mechanism during selective laser melting and mechanical property characterization of 316L stainless steel parts, Mater. Des. 100 (2016) 291–299, doi:10.1016/j.matdes.2016.03.111.

[85] Y.M. Wang, T. Voisin, J.T. McKeown, J. Ye, N.P. Calta, Z. Li, Z. Zeng, Y. Zhang, W. Chen, T.T. Roehling, R.T. Ott, M.K. Santala, P.J. Depond, M.J. Matthews, A.V Hamza, T. Zhu, Additively manufactured hierarchical stainless steels with high strength and ductility, Nat. Mater. 17 (2018) 63–71, doi:10.1038/nmat5021.

[86] K. Saeidi, X. Gao, Y. Zhong, Z.J. Shen, Hardened austenite steel with columnar sub-grain structure formed by laser melting, Mater. Sci. Eng. A 625 (2015) 221–229, doi:10.1016/j.msea.2014.12.018.

[87] L. Liu, Q. Ding, Y. Zhong, J. Zou, J. Wu, Y.L. Chiu, J. Li, Z. Zhang, Q. Yu, Z. Shen, Dislocation network in additive manufactured steel breaks strength–ductility trade-off, Mater. Today 21 (2018) 354–361, doi:10.1016/j.mattod.2017.11.004.

[88] A.J. Birnbaum, J.C. Steuben, E.J. Barrick, A.P. Iliopoulos, J.G. Michopoulos, Intrinsic strain aging, Σ3 boundaries, and origins of cellular substructure in additively manufactured 316L, Addit. Manuf. 29 (2019) 100784, doi:10.1016/j.addma.2019.100784.

[89] N. Takata, H. Kodaira, K. Sekizawa, A. Suzuki, M. Kobashi, Change in microstructure of selectively laser melted AlSi10Mg alloy with heat treatments, Mater. Sci. Eng. A 704 (2017) 218–228, doi:10.1016/j.msea.2017.08.029.

[90] Y.S.J. Yoo, T.A. Book, M.D. Sangid, J. Kacher, Identifying strain localization and dislocation processes in fatigued Inconel 718 manufactured from selective laser melting, Mater. Sci. Eng. A 724 (2018) 444–451, doi:10.1016/j.msea.2018.03.127.

[91] Y. Zhao, K. Aoyagi, K. Yamanaka, A. Chiba, Role of operating and environmental conditions in determining molten pool dynamics during electron beam melting and selective laser melting, Addit. Manuf. 36 (2020) 101559, doi:10.1016/j.addma.2020.101559.

[92] O. Andreau, I. Koutiri, P. Peyre, J.D. Penot, N. Saintier, E. Pessard, T. De Terris, C. Dupuy, T. Baudin, Texture control of 316L parts by modulation of the melt pool morphology in selective laser melting, J. Mater. Process. Technol. 264 (2019) 21–31, doi:10.1016/j.jmatprotec.2018.08.049.

[93] S. Gao, Z. Hu, M. Duchamp, P.S.S.R. Krishnan, S. Tekumalla, X. Song, M. Seita, Recrystallization-based grain boundary engineering of 316L stainless steel produced via selective laser melting, Acta Mater 200 (2020) 366–377, doi:10.1016/j.actamat.2020.09.015.

[94] M. Laleh, A.E. Hughes, M.Y. Tan, G.S. Rohrer, S. Primig, N. Haghdadi, Grain boundary character distribution in an additively manufactured austenitic stainless steel, Scr. Mater. 192 (2021) 115–119, doi:10.1016/j.scriptamat.2020.10.018.

[95] A. Bauereiß, T. Scharowsky, C. Körner, Defect generation and propagation mechanism during additive manufacturing by selective beam melting, J. Mater. Process Technol. 214 (2014) 2522–2528, doi:10.1016/j.jmatprotec.2014.05.002.

[96] S. Huang, R.L. Narayan, J.H.K. Tan, S.L. Sing, W.Y. Yeong, Resolving the porosity-unmelted inclusion dilemma during *in-situ* alloying of Ti34Nb via laser powder bed fusion, Acta Mater. 204 (2020) 116522, doi:10.1016/j.actamat.2020.116522.

[97] P. Kumar, O. Prakash, U. Ramamurty, Micro-and meso-structures and their influence on mechanical properties of selectively laser melted Ti-6Al-4V, Acta Mater. 154 (2018) 246–260, doi:10.1016/j.actamat.2018.05.044.

[98] P. Kumar, U. Ramamurty, Microstructural optimization through heat treatment for enhancing the fracture toughness and fatigue crack growth resistance of selective laser melted Ti–6Al–4V alloy, Acta Mater. 169 (2019) 45–59, doi:10.1016/j.actamat.2019.03.003.

[99] P.H. Lai, J.K. Chen, M.W. Wu, The transverse rupture strength in Ti-6Al-4V alloy manufactured by selective laser melting, in: MATEC Web of Conferences, 2015, pp. 1–5, doi:10.1051/matecconf/20152702010.

[100] L. Thijs, F. Verhaeghe, T. Craeghs, J. Van Humbeeck, J.P. Kruth, A study of the microstructural evolution during selective laser melting of Ti-6Al-4V, Acta Mater. 58 (2010) 3303–3312, doi:10.1016/j.actamat.2010.02.004.

[101] P.L. Stephenson, N. Haghdadi, R. DeMott, X.Z. Liao, S.P. Ringer, S. Primig, Effect of scanning strategy on variant selection in additively manufactured Ti-6Al-4V, Addit. Manuf. 36 (2020) 101581, doi:10.1016/j.addma.2020.101581.

[102] J. Yang, H. Yu, J. Yin, M. Gao, Z. Wang, X. Zeng, Formation and control of martensite in Ti-6Al-4V alloy produced by selective laser melting, Mater. Des. 108 (2016) 308–318, doi:10.1016/j.matdes.2016.06.117.

[103] G.M. Ter Haar, T.H. Becker, Selective laser melting produced Ti-6Al-4V: Post-process heat treatments to achieve superior tensile properties, Materials 11 (2018) 146, doi:10.3390/ma11010146.

[104] C.J. Todaro, M.A. Easton, D. Qiu, D. Zhang, M.J. Bermingham, E.W. Lui, M. Brandt, D.H. StJohn, M. Qian, Grain structure control during metal 3D printing by high-intensity ultrasound, Nat. Commun. 11 (2020) 1–9, doi:10.1038/s41467-019-13874-z.

[105] M.J. Bermingham, D. Kent, H. Zhan, D.H. Stjohn, M.S. Dargusch, Controlling the microstructure and properties of wire arc additive manufactured Ti-6Al-4V with trace boron additions, Acta Mater. 91 (2015) 289–303, doi:10.1016/j.actamat.2015.03.035.

[106] T. Wang, Y.Y. Zhu, S.Q. Zhang, H.B. Tang, H.M. Wang, Grain morphology evolution behavior of titanium alloy components during laser melting deposition additive manufacturing, J. Alloys Compd. 632 (2015) 505–513, doi:10.1016/j.jallcom.2015.01.256.

[107] M.J. Bermingham, D.H. StJohn, J. Krynen, S. Tedman-Jones, M.S. Dargusch, Promoting the columnar to equiaxed transition and grain refinement of titanium alloys during additive manufacturing, Acta Mater. 168 (2019) 261–274, doi:10.1016/j.actamat.2019.02.020.

[108] E. Leey, R. Banerjee, S. Kary, D. Bhattacharyyay, H.L. Frasery, Selection of α variants during microstructural evolution in α/β titanium alloys, Philos. Mag. 87 (2007) 3615–3627, doi:10.1080/14786430701373672.

[109] D. Banerjee, J.C. Williams, Perspectives on titanium science and technology, Acta Mater. 61 (2013) 844–879, doi:10.1016/j.actamat.2012.10.043.

[110] G.A. Sargent, K.T. Kinsel, A.L. Pilchak, A.A. Salem, S.L. Semiatin, Variant selection during cooling after beta annealing of Ti-6Al-4V ingot material, Metall. Mater. Trans. A Phys. Metall. Mater. Sci. 43 (2012) 3570–3585, doi:10.1007/s11661-012-1245-y.

[111] S. Banerjee, R. Krishnan, Martensitic transformation in zirconium-niobium alloys, Acta Metall 19 (1971) 1317–1326, doi:10.1016/0001-6160(71)90068-X.

[112] P. Gaunt, J.W. Christian, The crystallography of the β-α transformation in zirconium and in two titanium-molybdenum alloys, Acta Metall. 7 (1959) 534–543, doi:10.1016/0001-6160(59)90189-0.

[113] G.M. Ter Haar, T.H. Becker, The influence of microstructural texture and prior beta grain recrystallisation on the deformation behaviour of laser powder bed fusion produced Ti-6Al-4V, Mater. Sci. Eng. A (2021) 141185, doi:10.1016/j.msea.2021.141185.

[114] N. Sridharan, A. Chaudhary, P. Nandwana, S.S. Babu, Texture evolution during laser direct metal deposition of Ti-6Al-4V, JOM 68 (2016) 772–777, doi:10.1007/s11837-015-1797-6.

[115] B. Vrancken, L. Thijs, J.-P. Kruth, J. Van Humbeeck, Heat treatment of Ti6Al4V produced by selective laser melting: microstructure and mechanical properties, J. Alloys Compd. 541 (2012) 177–185, doi:10.1016/j.jallcom.2012.07.022.

[116] G.M. Ter Haar, T.H. Becker, Low temperature stress relief and martensite decomposition in selective laser melting produced Ti6Al4V, Mater. Des. Process. Commun. (2020) 2–7, doi:10.1002/mdp2.138.

[117] C. de Formanoir, G. Martin, F. Prima, S.Y.P. Allain, T. Dessolier, F. Sun, S. Vivès, B. Hary, Y. Bréchet, S. Godet, Micromechanical behavior and thermal stability of a dual-phase α+α' titanium alloy produced by additive manufacturing, Acta Mater. 162 (2019) 149–162, doi:10.1016/j.actamat.2018.09.050.

[118] A. Yadollahi, N. Shamsaei, S.M. Thompson, D.W. Seely, Effects of process time interval and heat treatment on the mechanical and microstructural properties of direct laser deposited 316L stainless steel, Mater. Sci. Eng. A 644 (2015) 171–183, doi:10.1016/j.msea.2015.07.056.

[119] T. Ishimoto, S. Wu, Y. Ito, S.-H. Sun, H. Amano, T. Nakano, Crystallographic orientation control of 316L austenitic stainless steel via selective laser melting, ISIJ Int. 60 (2020) 1758–1764, doi:10.2355/isijinternational.ISIJINT-2019-744.

[120] A.T. Polonsky, W.C. Lenthe, M.P. Echlin, V. Livescu, G.T. Gray, T.M. Pollock, Solidification-driven orientation gradients in additively manufactured stainless steel, Acta Mater. 183 (2020) 249–260, doi:10.1016/j.actamat.2019.10.047.

[121] Z. Zhu, W. Li, Q.B. Nguyen, X. An, W. Lu, Z. Li, F.L. Ng, S.M. Ling Nai, J. Wei, Enhanced strength–ductility synergy and transformation-induced plasticity of the selective laser fabricated 304L stainless steel, Addit. Manuf. 35 (2020) 101300, doi:10.1016/j.addma.2020.101300.

[122] Z. Sun, X. Tan, S.B. Tor, C.K. Chua, Simultaneously enhanced strength and ductility for 3D-printed stainless steel 316L by selective laser melting, NPG Asia Mater. 10 (2018) 127–136, doi:10.1038/s41427-018-0018-5.

[123] A. Aversa, A. Saboori, E. Librera, M. de Chirico, S. Biamino, M. Lombardi, P. Fino, The role of directed energy deposition atmosphere mode on the microstructure and mechanical properties of 316L samples, Addit. Manuf. 34 (2020) 101274, doi:10.1016/j.addma.2020.101274.

[124] K. Abd-Elghany, D.L. Bourell, Property evaluation of 304L stainless steel fabricated by selective laser melting, Rapid Prototyp. J. 18 (2012) 420–428, doi:10.1108/13552541211250418.

[125] J. Gordon, J. Hochhalter, C. Haden, D.G. Harlow, Enhancement in fatigue performance of metastable austenitic stainless steel through directed energy deposition additive manufacturing, Mater. Des. 168 (2019) 107630, doi:10.1016/j.matdes.2019.107630.

[126] M.S. Pham, B. Dovgyy, P.A. Hooper, Twinning induced plasticity in austenitic stainless steel 316L made by additive manufacturing, Mater. Sci. Eng. A 704 (2017) 102–111, doi:10.1016/j.msea.2017.07.082.

[127] J. Suryawanshi, K.G. Prashanth, U. Ramamurty, Tensile, fracture, and fatigue crack growth properties of a 3D printed maraging steel through selective laser melting, J. Alloys Compd. 725 (2017) 355–364, doi:10.1016/j.jallcom.2017.07.177.

[128] J. Damon, T. Hanemann, S. Dietrich, G. Graf, K.H. Lang, V. Schulze, Orientation dependent fatigue performance and mechanisms of selective laser melted maraging steel X3NiCoMoTi18-9-5, Int. J. Fatigue 127 (2019) 395–402, doi:10.1016/j.ijfatigue.2019.06.025.

[129] E.A. Jägle, P.-P. Choi, J. Van Humbeeck, D. Raabe, Precipitation and austenite reversion behavior of a maraging steel produced by selective laser melting, J. Mater. Res. 29 (2014) 2072, doi:10.1557/jmr.2014.204.

[130] E.A. Jägle, Z. Sheng, P. Kürnsteiner, S. Ocylok, A. Weisheit, D. Raabe, Comparison of maraging steel micro- and nanostructure produced conventionally and by laser additive manufacturing, Materials 10 (2017), doi:10.3390/ma10010008.

[131] B. Mooney, K.I. Kourousis, A review of factors affecting the mechanical properties of maraging steel 300 fabricated via laser powder bed fusion, Metals 10 (2020) 1–22. 10.3390/met10091273.

[132] B. Wang, P. Zhang, Q.Q. Duan, Z.J. Zhang, H.J. Yang, X.W. Li, Z.F. Zhang, Optimizing the fatigue strength of 18Ni maraging steel through ageing treatment, Mater. Sci. Eng. A 707 (2017) 674–688, doi:10.1016/j.msea.2017.09.107.

[133] H. Gong, J.J.S. Dilip, L. Yang, C. Teng, B. Stucker, Influence of small particles inclusion on selective laser melting of Ti-6Al-4V powder, Conf. Ser.: Mater. Sci. Eng. 272 (2020), doi:10.1088/1757-899X/272/1/012024.

[134] A. Yadollahi, N. Shamsaei, S.M. Thompson, A. Elwany, L. Bian, Effects of building orientation and heat treatment on fatigue behavior of selective laser melted 17-4 PH stainless steel, Int. J. Fatigue 94 (2017) 218–235, doi:10.1016/j.ijfatigue.2016.03.014.

[135] E. Lu, A. Palazotto, A. Dempsey, R. Abraham, Analysis of the effects of additive manufacturing on the material properties of 15-5PH stainless steel, in: 58th AIAA/ASCE/AHS/ASC Structures, Structural Dynamics, and Materials Conference 2017, 2017, pp. 1–13, doi:10.2514/6.2017-1142.

[136] S. Sarkar, C.S. Kumar, A.K. Nath, Effects of heat treatment and build orientations on the fatigue life of selective laser melted 15-5 PH stainless steel, Mater. Sci. Eng. A 755 (2019) 235–245, doi:10.1016/j.msea.2019.04.003.

[137] H.K. Rafi, D. Pal, N. Patil, T.L. Starr, B.E. Stucker, Microstructure and mechanical behavior of 17-4 precipitation hardenable steel processed by selective laser melting, J. Mater. Eng. Perform. 23 (2014) 4421–4428, doi:10.1007/s11665-014-1226-y.

[138] A. Yadollahi, M. Mahmoudi, A. Elwany, H. Doude, L. Bian, J.C. Newman, Effects of crack orientation and heat treatment on fatigue-crack-growth behavior of AM 17-4 PH stainless steel, Eng. Fract. Mech. 226 (2020) 106874, doi:10.1016/j.engfracmech.2020.106874.

[139] S.D. Meredith, J.S. Zuback, J.S. Keist, T.A. Palmer, Impact of composition on the heat treatment response of additively manufactured 17–4 PH grade stainless steel, Mater. Sci. Eng. A 738 (2018) 44–56, doi:10.1016/j.msea.2018.09.066.

[140] T.G. Gallmeyer, S. Moorthy, B.B. Kappes, M.J. Mills, B. Amin-Ahmadi, A.P. Stebner, Knowledge of process-structure-property relationships to engineer better heat treatments for laser powder bed fusion additive manufactured Inconel 718, Addit. Manuf. 31 (2020) 100977, doi:10.1016/j.addma.2019.100977.

[141] B. Graybill, D. Malawey, E. Martinez-franco, Additive manufacturing of nickel-based superalloys, in: ASME 2018 13th International Manufacturing Science and Engineering Conference, 2018, pp. 1–17.

[142] D. Ma, A.D. Stoica, Z. Wang, A.M. Beese, Crystallographic texture in an additively manufactured nickel-base superalloy, Mater. Sci. Eng. A 684 (2017) 47–53, doi:10.1016/j.msea.2016.12.028.

[143] V.A. Popovich, E.V. Borisov, A.A. Popovich, V.S. Sufiiarov, D.V. Masaylo, L. Alzina, Functionally graded Inconel 718 processed by additive manufacturing: crystallographic texture, anisotropy of microstructure and mechanical properties, Mater. Des. 114 (2017) 441–449, doi:10.1016/j.matdes.2016.10.075.

[144] M.R. Gotterbarm, M. Seifi, D. Melzer, J. Džugan, A.A. Salem, Z.H. Liu, C. Körner, Small scale testing of IN718 single crystals manufactured by EB-PBF, Addit. Manuf. 36 (2020) 101449, doi:10.1016/j.addma.2020.101449.

[145] H. Helmer, A. Bauereiß, R.F. Singer, C. Körner, Grain structure evolution in Inconel 718 during selective electron beam melting, Mater. Sci. Eng. A 668 (2016) 180–187, doi:10.1016/j.msea.2016.05.046.

[146] M.R. Gotterbarm, A.M. Rausch, C. Körner, Fabrication of single crystals through a μ-helix grain selection process during electron beam metal additive manufacturing, Metals 10 (2020), doi:10.3390/met10030313.

[147] M. Ni, C. Chen, X. Wang, P. Wang, R. Li, X. Zhang, K. Zhou, Anisotropic tensile behavior of in situ precipitation strengthened Inconel 718 fabricated by additive manufacturing, Mater. Sci. Eng. A 701 (2017) 344–351, doi:10.1016/j.msea.2017.06.098.

[148] K.N. Amato, S.M. Gaytan, L.E. Murr, E. Martinez, P.W. Shindo, J. Hernandez, S. Collins, F. Medina, Microstructures and mechanical behavior of Inconel 718 fabricated by selective laser melting, Acta Mater. 60 (2012) 2229–2239, doi:10.1016/j.actamat.2011.12.032.

[149] S. Sui, J. Chen, E. Fan, H. Yang, X. Lin, W. Huang, The influence of Laves phases on the high-cycle fatigue behavior of laser additive manufactured Inconel 718, Mater. Sci. Eng. A 695 (2017) 6–13, doi:10.1016/j.msea.2017.03.098.

[150] R.G. Ding, Z.W. Huang, H.Y. Li, I. Mitchell, G. Baxter, P. Bowen, Electron microscopy study of direct laser deposited IN718, Mater. Charact. 106 (2015) 324–337, doi:10.1016/j.matchar.2015.06.017.

[151] Y. Cao, P. Bai, F. Liu, X. Hou, Y. Guo, Effect of the solution temperature on the precipitates and grain evolution of IN718 fabricated by laser additive manufacturing, Materials 13 (2020), doi:10.3390/ma13020340.

[152] Y.L. Kuo, S. Horikawa, K. Kakehi, The effect of interdendritic δ phase on the mechanical properties of Alloy 718 built up by additive manufacturing, Mater. Des. 116 (2017) 411–418, doi:10.1016/j.matdes.2016.12.026.

[153] X. Yu, X. Lin, F. Liu, L. Wang, Y. Tang, J. Li, S. Zhang, W. Huang, Influence of post-heat-treatment on the microstructure and fracture toughness properties of Inconel 718 fabricated with laser directed energy deposition additive manufacturing, Mater. Sci. Eng. A 798 (2020) 140092, doi:10.1016/j.msea.2020.140092.

[154] J. Wu, X.Q. Wang, W. Wang, M.M. Attallah, M.H. Loretto, Microstructure and strength of selectively laser melted AlSi10Mg, Acta Mater. 117 (2016) 311–320, doi:10.1016/j.actamat.2016.07.012.

[155] M.J. Paul, Q. Liu, J.P. Best, X. Li, J.J. Kruzic, U. Ramamurty, B. Gludovatz, Fracture resistance of AlSi10Mg fabricated by laser powder bed fusion, Acta Mater. (2021) 116869, doi:10.1016/j.actamat.2021.116869.

[156] C. Zhang, H. Zhu, H. Liao, Y. Cheng, Z. Hu, X. Zeng, Effect of heat treatments on fatigue property of selective laser melting AlSi10Mg, Int. J. Fatigue 116 (2018) 513–522, doi:10.1016/j.ijfatigue.2018.07.016.

[157] M. Fousová, D. Dvorský, A. Michalcová, D. Vojtěch, Changes in the microstructure and mechanical properties of additively manufactured AlSi10Mg alloy after exposure to elevated temperatures, Mater. Charact. 137 (2018) 119–126, doi:10.1016/j.matchar.2018.01.028.

[158] L. Zhou, A. Mehta, E. Schulz, B. McWilliams, K. Cho, Y. Sohn, Microstructure, precipitates and hardness of selectively laser melted AlSi10Mg alloy before and after heat treatment, Mater. Charact. 143 (2018) 5–17, doi:10.1016/j.matchar.2018.04.022.

[159] ASTM, ASTM E3166-20: standard guide for nondestructive examination of metal additively manufactured aerospace parts after build 1, ASTM Int. (2020) 1–63. 10.1520/E3166-20E01.1.14.

[160] J.W. Pegues, S. Shao, N. Shamsaei, N. Sanaei, A. Fatemi, D.H. Warner, P. Li, N. Phan, Fatigue of additive manufactured Ti-6Al-4V, Part I: The effects of powder feedstock, manufacturing, and post-process conditions on the resulting microstructure and defects, Int. J. Fatigue (2020) 132, doi:10.1016/j.ijfatigue.2019.105358.

[161] I. Koutiri, E. Pessard, P. Peyre, O. Amlou, T. De Terris, Influence of SLM process parameters on the surface finish, porosity rate and fatigue behavior of as-built Inconel 625 parts, J. Mater. Process. Technol. 255 (2018) 536–546, doi:10.1016/j.jmatprotec.2017.12.043.

[162] M. Fujishima, Y. Oda, R. Ashida, K. Takezawa, M. Kondo, Study on factors for pores and cladding shape in the deposition processes of Inconel 625 by the directed energy deposition (DED) method, CIRP J. Manuf. Sci. Technol. 19 (2017) 200–204, doi:10.1016/j.cirpj.2017.04.003.

[163] Z. Wang, E. Denlinger, P. Michaleris, A.D. Stoica, D. Ma, A.M. Beese, Residual stress mapping in Inconel 625 fabricated through additive manufacturing: Method for neutron diffraction measurements to validate thermomechanical model predictions, Mater. Des. 113 (2017) 169–177, doi:10.1016/j.matdes.2016.10.003.

[164] A. Mostafaei, E.L. Stevens, E.T. Hughes, S.D. Biery, C. Hilla, M. Chmielus, Powder bed binder jet printed alloy 625: densification, microstructure and mechanical properties, Mater. Des. 108 (2016) 126–135, doi:10.1016/j.matdes.2016.06.067.

[165] N. Sanaei, A. Fatemi, N. Phan, Defect characteristics and analysis of their variability in metal L-PBF additive manufacturing, Mater. Des. 182 (2019) 108091, doi:10.1016/j.matdes.2019.108091.

[166] J. Ge, T. Ma, Y. Chen, T. Jin, H. Fu, R. Xiao, Y. Lei, J. Lin, Wire-arc additive manufacturing H13 part: 3D pore distribution, microstructural evolution, and mechanical performances, J. Alloys Compd. 783 (2019) 145–155, doi:10.1016/j.jallcom.2018.12.274.

[167] Z.E. Tan, J.H.L. Pang, J. Kaminski, H. Pepin, Characterisation of porosity, density, and microstructure of directed energy deposited stainless steel AISI 316L, Addit. Manuf. 25 (2019) 286–296, doi:10.1016/j.addma.2018.11.014.

[168] P. Kumar, U. Ramamurty, High cycle fatigue in selective laser melted Ti-6Al-4V, Acta Mater. 194 (2020) 305–320, doi:10.1016/j.actamat.2020.05.041.

[169] K. Yang, Q. Huang, Q. Wang, Q. Chen, Competing crack initiation behaviors of a laser additively manufactured nickel-based superalloy in high and very high cycle fatigue regimes, Int. J. Fatigue 136 (2020) 105580, doi:10.1016/j.ijfatigue.2020.105580.

[170] X. Wang, X. He, T. Wang, Y. Li, Internal pores in DED Ti-6.5Al-2Zr-Mo-V alloy and their influence on crack initiation and fatigue life in the mid-life regime, Addit. Manuf. 28 (2019) 373–393, doi:10.1016/j.addma.2019.05.007.

[171] T.H. Becker, N.M. Dhansay, Influence of porosity on the fatigue life of laser powder bed fusion–produced Ti6Al4V, Mater. Des. Process. Commun. 3 (2021) 101396, doi:10.1002/mdp2.141.

[172] J. Günther, D. Krewerth, T. Lippmann, S. Leuders, T. Tröster, A. Weidner, H. Biermann, T. Niendorf, Fatigue life of additively manufactured Ti-6Al-4V in the very high cycle fatigue regime, Int. J. Fatigue 94 (2017) 236–245, doi:10.1016/j.ijfatigue.2016.05.018.

[173] M. Seifi, A. Salem, D. Satko, D. Shaffer, J.J. Lewandowski, Defect distribution and microstructure heterogeneity effects on fracture resistance and fatigue behavior of EBM Ti-6Al-4V, Int. J. Fatigue (2017), doi:10.1016/j.ijfatigue.2016.06.001.

[174] S. Tammas-Williams, H. Zhao, F. Léonard, F. Derguti, I. Todd, P.B. Prangnell, XCT analysis of the influence of melt strategies on defect population in Ti-6Al-4V components manufactured by selective electron beam melting, Mater. Charact. 102 (2015) 47–61, doi:10.1016/j.matchar.2015.02.008.

[175] G. Ziółkowski, E. Chlebus, P. Szymczyk, J. Kurzac, Application of X-ray CT method for discontinuity and porosity detection in 316L stainless steel parts produced with SLM technology, Arch. Civ. Mech. Eng. 14 (2014) 608–614, doi:10.1016/j.acme.2014.02.003.

[176] B. Vandenbroucke, J.P. Kruth, Selective laser melting of biocompatible metals for rapid manufacturing of medical parts, Rapid Prototyp. J. 13 (2007) 196–203, doi:10.1108/13552540710776142.

[177] S.A. Khairallah, A.T. Anderson, A. Rubenchik, W.E. King, Laser powder-bed fusion additive manufacturing: physics of complex melt flow and formation mechanisms of pores, spatter, and denudation zones, Acta Mater. 108 (2016) 36–45, doi:10.1016/j.actamat.2016.02.014.

[178] G. Strano, L. Hao, R.M. Everson, K.E. Evans, Surface roughness analysis, modelling and prediction in selective laser melting, J. Mater. Process. Technol. 213 (2013) 589–597, doi:10.1016/j.jmatprotec.2012.11.011.

[179] K.A. Mumtaz, N. Hopkinson, Selective laser melting of thin wall parts using pulse shaping, J. Mater. Process. Technol. 210 (2010) 279–287, doi:10.1016/j.jmatprotec.2009.09.011.

[180] P.A. Kobryn, E.H. Moore, S.L. Semiatin, Effect of laser power and traverse speed on microstructure, porosity, and build height in laser-deposited Ti-6Al-4V, Scr. Mater. 43 (2000) 299–305, doi:10.1016/S1359-6462(00)00408-5.

[181] P. Edwards, M. Ramulu, Fatigue performance evaluation of selective laser melted Ti-6Al-4V, Mater. Sci. Eng. A 598 (2014) 327–337, doi:10.1016/j.msea.2014.01.041.

[182] H. Gong, K. Rafi, H. Gu, G.D. Janaki Ram, T. Starr, B. Stucker, Influence of defects on mechanical properties of Ti-6Al-4V components produced by selective laser melting and electron beam melting, Mater. Des. 86 (2015) 545–554, doi:10.1016/j.matdes.2015.07.147.

[183] K.S. Chan, M. Koike, R.L. Mason, T. Okabe, Fatigue life of titanium alloys fabricated by additive layer manufacturing techniques for dental implants, Metall. Mater. Trans. A Phys. Metall. Mater. Sci. 44 (2013) 1010–1022, doi:10.1007/s11661-012-1470-4.

[184] T. Do, P. Kwon, C.S. Shin, Process development toward full-density stainless steel parts with binder jetting printing, Int. J. Mach. Tools Manuf. 121 (2017) 50–60, doi:10.1016/j.ijmachtools.2017.04.006.

[185] A. Bandyopadhyay, I. Mitra, A. Shivaram, N. Dasgupta, S. Bose, Direct comparison of additively manufactured porous titanium and tantalum implants towards in vivo osseointegration, Addit. Manuf. 28 (2019) 259–266, doi:10.1016/j.addma.2019.04.025.

[186] C.A. Kantzos, R.W. Cunningham, V. Tari, A.D. Rollett, Characterization of metal additive manufacturing surfaces using synchrotron X-ray CT and micromechanical modeling, Comput. Mech. 61 (2018) 575–580, doi:10.1007/s00466-017-1531-z.

[187] A. Fatemi, R. Molaei, S. Sharifimehr, N. Phan, N. Shamsaei, Multiaxial fatigue behavior of wrought and additive manufactured Ti-6Al-4V including surface finish effect, Int. J. Fatigue 100 (2017) 347–366, doi:10.1016/j.ijfatigue.2017.03.044.

[188] S. Beretta, M. Gargourimotlagh, S. Foletti, A. du Plessis, M. Riccio, Fatigue strength assessment of "as built" AlSi10Mg manufactured by SLM with different build orientations, Int. J. Fatigue 139 (2020) 105737, doi:10.1016/j.ijfatigue.2020.105737.

[189] P. Edwards, M. Ramulu, Effect of build direction on the fracture toughness and fatigue crack growth in selective laser melted Ti-6Al-4-‰V, Fatigue Fract. Eng. Mater. Struct. 38 (2015) 1228–1236, doi:10.1111/ffe.12303.

[190] J. Karlsson, A. Snis, H. Engqvist, J. Lausmaa, Characterization and comparison of materials produced by Electron Beam Melting (EBM) of two different Ti-6Al-4V powder fractions, J. Mater. Process. Technol. 213 (2013) 2109–2118, doi:10.1016/j.jmatprotec.2013.06.010.

[191] P. Mercelis, J.-P. Kruth, Residual stresses in selective laser sintering and selective laser melting, Rapid Prototyp. J. 12 (2006) 254–265, doi:10.1108/13552540610707013.

[192] P. Rangaswamy, T.M. Holden, R.B. Rogge, M.L. Griffith, Residual stresses in components formed by the laser-engineered net shaping (LENS®)

process, J. Strain Anal. Eng. Des. 38 (2003) 519–527, doi:10.1243/030932403770735881.

[193] I. Yadroitsev, I. Yadroitsava, Evaluation of residual stress in stainless steel 316L and Ti6Al4V samples produced by selective laser melting, Virtual Phys. Prototyp. 10 (2015) 67–76, doi:10.1080/17452759.2015.1026045.

[194] T. Mishurova, S. Cabeza, K. Artzt, J. Haubrich, M. Klaus, C. Genzel, G. Requena, G. Bruno, An assessment of subsurface residual stress analysis in SLM Ti-6Al-4V, Materials 10 (2017). 10.3390/ma10040348.

[195] L.S. Anderson, A.M. Venter, B. Vrancken, D. Marais, J. van Humbeeck, T.H. Becker, Investigating the residual stress distribution in selective laser melting produced Ti-6Al-4V using neutron diffraction, in: Mechanical Stress Evaluation by Neutron Synchrotron Radiation, 2018, pp. 73–78, doi:10.21741/9781945291678-11.

[196] B. Vrancken, V. Cain, R. Knutsen, J. Van Humbeeck, Residual stress via the contour method in compact tension specimens produced via selective laser melting, Scr. Mater. 87 (2014) 29–32, doi:10.1016/j.scriptamat.2014.05.016.

[197] T.H. Becker, N.M. Dhansay, G.M. Ter Haar, K. Vanmeensel, G.M. Ter Haar, K. Vanmeensel, Near-threshold fatigue crack growth rates of laser powder bed fusion produced Ti-6Al-4V, Acta Mater. 197 (2020) 269–282, doi:10.1016/j.actamat.2020.07.049.

[198] T. Mishurova, S. Cabeza, T. Thiede, N. Nadammal, A. Kromm, M. Klaus, C. Genzel, C. Haberland, G. Bruno, The influence of the support structure on residual stress and distortion in SLM Inconel 718 parts, Metall. Mater. Trans. A 49 (2018) 3038–3046, doi:10.1007/s11661-018-4653-9.

[199] C.A. Brice, W.H. Hofmeister, Determination of bulk residual stresses in electron beam additive-manufactured aluminum, Metall. Mater. Trans. A 44 (2013) 5147–5153, doi:10.1007/s11661-013-1847-z.

[200] T. Gnäupel-Herold, J. Slotwinski, S. Moylan, Neutron measurements of stresses in a test artifact produced by laser-based additive manufacturing, AIP Conf. Proc. 1581 (33) (2014) 1205–1212, doi:10.1063/1.4864958.

[201] L.M. Sochalski-Kolbus, E.A. Payzant, P.A. Cornwell, T.R. Watkins, S.S. Babu, R.R. Dehoff, M. Lorenz, O. Ovchinnikova, C. Duty, Comparison of residual stresses in inconel 718 simple parts made by electron beam melting and direct laser metal sintering, Metall. Mater. Trans. A Phys. Metall. Mater. Sci. 46 (2015) 1419–1432, doi:10.1007/s11661-014-2722-2.

[202] B. Vrancken, S. Buls, J.-P. Kruth, J. Van Humbeeck, Influence of preheating and oxygen content on selective laser melting of Ti6Al4V, Proceeding of 16th RAP-DASA Conference, 2015.

[203] R. Mertens, S. Dadbakhsh, J. Van Humbeeck, J.P. Kruth, Application of base plate preheating during selective laser melting, Procedia CIRP 74 (2018) 5–11, doi:10.1016/j.procir.2018.08.002.

[204] L.N. Carter, C. Martin, P.J. Withers, M.M. Attallah, The influence of the laser scan strategy on grain structure and cracking behaviour in SLM powder-bed fabricated nickel superalloy, J. Alloys Compd. 615 (2014) 338–347, doi:10.1016/j.jallcom.2014.06.172.

[205] M.M. Attallah, R. Jennings, X. Wang, L.N. Carter, Additive manufacturing of Ni-based superalloys: the outstanding issues, MRS Bull. 41 (2016) 758–764, doi:10.1557/mrs.2016.211.

[206] B. Vrancken, R.K. Ganeriwala, M.J. Matthews, Analysis of laser-induced microcracking in tungsten under additive manufacturing conditions: experiment and simulation, Acta Mater. 194 (2020) 464–472, doi:10.1016/j.actamat.2020.04.060.

[207] T. Mukherjee, W. Zhang, T. DebRoy, An improved prediction of residual stresses and distortion in additive manufacturing, Comput. Mater. Sci. 126 (2017) 360–372, doi:10.1016/j.commatsci.2016.10.003.

[208] L.D. Bobbio, S. Qin, A. Dunbar, P. Michaleris, A.M. Beese, Characterization of the strength of support structures used in powder bed fusion additive manufacturing of Ti-6Al-4V, Addit. Manuf. 14 (2017) 60–68, doi:10.1016/j.addma.2017.01.002.

[209] L.N. Carter, M.M. Attallah, R.C. Reed, Laser Powder Bed Fabrication of nickel-base superalloys: influence of parameters; characterisation, quantification and mitigation of cracking, in: Superalloys 2012, John Wiley & Sons, Inc., Hoboken, NJ, USA, 2012, pp. 577–586, doi:10.1002/9781118516430.ch64.

[210] P. Li, D.H. Warner, J.W. Pegues, M.D. Roach, N. Shamsaei, N. Phan, Investigation of the mechanisms by which hot isostatic pressing improves the fatigue performance of powder bed fused Ti-6Al-4V, Int. J. Fatigue 120 (2019) 342–352, doi:10.1016/j.ijfatigue.2018.10.015.

[211] S. Leuders, M. Thöne, A. Riemer, T. Niendorf, T. Tröster, H.A. Richard, H.J. Maier, On the mechanical behaviour of titanium alloy TiAl6V4 manufactured by selective laser melting: Fatigue resistance and crack growth performance, Int. J. Fatigue 48 (2013) 300–307, doi:10.1016/j.ijfatigue.2012.11.011.

[212] A. du Plessis, E. Macdonald, Hot isostatic pressing in metal additive manufacturing: X-ray tomography reveals details of pore closure, Addit. Manuf. 34 (2020) 101191, doi:10.1016/j.addma.2020.101191.

[213] R. Cunningham, A. Nicolas, J. Madsen, E. Fodran, E. Anagnostou, M.D. Sangid, A.D. Rollett, Analyzing the effects of powder and post-processing on porosity and properties of electron beam melted Ti-6Al-4V, Mater. Res. Lett. 5 (2017) 516–525, doi:10.1080/21663831.2017.1340911.

[214] S. Tammas-Williams, P.J. Withers, I. Todd, P.B. Prangnell, Porosity regrowth during heat treatment of hot isostatically pressed additively manufactured titanium components, Scr. Mater. 122 (2016) 72–76, doi:10.1016/j.scriptamat.2016.05.002.

[215] A. Du Plessis, S.G. Le Roux, J. Els, G. Booysen, D.C. Blaine, Application of microCT to the non-destructive testing of an additive manufactured titanium component, Case Stud. Nondestruct. Test. Eval. 4 (2015) 1–7, doi:10.1016/j.csndt.2015.09.001.

[216] K.A. Unocic, L.M. Kolbus, R.R. Dehoff, S.N. Dryepondt, B.A. Pint, High-temperature performance of UNS N07718 processed by additive manufacturing, NACE Conference, 2014 https://www.researchgate.net/publication/276353527_High-Temperature_Performance_of_UNS_N07718_Processed_by_Additive_Manufacturing.

[217] A. Lasemi, D. Xue, P. Gu, Recent development in CNC machining of freeform surfaces: a state-of-the-art review, CAD Comput. Aided Des. 42 (2010) 641–654, doi:10.1016/j.cad.2010.04.002.

[218] S. Bagehorn, J. Wehr, H.J. Maier, Application of mechanical surface finishing processes for roughness reduction and fatigue improvement of additively manufactured Ti-6Al-4V parts, Int. J. Fatigue 102 (2017) 135–142, doi:10.1016/j.ijfatigue.2017.05.008.

[219] M. Bezuidenhout, G.M. Ter Haar, T.H. Becker, S. Rudolph, O. Damm, N. Sacks, The effect of HF-HNO3 chemical polishing on the surface roughness and fatigue life of laser powder bed fusion produced Ti6Al4V, Mater. Today Commun. 25 (2020) 101396, doi:10.1016/j.mtcomm.2020.101396.

[220] M. Benedetti, V. Fontanari, M. Bandini, F. Zanini, S. Carmignato, Low- and high-cycle fatigue resistance of Ti-6Al-4V ELI additively manufactured via selective laser melting: mean stress and defect sensitivity, Int. J. Fatigue 107 (2018) 96–109, doi:10.1016/j.ijfatigue.2017.10.021.

[221] X. Yan, S. Yin, C. Chen, R. Jenkins, R. Lupoi, R. Bolot, W. Ma, M. Kuang, H. Liao, J. Lu, M. Liu, Fatigue strength improvement of selective laser melted Ti6Al4V using ultrasonic surface mechanical attrition, Mater. Res. Lett. 7 (2019) 327–333, doi:10.1080/21663831.2019.1609110.

[222] H. Zhang, R. Chiang, H. Qin, Z. Ren, X. Hou, D. Lin, G.L. Doll, V.K. Vasudevan, Y. Dong, C. Ye, The effects of ultrasonic nanocrystal surface modification on the fatigue performance of 3D-printed Ti64, Int. J. Fatigue 103 (2017) 136–146, doi:10.1016/j.ijfatigue.2017.05.019.

[223] Y.J. Yin, J.Q. Sun, J. Guo, X.F. Kan, D.C. Yang, Mechanism of high yield strength and yield ratio of 316 L stainless steel by additive manufacturing, Mater. Sci. Eng. A 744 (2019) 773–777, doi:10.1016/j.msea.2018.12.092.

[224] W. Xu, M. Brandt, S. Sun, J. Elambasseril, Q. Liu, K. Latham, K. Xia, M. Qian, Additive manufacturing of strong and ductile Ti-6Al-4V by selective laser melting via in situ martensite decomposition, Acta Mater. 85 (2015) 74–84, doi:10.1016/j.actamat.2014.11.028.

[225] N.T. Aboulkhair, C. Tuck, I. Ashcroft, I. Maskery, N.M. Everitt, On the precipitation hardening of selective laser melted AlSi10Mg, Metall. Mater. Trans. A Phys. Metall. Mater. Sci. 46 (2015) 3337–3341, doi:10.1007/s11661-015-2980-7.

[226] H.D. Carlton, A. Haboub, G.F. Gallegos, D.Y. Parkinson, A.A. MacDowell, Damage evolution and failure mechanisms in additively manufactured stainless steel, Mater. Sci. Eng. A 651 (2016) 406–414, doi:10.1016/j.msea.2015.10.073.

[227] ASTM, ASTM F1108 standard specification for Titanium - 6 Aluminum - 4 Vanadium Alloy castings for surgical implants (UNS R56406), (2014). 10.1520/F1108-14.

[228] ASTM, ASTM F1472 standard specification for wrought Titanium-6 Aluminum-4 Vanadium Alloy for surgical implant applications, (2020). 10.1520/F1472-20A.

[229] L.E. Murr, E.V. Esquivel, S.A. Quinones, S.M. Gaytan, M.I. Lopez, E.Y. Martinez, F. Medina, D.H. Hernandez, E. Martinez, J.L. Martinez, S.W. Stafford, D.K. Brown, T. Hoppe, W. Meyers, U. Lindhe, R.B. Wicker, Microstructures and mechanical properties of electron beam-rapid manufactured Ti–6Al–4V biomedical prototypes compared to wrought Ti–6Al–4V, Mater. Charact. 60 (2009) 96–105, doi:10.1016/j.matchar.2008.07.006.

[230] G. Choi, W.S. Choi, J. Han, P.P. Choi, Additive manufacturing of titanium-base alloys with equiaxed microstructures using powder blends, Addit. Manuf. 36 (2020) 101467, doi:10.1016/j.addma.2020.101467.

[231] K. Dietrich, J. Diller, S. Dubiez-Le Goff, D. Bauer, P. Forêt, G. Witt, The influence of oxygen on the chemical composition and mechanical properties of Ti-6Al-4V during laser powder bed fusion (L-PBF), Addit. Manuf. 32 (2020), doi:10.1016/j.addma.2019.100980.

[232] O.A. Quintana, W. Tong, Effects of Oxygen content on tensile and fatigue performance of Ti-6Al-4 V manufactured by selective laser melting, JOM 69 (2017) 2693–2697, doi:10.1007/s11837-017-2590-5.

[233] L. Thijs, M.L. Montero Sistiaga, R. Wauthle, Q. Xie, J.P. Kruth, J. Van Humbeeck, Strong morphological and crystallographic texture and resulting yield strength anisotropy in selective laser melted tantalum, Acta Mater. 61 (2013) 4657–4668, doi:10.1016/j.actamat.2013.04.036.

[234] M. Tarik Hasib, H.E. Ostergaard, X. Li, J.J. Kruzic, Fatigue crack growth behavior of laser powder bed fusion additive manufactured Ti-6Al-4V: roles of post heat treatment and build orientation, Int. J. Fatigue (2020) 105955, doi:10.1016/j.ijfatigue.2020.105955.

[235] ASTM A276 /A276M-17, ASTM-A276, ASTM international, West Conshohocken, PA, 2017. 10.1520/A0276_A0276M-17.

[236] P. Guo, B. Zou, C. Huang, H. Gao, Study on microstructure, mechanical properties and machinability of efficiently additive manufactured AISI 316L stainless steel by high-power direct laser deposition, J. Mater. Process. Technol. 240 (2017) 12–22, doi:10.1016/j.jmatprotec.2016.09.005.

[237] C. Wang, X. Tan, E. Liu, S.B. Tor, Process parameter optimization and mechanical properties for additively manufactured stainless steel 316L parts by selective electron beam melting, Mater. Des. 147 (2018) 157–166, doi:10.1016/j.matdes.2018.03.035.

[238] L.E. Murr, E. Martinez, J. Hernandez, S. Collins, K.N. Amato, S.M. Gaytan, P.W. Shindo, Microstructures and properties of 17-4 PH stainless steel fabricated by selective laser melting, J. Mater. Res. Technol. 1 (2012) 167–177, doi:10.1016/S2238-7854(12)70029-7.

[239] L. Facchini, N. Vicente, I. Lonardelli, E. Magalini, P. Robotti, M. Alberto, Metastable austenite in 17-4 precipitation-hardening stainless steel produced by selective laser melting, Adv. Eng. Mater. 12 (2010) 184–188, doi:10.1002/adem.200900259.

[240] J. Nguejio, F. Szmytka, S. Hallais, A. Tanguy, S. Nardone, M.Godino Martinez, Comparison of microstructure features and mechanical properties for additive manufactured and wrought nickel alloys 625, Mater. Sci. Eng. A 764 (2019) 138214, doi:10.1016/j.msea.2019.138214.

[241] E. Chlebus, K. Gruber, B. Kuźnicka, J. Kurzac, T. Kurzynowski, Effect of heat treatment on the microstructure and mechanical properties of Inconel 718 processed by selective laser melting, Mater. Sci. Eng. A 639 (2015) 647–655, doi:10.1016/j.msea.2015.05.035.

[242] M.M. Kirka, D.A. Greeley, C. Hawkins, R.R. Dehoff, Effect of anisotropy and texture on the low cycle fatigue behavior of Inconel 718 processed via electron beam melting, Int. J. Fatigue 105 (2017) 235–243, doi:10.1016/j.ijfatigue.2017.08.021.

[243] J. Wu, X.Q. Wang, W. Wang, M.M. Attallah, M.H. Loretto, Microstructure and strength of selectively laser melted AlSi10Mg, Acta Mater. 117 (2016) 311–320, doi:10.1016/j.actamat.2016.07.012.

[244] U. Tradowsky, J. White, R.M. Ward, N. Read, W. Reimers, M.M. Attallah, Selective laser melting of AlSi10Mg: influence of post-processing on the microstructural and tensile properties development, Mater. Des. 105 (2016) 212–222, doi:10.1016/j.matdes.2016.05.066.

[245] S.R. Ch, A. Raja, P. Nadig, R. Jayaganthan, N.J. Vasa, Influence of working environment and built orientation on the tensile properties of selective laser melted AlSi10Mg alloy, Mater. Sci. Eng. A 750 (2019) 141–151, doi:10.1016/j.msea.2019.01.103.

[246] D. Buchbinder, H. Schleifenbaum, S. Heidrich, W. Meiners, J. Bültmann, High power selective laser melting (HP SLM) of aluminum parts, Phys. Procedia 12 (2011) 271–278, doi:10.1016/j.phpro.2011.03.035.

[247] K. Kempen, L. Thijs, J. Van Humbeeck, J.P. Kruth, Mechanical properties of AlSi10Mg produced by selective laser melting, Phys. Procedia 39 (2012) 439–446, doi:10.1016/j.phpro.2012.10.059.

[248] N. Read, W. Wang, K. Essa, M.M. Attallah, Selective laser melting of AlSi10Mg alloy: process optimisation and mechanical properties development, Mater. Des. 65 (2015) 417–424, doi:10.1016/j.matdes.2014.09.044.

[249] K.G. Prashanth, S. Scudino, H.J. Klauss, K.B. Surreddi, L. Löber, Z. Wang, A.K. Chaubey, U. Kühn, J. Eckert, Microstructure and mechanical properties of Al-12Si produced by selective laser melting: effect of heat treatment, Mater. Sci. Eng. A 590 (2014) 153–160, doi:10.1016/j.msea.2013.10.023.

[250] D. Manfredi, F. Calignano, M. Krishnan, R. Canali, E. Paola, S. Biamino, D. Ugues, M. Pavese, P. Fino, Additive manufacturing of Al Alloys and Aluminium Matrix Composites (AMCs), Light Met. Alloy. Appl. (2014) 15 InTech, doi:10.5772/58534.

[251] R.O. Ritchie, The conflicts between strength and toughness, Nat. Mater. 10 (2011) 817–822, doi:10.1038/nmat3115.

[252] J. Suryawanshi, K.G.G. Prashanth, S. Scudino, J. Eckert, O. Prakash, U. Ramamurty, Simultaneous enhancements of strength and toughness in an Al-12Si alloy synthesized using selective laser melting, Acta Mater. 115 (2016) 285–294, doi:10.1016/j.actamat.2016.06.009.

[253] V. Cain, L. Thijs, J. Van Humbeeck, B. Van Hooreweder, R. Knutsen, J. Van Humbeeck, B. Van Hooreweder, R. Knutsen, Crack propagation and fracture toughness of Ti6Al4V alloy produced by selective laser melting, Addit. Manuf. 5 (2015) 68–76, doi:10.1016/j.addma.2014.12.006.

[254] K.S. Ravichandran, A.K. Vasudevan, Fracture resistance of structural alloys, Fatigue Fract. 19 (2018) 381–392, doi:10.31399/asm.hb.v19.a0002379.

[255] N.M. Dhansay, Fracture Mechanics Based Fatigue and Fracture Toughness Evaluation of SLM Ti-6Al-4V, University of Cape Town, 2015.

[256] H.E. Boyer, Atlas of fatigue curves, (1985) 518. http://books.google.com.co/books?id=Hbo8dI4CqVAC&dq=AISI+SAE+4120+fatigue+resistance+curves&source=gbs_navlinks_s.

[257] P. Kumar, Z. Zhu, S.M.L. Nai, R.L. Narayan, U. Ramamurty, Fracture toughness of 304L austenitic stainless steel produced by laser powder bed fusion, Scr. Mater. 202 (2021) 114002, doi:10.1016/j.scriptamat.2021.114002.

[258] W.J. Mills, Fracture toughness of type 304 and 316 stainless steels and their welds, Int. Mater. Rev. 42 (1997) 45–82, doi:10.1179/imr.1997.42.2.45.

[259] R. Casati, J. Lemke, M. Vedani, Microstructure and Fracture behavior of 316L austenitic stainless steel produced by selective laser melting, J. Mater. Sci. Technol. 32 (2016) 738–744, doi:10.1016/j.jmst.2016.06.016.

[260] G. Puppala, A. Moitra, S. Sathyanarayanan, R. Kaul, G. Sasikala, R.C. Prasad, L.M. Kukreja, Evaluation of fracture toughness and impact toughness of laser rapid manufactured Inconel-625 structures and their co-relation, Mater. Des. 59 (2014) 509–515, doi:10.1016/j.matdes.2014.03.013.

[261] J.R. Poulin, A. Kreitcberg, P. Terriault, V. Brailovski, Long fatigue crack propagation behavior of laser powder bed-fused inconel 625 with intentionally-seeded porosity, Int. J. Fatigue 127 (2019) 144–156, doi:10.1016/j.ijfatigue.2019.06.008.

[262] M.M. Kirka, A. Plotkowski, P. Nandwana, A. Chaudhary, S.S. Babu, R.R. Dehoff, Progress in the processing and understanding of alloy 718 fabricated through powder bed additive manufacturing processes, 2018. 10.1007/978-3-319-89480-5_4.

[263] L. Hitzler, J. Hirsch, J. Schanz, B. Heine, M. Merkel, W. Hall, A. Öchsner, Fracture toughness of selective laser melted AlSi10Mg, Proc. Inst. Mech. Eng. Part L J. Mater. Des. Appl. 233 (2019) 615–621, doi:10.1177/1464420716687337.

[264] V. Drossou-Agakidou, F. Kanakoudi-Tsakalidou, K. Sarafidis, A. Taparkou, V. Tzimouli, H. Tsandali, G. Kremenopoulos, Properties and selection: nonferrous alloys and special-purpose materials, 1990. 10.1007/s004310500884.

[265] Q. Liu, H. Wu, M.J. Paul, P. He, Z. Peng, B. Gludovatz, J.J. Kruzic, C.H. Wang, X. Li, Machine-learning assisted laser powder bed fusion process optimization for AlSi10Mg: new microstructure description indices and fracture mechanisms, Acta Mater. 201 (2020) 316–328, doi:10.1016/j.actamat.2020.10.010.

[266] Y. Zhai, H. Galarraga, D.A. Lados, Microstructure, static properties, and fatigue crack growth mechanisms in Ti-6Al-4V fabricated by additive manufacturing: LENS and EBM, Eng. Fail. Anal. 69 (2016) 3–14, doi:10.1016/j.engfailanal.2016.05.036.

[267] T.H. Becker, N.M. Dhansay, G.M. Ter Haar, K. Vanmeensel, Near-threshold fatigue crack growth rates of laser powder bed fusion produced Ti-6Al-4V, Acta Mater. 197 (2020) 269–282, doi:10.2139/ssrn.3622627.

[268] V. Cain, L. Thijs, J. Van Humbeeck, B. Van Hooreweder, R. Knutsen, Crack propagation and fracture toughness of Ti6Al4V alloy produced by selective laser melting, Addit. Manuf. 5 (2015) 68–76, doi:10.1016/j.addma.2014.12.006.

[269] N. JC, P. RS, in: Fatigue Crack Growth Thresholds, Endurance Limits, and Design, ASTM International, West Conshohocken, PA, 2000, p. 19428, doi:10.1520/STP1372-EB. 2959, 100 Barr Harbor Drive, PO Box C700.

[270] N. Macallister, K. Vanmeensel, T.H. Becker, Fatigue crack growth parameters of laser powder bed fusion produced Ti-6Al-4V, Int. J. Fatigue 145 (2021) 106100, doi:10.1016/j.ijfatigue.2020.106100.

[271] A. Riemer, S. Leuders, M. Thöne, H.A. Richard, T. Tröster, T. Niendorf, On the fatigue crack growth behavior in 316L stainless steel manufactured by selective laser melting, Eng. Fract. Mech. 120 (2014) 15–25, doi:10.1016/j.engfracmech.2014.03.008.

[272] P.D. Nezhadfar, E. Burford, K. Anderson-Wedge, B. Zhang, S. Shao, S.R. Daniewicz, N. Shamsaei, Fatigue crack growth behavior of additively manufactured 17-4 PH stainless steel: effects of build orientation and microstructure, Int. J. Fatigue 123 (2019) 168–179, doi:10.1016/j.ijfatigue.2019.02.015.

[273] L. Thijs, K. Kempen, J.P. Kruth, J. Van Humbeeck, Fine-structured aluminium products with controllable texture by selective laser melting of pre-alloyed AlSi10Mg powder, Acta Mater. 61 (2013) 1809–1819, doi:10.1016/j.actamat.2012.11.052.

[274] R. Pippan, A. Hohenwarter, Fatigue crack closure: a review of the physical phenomena, Fatigue Fract. Eng. Mater. Struct. 40 (2017) 471–495, doi:10.1111/ffe.12578.

[275] R.O. Ritchie, Mechanisms of fatigue crack propagation in metals, ceramics and composites: role of crack tip shielding, Mater. Sci. Eng. 103 (1988) 15–28, doi:10.1016/0025-5416(88)90547-2.

[276] ASTM, E647–11 standard test method for measurement of fatigue crack growth rates, (2011) 1–46. 10.1520/E0647-11E01.2.

[277] Z.W. Xu, A. Liu, X.S. Wang, The influence of building direction on the fatigue crack propagation behavior of Ti6Al4V alloy produced by selective laser melting, Mater. Sci. Eng. A (2019) 767, doi:10.1016/j.msea.2019.138409.

[278] P. Ganesh, R. Kaul, C.P. Paul, P. Tiwari, S.K. Rai, R.C. Prasad, L.M. Kukreja, Fatigue and fracture toughness characteristics of laser rapid manufactured Inconel 625 structures, Mater. Sci. Eng. A 527 (2010) 7490–7497, doi:10.1016/j.msea.2010.08.034.

[279] H. Qi, M. Azer, A. Ritter, Studies of standard heat treatment effects on microstructure and mechanical properties of laser net shape manufactured INCONEL 718, Metall. Mater. Trans. A Phys. Metall. Mater. Sci. 40 (2009) 2410–2422, doi:10.1007/s11661-009-9949-3.

[280] R. Konečná, L. Kunz, G. Nicoletto, A. Bača, Long fatigue crack growth in Inconel 718 produced by selective laser melting, Int. J. Fatigue 92 (2016) 499–506, doi:10.1016/j.ijfatigue.2016.03.012.

[281] R. Konecná, L. Kunz, G. Nicoletto, A. Baca, Fatigue crack growth behavior of Inconel 718 produced by selective laser melting, Frat. Ed Integrità Strutt. 10 (2015) 31–40, doi:10.3221/IGF-ESIS.35.04.

[282] L. Xiao, D.L. Chen, M.C. Chaturvedi, Effect of boron on fatigue crack growth behavior in superalloy IN 718 at RT and 650 °C, Mater. Sci. Eng. A 428 (2006) 1–11, doi:10.1016/j.msea.2005.08.206.

[283] J. Pegues, M. Roach, R. Scott Williamson, N. Shamsaei, Surface roughness effects on the fatigue strength of additively manufactured Ti-6Al-4V, Int. J. Fatigue 116 (2018) 543–552, doi:10.1016/j.ijfatigue.2018.07.013.

[284] G. Kasperovich, J. Hausmann, Improvement of fatigue resistance and ductility of TiAl6V4 processed by selective laser melting, J. Mater. Process. Technol. 220 (2015) 202–214, doi:10.1016/j.jmatprotec.2015.01.025.

[285] H. Masuo, Y. Tanaka, S. Morokoshi, H. Yagura, T. Uchida, Y. Yamamoto, Y. Murakami, Influence of defects, surface roughness and HIP on the fatigue strength of Ti-6Al-4V manufactured by additive manufacturing, Int. J. Fatigue 117 (2018) 163–179, doi:10.1016/j.ijfatigue.2018.07.020.

[286] S. Kikuchi, S. Heinz, D. Eifler, Y. Nakamura, A. Ueno, Evaluation of very high cycle fatigue properties of low temperature nitrided Ti-6Al-4V alloy using ultrasonic testing technology, Key Eng. Mater. 664 (2016) 118–127, doi:10.4028/www.scientific.net/KEM.664.118.

[287] I. Walter, L.A. Imig, Fatigue of four stainless steels, four titanium alloys, and two aluminum alloys before and after exposure to elevated temperatures for up to three years, 1971.

[288] W. Eric, E. Claus, S. Shafaqat, W. Frank, High cycle fatigue (HCF) performance of Ti-6Al-4V alloy processed by selective laser melting, Adv. Mater. Res. (2013) 134–139, doi:10.4028/www.scientific.net/AMR.816-817.134.

[289] E. Wycisk, A. Solbach, S. Siddique, D. Herzog, F. Walther, C. Emmelmann, Effects of defects in laser additive manufactured Ti-6Al-4V on fatigue properties, Phys. Procedia 56 (2014) 371–378, doi:10.1016/j.phpro.2014.08.120.

[290] K. Mertova, J. Dzugan, M. Roudnicka, Fatigue properties of SLM-produced Ti6Al4V with various post-processing processes, IOP Conf. Ser. Mater. Sci. Eng. 461 (2018), doi:10.1088/1757-899X/461/1/012052.

[291] L. Lan, X. Jin, S. Gao, B. He, Y. Rong, Microstructural evolution and stress state related to mechanical properties of electron beam melted Ti-6Al-4V alloy modified by laser shock peening, J. Mater. Sci. Technol. 50 (2020) 153–161, doi:10.1016/j.jmst.2019.11.039.

[292] S. Beretta, S. Romano, A comparison of fatigue strength sensitivity to defects for materials manufactured by AM or traditional processes, Int. J. Fatigue 94 (2017) 178–191, doi:10.1016/j.ijfatigue.2016.06.020.

[293] S. Romano, P.D. Nezhadfar, N. Shamsaei, M. Seifi, S. Beretta, High cycle fatigue behavior and life prediction for additively manufactured 17-4 PH stainless steel: effect of sub-surface porosity and surface roughness, Theor. Appl. Fract. Mech. 106 (2020), doi:10.1016/j.tafmec.2020.102477.

[294] U. Zerbst, G. Bruno, J.Y. Buffière, T. Wegener, T. Niendorf, T. Wu, X. Zhang, N. Kashaev, G. Meneghetti, N. Hrabe, M. Madia, T. Werner, K. Hilgenberg, M. Koukolíková, R. Procházka, J. Džugan, B. Möller, S. Beretta, A. Evans, R. Wagener, K. Schnabel, Damage tolerant design of additively manufactured metallic components subjected to cyclic loading: state of the art and challenges, Prog. Mater. Sci. (2021) 1–73, doi:10.1016/j.pmatsci.2021.100786.

[295] A.B. Spierings, T.L. Starr, K. Wegener, Fatigue performance of additive manufactured metallic parts, Rapid Prototyp. J. 19 (2013) 88–94, doi:10.1108/13552541311302932.

[296] E. Uhlmann, C. Fleck, G. Gerlitzky, F. Faltin, Dynamical fatigue behavior of additive manufactured products for a fundamental life cycle approach, Procedia CIRP 61 (2017) 588–593, doi:10.1016/j.procir.2016.11.138.

[297] C. Yu, Y. Zhong, P. Zhang, Z. Zhang, C. Zhao, Z. Zhang, Z. Shen, W. Liu, Effect of build direction on fatigue performance of L-PBF 316L stainless steel, Acta Metall. Sin. (Engl. Lett.) 33 (2020) 539–550, doi:10.1007/s40195-019-00983-3.

[298] T.M. Mower, M.J. Long, Mechanical behavior of additive manufactured, powder-bed laser-fused materials, Mater. Sci. Eng. A 651 (2016) 198–213, doi:10.1016/j.msea.2015.10.068.

[299] B. Voloskov, S. Evlashin, S. Dagesyan, S. Abaimov, I. Akhatov, I. Sergeichev, Very high cycle fatigue behavior of additively manufactured 316L stainless steel, Materials 13 (2020) 1–11, doi:10.3390/ma13153293.

[300] P. Wood, T. Libura, Z.L. Kowalewski, G. Williams, A. Serjouei, Influences of horizontal and vertical build orientations and post-fabrication processes on the fatigue behavior of stainless steel 316L produced by selective laser melting, Materials 12 (2019) 4203, doi:10.3390/ma12244203.

[301] S. Lee, J.W. Pegues, N. Shamsaei, Fatigue behavior and modeling for additive manufactured 304L stainless steel: the effect of surface roughness, Int. J. Fatigue 141 (2020) 105856, doi:10.1016/j.ijfatigue.2020.105856.

[302] M.M. Parvez, T. Pan, Y. Chen, S. Karnati, J.W. Newkirk, F. Liou, High cycle fatigue performance of lpbf 304l stainless steel at nominal and optimized parameters, Materials 13 (2020) 1–15, doi:10.3390/ma13071591.

[303] P.D. Nezhadfar, R. Shrestha, N. Phan, N. Shamsaei, Fatigue behavior of additively manufactured 17-4 PH stainless steel: synergistic effects of surface roughness and heat treatment, Int. J. Fatigue 124 (2019) 188–204, doi:10.1016/j.ijfatigue.2019.02.039.

[304] D. Rigon, G. Meneghetti, An engineering estimation of fatigue thresholds from a microstructural size and Vickers hardness: application to wrought and additively manufactured metals, Int. J. Fatigue (2020) 139, doi:10.1016/j.ijfatigue.2020.105796.

[305] K. Solberg, F. Berto, The effect of defects and notches in quasi-static and fatigue loading of Inconel 718 specimens produced by selective laser melting, Int. J. Fatigue 137 (2020) 105637, doi:10.1016/j.ijfatigue.2020.105637.

[306] D.B. Witkin, D. Patel, T.V. Albright, G.E. Bean, T. McLouth, Influence of surface conditions and specimen orientation on high cycle fatigue properties of Inconel 718 prepared by laser powder bed fusion, Int. J. Fatigue 132 (2020) 105392, doi:10.1016/j.ijfatigue.2019.105392.

[307] Y. Yamashita, T. Murakami, R. Mihara, M. Okada, Y. Murakami, Defect analysis and fatigue design basis for Ni-based superalloy 718 manufactured by selective laser melting, Int. J. Fatigue 117 (2018) 485–495, doi:10.1016/j.ijfatigue.2018.08.002.

[308] S. Gribbin, S. Ghorbanpour, N.C. Ferreri, J. Bicknell, I. Tsukrov, M. Knezevic, Role of grain structure, grain boundaries, crystallographic texture, precipitates, and porosity on fatigue behavior of Inconel 718 at room and elevated temperatures, Mater. Charact. 149 (2019) 184–197, doi:10.1016/j.matchar.2019.01.028.

[309] W. Li, R. Sun, P. Wang, X.L. Li, Y. Zhang, T. Hu, C. Li, T. Sakai, Subsurface faceted cracking behavior of selective laser melting Ni-based superalloy under very high cycle fatigue, Scr. Mater. 194 (2021) 0–5, doi:10.1016/j.scriptamat.2020.11.001.

[310] M.M. Kirka, F. Medina, R. Dehoff, A. Okello, Mechanical behavior of postprocessed Inconel 718 manufactured through the electron beam melting process, Mater. Sci. Eng. A 680 (2017) 338–346, doi:10.1016/j.msea.2016.10.069.

[311] M.J. Donachie, Titanium: A Technical Guide, 2nd Edition, ASM International, 2000, doi:10.1016/j.scriptamat.2006.08.010.

[312] M.M. Kirka, D.A.A. Greeley, C. Hawkins, R.R.R. Dehoff, Effect of anisotropy and texture on the low cycle fatigue behavior of Inconel 718 processed via electron beam melting, Int. J. Fatigue 105 (2017) 235–243, doi:10.1016/j.ijfatigue.2017.08.021.

[313] N.E. Uzan, R. Shneck, O. Yeheskel, N. Frage, Fatigue of AlSi10Mg specimens fabricated by additive manufacturing selective laser melting (AM-SLM), Mater. Sci. Eng. A 704 (2017) 229–237, doi:10.1016/j.msea.2017.08.027.

[314] E. Beevers, A.D. Brandão, J. Gumpinger, M. Gschweitl, C. Seyfert, P. Hofbauer, T. Rohr, T. Ghidini, Fatigue properties and material characteristics of additively manufactured AlSi10Mg – Effect of the contour parameter on the microstructure, density, residual stress, roughness and mechanical properties, Int. J. Fatigue 117 (2018) 148–162, doi:10.1016/j.ijfatigue.2018.08.023.

[315] N.E. Uzan, S. Ramati, R. Shneck, N. Frage, O. Yeheskel, On the effect of shot-peening on fatigue resistance of AlSi10Mg specimens fabricated by additive manufacturing using selective laser melting (AM-SLM), Addit. Manuf. 21 (2018) 458–464, doi:10.1016/j.addma.2018.03.030.

[316] M. Donachie, Titanium A Technical Guide, 2nd ed., 2000 Ohio http://books.google.com/books?hl=en&lr=&id=HgzukknbNGAC&oi=fnd&pg=PR7&dq=Titanium+A+Technical+Guide&ots=K_51iicC1J&sig=rGiGidXw5ZyO1W45EG05Bkhzmy0 (accessed September 19, 2013).

[317] H.K. Rafi, N.V. Karthik, H. Gong, T.L. Starr, B.E. Stucker, Microstructures and mechanical properties of Ti6Al4V parts fabricated by selective laser melting and electron beam melting, J. Mater. Eng. Perform. (2013) doi:10.1007/s11665-013-0658-0.

[318] E. Wycisk, S. Siddique, D. Herzog, F. Walther, C. Emmelmann, Fatigue performance of laser additive manufactured Ti–6Al–4V in very high cycle fatigue regime up to 10 9 cycles, Front. Mater. 2 (2015) 72, doi:10.3389/fmats.2015.00072.

[319] J.B. Gao, X.L. Zhao, J.K. Yue, M.C. Qi, D.L. Zhang, Microstructure and mechanical properties of Ti-6Al-4V alloy samples fabricated by selective laser melting, Key Eng. Mater. 770 (2018) 179–186, doi:10.4028/www.scientific.net/KEM.770.179.

[320] X. Tan, Y. Kok, Y.J. Tan, M. Descoins, D. Mangelinck, S.B. Tor, K.F. Leong, C.K. Chua, Graded microstructure and mechanical properties of additive manufactured Ti-6Al-4V via electron beam melting, Acta Mater. 97 (2015) 1–16, doi:10.1016/j.actamat.2015.06.036.

[321] P. Edwards, A. O'Conner, M. Ramulu, Electron beam additive manufacturing of titanium components: properties and performance, J. Manuf. Sci. Eng. Trans. ASME 135 (2013), doi:10.1115/1.4025773.

[322] H. Galarraga, R.J. Warren, D.A. Lados, R.R. Dehoff, M.M. Kirka, P. Nandwana, Effects of heat treatments on microstructure and properties of Ti-6Al-4V ELI alloy fabricated by electron beam melting (EBM), Mater. Sci. Eng. A 685 (2017) 417–428, doi:10.1016/j.msea.2017.01.019.

[323] Y. Zhai, H. Galarraga, D.A. Lados, Microstructure evolution, tensile properties, and fatigue damage mechanisms in Ti-6Al-4V alloys fabricated by two additive manufacturing techniques, Procedia Eng. (2015) doi:10.1016/j.proeng.2015.08.007.

[324] B.E. Carroll, T.A. Palmer, A.M. Beese, Anisotropic tensile behavior of Ti–6Al–4V components fabricated with directed energy deposition additive manufacturing, Acta Mater. 87 (2015) 309–320, doi:10.1016/j.actamat.2014.12.054.

[325] J. Yu, M. Rombouts, G. Maes, F. Motmans, Material properties of Ti6Al4V parts produced by laser metal deposition, Phys. Procedia 39 (2012) 416–424, doi:10.1016/j.phpro.2012.10.056.

[326] E. Liverani, S. Toschi, L. Ceschini, A. Fortunato, Effect of selective laser melting (SLM) process parameters on microstructure and mechanical properties of 316L austenitic stainless steel, J. Mater. Process. Technol. 249 (2017) 255–263, doi:10.1016/j.jmatprotec.2017.05.042.

[327] N.P. Lavery, J. Cherry, S. Mehmood, H. Davies, B. Girling, E. Sackett, S.G.R. Brown, J. Sienz, Effects of hot isostatic pressing on the elastic modulus and tensile properties of 316L parts made by powder bed laser fusion, Mater. Sci. Eng. A 693 (2017) 186–213, doi:10.1016/j.msea.2017.03.100.

[328] D.K. Kim, W. Woo, E.Y. Kim, S.H. Choi, Microstructure and mechanical characteristics of multi-layered materials composed of 316L stainless steel and ferritic steel produced by direct energy deposition, J. Alloys Compd. 774 (2019) 896–907, doi:10.1016/j.jallcom.2018.09.390.

[329] M. Ghayoor, K. Lee, Y. He, C. hung Chang, B.K. Paul, S. Pasebani, Selective laser melting of 304L stainless steel: role of volumetric energy density on the microstructure, texture and mechanical properties, Addit. Manuf. 32 (2020) 101011, doi:10.1016/j.addma.2019.101011.

[330] K. Guan, Z. Wang, M. Gao, X. Li, X. Zeng, Effects of processing parameters on tensile properties of selective laser melted 304 stainless steel, Mater. Des. 50 (2013) 581–586, doi:10.1016/j.matdes.2013.03.056.

[331] a276Standard Specification for Stainless Steel Bars and Shapes, ASTM International, West Conshohocken, PA, 2012, doi:10.1520/A0276-10.2.

[332] T. LeBrun, T. Nakamoto, K. Horikawa, H. Kobayashi, Effect of retained austenite on subsequent thermal processing and resultant mechanical properties of selective laser melted 17-4 PH stainless steel, Mater. Des. 81 (2015) 44–53, doi:10.1016/j.matdes.2015.05.026.

[333] J. Vishwakarma, K. Chattopadhyay, N.C. Santhi Srinivas, Effect of build orientation on microstructure and tensile behaviour of selectively laser melted M300 maraging steel, Mater. Sci. Eng. A 798 (2020) 140130, doi:10.1016/j.msea.2020.140130.

[334] C. Tan, K. Zhou, W. Ma, P. Zhang, M. Liu, T. Kuang, Microstructural evolution, nanoprecipitation behavior and mechanical properties of selective laser melted high-performance grade 300 maraging steel, Mater. Des. 134 (2017) 23–34, doi:10.1016/j.matdes.2017.08.026.

[335] R. Casati, J.N. Lemke, A. Tuissi, M. Vedani, Aging behaviour and mechanical performance of 18-Ni 300 steel processed by selective laser melting, Metals 6 (2016) 218, doi:10.3390/met6090218.

[336] T.H. Becker, D. Dimitrov, The achievable mechanical properties of SLM produced maraging steel 300 components, Rapid Prototyp. J. 22 (2016) 487–494, doi:10.1108/RPJ-08-2014-0096.

[337] K. Kempen, E. Yasa, L. Thijs, J.P. Kruth, J. Van Humbeeck, Microstructure and mechanical properties of selective laser melted 18Ni-300 steel, Phys. Procedia 12 (2011) 255–263, doi:10.1016/j.phpro.2011.03.033.

[338] Y. Yao, Y. Huang, B. Chen, C. Tan, Y. Su, J. Feng, Influence of processing parameters and heat treatment on the mechanical properties of 18Ni300 manufactured by laser based directed energy deposition, Opt. Laser Technol. 105 (2018) 171–179, doi:10.1016/j.optlastec.2018.03.011.

[339] S. Etris, Y. Fiorini, K. Lieb, I. Moore, A. Batik, C. Brinkman, G. Korth, Strain fatigue and tensile behavior of Inconel® 718 from room temperature to 650℃, J. Test. Eval. 2 (1974) 249, doi:10.1520/JTE10109J.

[340] Z. Wang, K. Guan, M. Gao, X. Li, X. Chen, X. Zeng, The microstructure and mechanical properties of deposited-IN718 by selective laser melting, J. Alloys Compd. 513 (2012) 518–523, doi:10.1016/j.jallcom.2011.10.107.

[341] M.M. Kirka, F. Medina, R. Dehoff, A. Okello, Mechanical behavior of post-processed Inconel 718 manufactured through the electron beam melting process, Mater. Sci. Eng. A 680 (2017) 338–346, doi:10.1016/j.msea.2016.10.069.

[342] F. Liu, F. Lyu, F. Liu, X. Lin, C. Huang, Laves phase control of inconel 718 superalloy fabricated by laser direct energy deposition via δ aging and solution treatment, J. Mater. Res. Technol. 9 (2020) 9753–9765, doi:10.1016/j.jmrt.2020.06.061.

[343] K.S. Kim, T.H. Kang, M.E. Kassner, K.T. Son, K.A. Lee, High-temperature tensile and high cycle fatigue properties of inconel 625 alloy manufactured by laser powder bed fusion, Addit. Manuf. 35 (2020) 101377, doi:10.1016/j.addma.2020.101377.

[344] L.E. Murr, E. Martinez, S.M. Gaytan, D.A. Ramirez, B.I. MacHado, P.W. Shindo, J.L. Martinez, F. Medina, J. Wooten, D. Ciscel, U. Ackelid, R.B. Wicker, Microstructural architecture, microstructures, and mechanical properties for a nickel-base superalloy fabricated by electron beam melting, Metall. Mater. Trans. A Phys. Metall. Mater. Sci. 42 (2011) 3491–3508, doi:10.1007/s11661-011-0748-2.

[345] A. Mostafaei, Y. Behnamian, Y.L. Krimer, E.L. Stevens, J.L. Luo, M. Chmielus, Effect of solutionizing and aging on the microstructure and mechanical properties of powder bed binder jet printed nickel-based superalloy 625, Mater. Des. 111 (2016) 482–491, doi:10.1016/j.matdes.2016.08.083.

[346] N. EN1706, Aluminium and aluminium alloys—castings—chemical composition and mechanical properties, Association Française de Normalisation. French Standardization Association No. NF EN. 1706 (2010) 2010.

[347] S.A. Jawade, R.S. Joshi, S.B. Desai, Comparative study of mechanical properties of additively manufactured aluminum alloy, Mater. Today Proc. (2020), doi:10.1016/j.matpr.2020.02.096.

[348] A. Iliopoulos, R. Jones, J. Michopoulos, N. Phan, R. Singh Raman, Crack growth in a range of additively manufactured aerospace structural materials, Aerospace 5 (2018) 118, doi:10.3390/aerospace5040118.

[349] M. Lapalme, É. Thibault, G. Rousseau, Comparison of mechanical properties of additively manufactured Ti-6Al-4V alloy made using different manufacturing processes, Annual Forum Proceeding - AHS International, AHS International, 2018.

[350] D. Greitemeier, F. Palm, F. Syassen, T. Melz, Fatigue performance of additive manufactured TiAl6V4 using electron and laser beam melting, Int. J. Fatigue 94 (2017) 211–217, doi:10.1016/j.ijfatigue.2016.05.001.

[351] T.H. Becker, M. Beck, C. Scheffer, Microstructure and mechanical properties of direct metal laser sintered Ti-6Al-4V, S. Afr. J. Ind. Eng. 26 (2015) 1–10.

[352] E. Wycisk, A. Solbach, S. Siddique, D. Herzog, F. Walther, C. Emmelmann, Effects of defects in laser additive manufactured Ti-6Al-4V on fatigue properties, Phys. Procedia (2014) 371–378, doi:10.1016/j.phpro.2014.08.120.

[353] B. Van Hooreweder, D. Moens, R. Boonen, J.-P. Kruth, P. Sas, Analysis of fracture toughness and crack propagation of Ti6Al4V produced by selective laser melting, Adv. Eng. Mater. 14 (2012) 92–97, doi:10.1002/adem.201100233.

[354] H. Galarraga, R.J. Warren, D.A. Lados, R.R. Dehoff, M.M. Kirka, Fatigue crack growth mechanisms at the microstructure scale in as-fabricated and heat treated Ti-6Al-4V ELI manufactured by electron beam melting (EBM), Eng. Fract. Mech. 176 (2017) 263–280, doi:10.1016/j.engfracmech.2017.03.024.

[355] M. Seifi, M. Dahar, R. Aman, O. Harrysson, J. Beuth, J.J. Lewandowski, Evaluation of orientation dependence of fracture toughness and fatigue crack propagation behavior of As-deposited ARCAM EBM Ti-6Al-4V, JOM 67 (2015) 597–607, doi:10.1007/s11837-015-1298-7.

[356] L.M.S. Santos, L.P. Borrego, J.A.M. Ferreira, J. de Jesus, J.D. Costa, C. Capela, Effect of heat treatment on the fatigue crack growth behaviour in additive manufactured AISI 18Ni300 steel, Theor. Appl. Fract. Mech. 102 (2019) 10–15, doi:10.1016/j.tafmec.2019.04.005.

[357] H.J. Rack, D. Kalish, Strength, fracture toughness, and low cycle fatigue behavior of 17-4 PH stainless steel, Met. Trans. 5 (1974) 1595–1605, doi:10.1007/BF02646331.

[358] X. Hu, Z. Xue, T.T. Ren, Y. Jiang, C.L. Dong, F. Liu, On the fatigue crack growth behaviour of selective laser melting fabricated Inconel 625: effects of build orientation and stress ratio, Fatigue Fract. Eng. Mater. Struct. 43 (2020) 771–787, doi:10.1111/ffe.13181.

[359] X. Yu, X. Lin, F. Liu, Y. Hu, S. Zhang, Y. Zhan, H. Yang, W. Huang, Microstructure and fatigue crack growth behavior of inconel 718 superalloy fabricated via laser directed energy deposition additive manufacturing, SSRN Electron. J. (2020), doi:10.2139/ssrn.3614841.

[360] N. Mfusi, L. Mathe, Popoola Tshabalala, The effect of stress relief on the mechanical and fatigue properties of additively manufactured AlSi10Mg parts, Metals 9 (2019) 1216, doi:10.3390/met9111216.

[361] N.E. Uzan, R. Shneck, O. Yeheskel, N. Frage, Fatigue of AlSi10Mg specimens fabricated by additive manufacturing selective laser melting (AM-SLM), Mater. Sci. Eng. A 704 (2017) 229–237, doi:10.1016/j.msea.2017.08.027.

[362] J. Günther, D. Krewerth, T. Lippmann, S. Leuders, T. Tröster, A. Weidner, H. Biermann, T. Niendorf, Fatigue life of additively manufactured Ti–6Al–4V in the very high cycle fatigue regime, Int. J. Fatigue 94 (2017) 236–245, doi:10.1016/j.ijfatigue.2016.05.018.

[363] H. Soyama, Y. Okura, The use of various peening methods to improve the fatigue strength of titanium alloy Ti6Al4V manufactured by electron beam melting, AIMS Mater. Sci. 5 (2018) 1000–1015, doi:10.3934/MATERSCI.2018.5.1000.

[364] P. Kumar, R. Jayaraj, J. Suryawanshi, U.R.R. Satwik, J. McKinnell, U. Ramamurty, Fatigue strength of additively manufactured 316L austenitic stainless steel, Acta Mater. 199 (2020) 225–239, doi:10.1016/j.actamat.2020.08.033.

[365] C. Elangeswaran, A. Cutolo, G.K. Muralidharan, C. de Formanoir, F. Berto, K. Vanmeensel, B. Van Hooreweder, Effect of post-treatments on the fatigue behaviour of 316L stainless steel manufactured by laser powder bed fusion, Int. J. Fatigue 123 (2019) 31–39, doi:10.1016/j.ijfatigue.2019.01.013.

[366] A. Riemer, S. Leuders, M. Thöne, H.A.A. Richard, T. Tröster, T. Niendorf, On the fatigue crack growth behavior in 316L stainless steel manufactured by selective laser melting, Eng. Fract. Mech. 120 (2014) 15–25, doi:10.1016/j.engfracmech.2014.03.008.

[367] G. Meneghetti, D. Rigon, C. Gennari, An analysis of defects influence on axial fatigue strength of maraging steel specimens produced by additive manufacturing, Int. J. Fatigue 118 (2019) 54–64, doi:10.1016/j.ijfatigue.2018.08.034.

[368] M. Akita, Y. Uematsu, T. Kakiuchi, M. Nakajima, R. Kawaguchi, Defect-dominated fatigue behavior in type 630 stainless steel fabricated by selective laser melting, Mater. Sci. Eng. A 666 (2016) 19–26, doi:10.1016/j.msea.2016.04.042.

[369] S.Okazaki Kevinsanny, O. Takakuwa, Y. Ogawa, Y. Funakoshi, H. Kawashima, S. Matsuoka, H. Matsunaga, Defect tolerance and hydrogen susceptibility of the fatigue limit of an additively manufactured Ni-based superalloy 718, Int. J. Fatigue 139 (2020) 105740, doi:10.1016/j.ijfatigue.2020.105740.

[370] Z.H. Jiao, L.M. Lei, H.C. Yu, F. Xu, R.D. Xu, X.R. Wu, Experimental evaluation on elevated temperature fatigue and tensile properties of one selective laser melted nickel based superalloy, Int. J. Fatigue 121 (2019) 172–180, doi:10.1016/j.ijfatigue.2018.12.024.

[371] A. Yadollahi, N. Shamsaei, Additive manufacturing of fatigue resistant materials: challenges and opportunities, Int. J. Fatigue 98 (2017) 14–31, doi:10.1016/j.ijfatigue.2017.01.001.

[372] A.R. Balachandramurthi, J. Moverare, S. Mahade, R. Pederson, Additive manufacturing of alloy 718 via electron beam melting:effect of post-treatment on the microstructure and the mechanical properties, Materials 12 (2018), doi:10.3390/ma12010068.